DEVELOPMENT OF NICKEL ALLOY HYDROGEN ELECTRODES FOR SOLID OXIDE ELECTROLYSIS CELL

Mr. Aritat Wongmaek

จุฬาลงกรณ์มหาวิทยาลัย
CHULALONGKORN UNIVERSITY

A Thesis Submitted in Partial Fulfillment of the Requirements
for the Degree of Master of Engineering in Chemical Engineering
Department of Chemical Engineering
FACULTY OF ENGINEERING
Chulalongkorn University
Academic Year 2019

Copyright of Chulalongkorn University

การพัฒนาขั้วไฮโดรเจนชนิดนิกเกิลอัลลอยสำหรับเซลล์อิเล็กโทรไลซิสแบบออกไซด์ของแข็ง

นายอริย์ธัช วงศ์เมฆ

จุฬาลงกรณ์มหาวิทยาลัย
CHULALONGKORN UNIVERSITY

วิทยานิพนธ์นี้เป็นส่วนหนึ่งของการศึกษาตามหลักสูตรปริญญาวิศวกรรมศาสตรมหาบัณฑิต
สาขาวิชาวิศวกรรมเคมี ภาควิชาวิศวกรรมเคมี
คณะวิศวกรรมศาสตร์ จุฬาลงกรณ์มหาวิทยาลัย
ปีการศึกษา 2562
ลิขสิทธิ์ของจุฬาลงกรณ์มหาวิทยาลัย

Thesis Title	DEVELOPMENT OF NICKEL ALLOY HYDROGEN ELECTRODES FOR SOLID OXIDE ELECTROLYSIS CELL
By	Mr. Aritat Wongmaek
Field of Study	Chemical Engineering
Thesis Advisor	Assistant Professor Pattaraporn Kim, Ph.D.

Accepted by the FACULTY OF ENGINEERING, Chulalongkorn University in Partial Fulfillment of the Requirement for the Master of Engineering

..... Dean of the FACULTY OF ENGINEERING
(Professor SUPOT TEACHAVORASINSKUN, D.Eng.)

THESIS COMMITTEE

..... Chairman
(Assistant Professor Palang Bumroongsakulsawat, Ph.D.)

..... Thesis Advisor
(Assistant Professor Pattaraporn Kim, Ph.D.)

..... Examiner
(Professor BUNJERD JONGSOMJIT, Ph.D.)

..... External Examiner
(Assistant Professor Panpailin Seeharaj, Ph.D.)

จุฬาลงกรณ์มหาวิทยาลัย
CHULALONGKORN UNIVERSITY

อริย์ธัช วงศ์เมฆ : การพัฒนาขั้วไฮโดรเจนชนิดนิกเกิลอัลลอยสำหรับเซลล์อิเล็กโทรไลซิสแบบออกไซด์ของแข็ง. (DEVELOPMENT OF NICKEL ALLOY HYDROGEN ELECTRODES FOR SOLID OXIDE ELECTROLYSIS CELL) อ.ที่ปรึกษาหลัก : ภัทรพร คิม

ขั้วไฮโดรเจนพื้นฐานชนิดนิกเกิล-อิตเทรียมสเตบิไลซ์เซอร์โคเนีย (Ni-YSZ) ในเซลล์อิเล็กโทรไลซิสแบบออกไซด์ของแข็งนั้นมักเกิดการออกซิไดซ์ภายใต้สภาวะที่มีไอน้ำสูง ในการอิเล็กโตรไลซิสเพื่อผลิตไฮโดรเจน นิกเกิลอัลลอยที่มีส่วนประกอบของนิกเกิล โครเมี่ยม (Cr) หรือเหล็ก (Fe) ที่ส่วนประกอบต่างๆ จึงถูกนำมาใช้เพื่อเพิ่มความทนทานต่อสภาวะออกซิเดชั่นที่อุณหภูมิสูงที่ดีกว่านิกเกิล งานวิจัยนี้ศึกษาผลปริมาณของอัลลอยและวิธีการขึ้นรูปที่เหมาะสมสำหรับขั้วแคโทดในเซลล์อิเล็กโทรไลซิสแบบออกไซด์ของแข็ง ในการเลือกขั้วไฮโดรเจนชนิดอัลลอยนั้นนอกจากความคงทนของขั้วแล้ว ยังต้องคำนึงถึงสมรรถนะของขั้วด้วย ในการทดลองนี้จะทำการปรับอัตราส่วนของ โครเมี่ยมหรือเหล็กให้มีสัดส่วนที่ร้อยละ 0 – 20 โดยน้ำหนัก โดยจะคงสัดส่วนระหว่าง โลหะผสมและอิตเทรียมสเตบิไลซ์เซอร์โคเนียที่ร้อยละ 60 ต่อ 40 โดยน้ำหนัก จากนั้นจะทำการทดสอบความต้านทานการเกิดออกซิเดชั่นด้วยการวิเคราะห์การเปลี่ยนแปลงน้ำหนักของสารโดยอาศัยคุณสมบัติทางความร้อน (TGA) และทดสอบสมรรถนะทางไฟฟ้าเคมีด้วย กราฟความสัมพันธ์ระหว่างกระแสกับแรงดัน (IV curve) และอิเล็กโตรเคมีคอลอิมพีแดนซ์สเปกโตรสโคปี (EIS) ที่อุณหภูมิปฏิบัติการในช่วง 650 ถึง 900 องศาเซลเซียส ภายใต้อัตราส่วนไอน้ำต่อไฮโดรเจนที่ 70:30 เซลล์อิเล็กโทรไลซิสแบบออกไซด์ของแข็งโดยโดยมีอิเล็กโทรไลต์เป็นตัวรองรับ (55Ni5Cr-YSZ/YSZ/Pt) นั้นจะแสดงความหนาแน่นกระแสไฟฟ้าที่มีค่าที่สูงและมากกว่าเซลล์อิเล็กโทรไลซิสแบบออกไซด์ของแข็งในสัดส่วนอื่นๆ โดยจะมีค่าความหนาแน่นกระแสไฟฟ้าเท่ากับ -1.09 A/cm^2 ที่ 1.8 V ณ อุณหภูมิปฏิบัติการ 800 องศาเซลเซียส สำหรับอัลลอยที่มีส่วนผสมของเหล็กนั้นจะไม่สามารถขึ้นรูปขั้วไฮโดรเจนได้เนื่องจากความแตกต่างของสัมประสิทธิ์การขยายตัวระหว่างโลหะและชั้นอิเล็กโทรไลต์ และเมื่อนำอัลลอยที่สัดส่วนต่างๆ มาขึ้นรูปตัวรองรับชนิดแคโทดจะพบว่าไม่เหมาะสมที่จะนำไปใช้ต่อ เนื่องจากขั้วมีความเปราะและหักง่าย ดังนั้นเทคนิคการเคลือบฝังและการล้างเคลือบจึงอีกหนึ่งในแนวทางของการพัฒนาความต้านทานต่อการเกิดออกซิเดชั่น พบว่า Ni alloys impregnated Ni-YSZ/YSZ/BSCF มีความคงทนที่ดีกว่าตัวตั้งเดิมแม้ว่าจะมีสมรรถนะที่ต่ำกว่าก็ตาม โดยที่อุณหภูมิ 800 องศาเซลเซียส และภายใต้ความต่างศักดิ์เท่ากับ 1.8 V จะมีความหนาแน่นกระแสไฟฟ้าเท่ากับ -0.26 A/cm^2 โดยขั้วตั้งเดิมนั้นจะมีความหนาแน่นกระแสไฟฟ้าที่สูงกว่าเท่ากับ -0.49 A/cm^2 และสำหรับเทคนิคการล้างเคลือบนั้นไม่เหมาะสมที่จะนำมาใช้ในการขึ้นรูปขั้วอิเล็กโทรดเนื่องจากมีพื้นที่ในการเกิดปฏิกิริยาที่ต่ำ

จุฬาลงกรณ์มหาวิทยาลัย
Chulalongkorn University

สาขาวิชา	วิศวกรรมเคมี	ลายมือชื่อนิสิต .....
ปีการศึกษา	2562	ลายมือชื่อ อ.ที่ปรึกษาหลัก .....

6170417321 : MAJOR CHEMICAL ENGINEERING

KEYWORD: Solid oxide electrolysis cells, Nickle alloy electrode, Hydrogen production, Steam electrolysis, Oxidation tolerance

Aritat Wongmaek : DEVELOPMENT OF NICKEL ALLOY HYDROGEN ELECTRODES FOR SOLID OXIDE ELECTROLYSIS CELL. Advisor: Asst. Prof. Pattaraporn Kim, Ph.D.

The conventional nickel-yttrium stabilized zirconia (Ni-YSZ) cathode in solid oxide electrolysis cell (SOEC) suffers from oxidation after exposed to steam during electrolysis for hydrogen production. The Ni-chromium (Cr)-iron (Fe) alloys with various compositions are introduced to improve cathode oxidation resistance. This study aims to study the effect of alloy contents and determine suitable fabrication method for SOEC cathode. The alloy containing cathode should satisfy both high electrochemical performance and low degradation rate. The content of Fe and Cr are varied in the range of 0-20%wt when the weight ratio of metal to YSZ is maintained constantly at 60:40. The SOEC having Ni-Cr-Fe alloy cathode are fabricated. The oxidation resistances are studied using thermogravimetric analysis (TGA). The electrochemical performance is carried out using current/potential characteristic curve and electrochemical impedance spectroscopy (EIS). The operating temperature is controlled between 650-900 °C with the feed containing steam to hydrogen ratio of 70:30. Electrolyte-supported 55Ni5Cr-YSZ/YSZ/Pt shows the highest current density of -1.09 A/cm^2 at 1.8 V, 800 °C, compared to the other NiCr alloy compositions. For NiFe cathode in the electrolyte-supported cell, the sample cracked due to the thermal expansion after sintering at 1,100 °C for 2 hr. The sintered cathode supporting layer of various alloys loading were fragile and brittle. The wash-coating and impregnating technique was introduced as an alternative method to fabricate the alloy containing cathode. The Ni alloys impregnated improved the durability of SOEC while lowering the performance. The highest current density of conventional Ni-YSZ/ YSZ/ BSCF and alloy-impregnated Ni-YSZ/ YSZ/ BSCF was -0.50 and -0.26 A/cm^2, respectively. For wash-coated electrode, the dense grains were formed which was not suitable for the hydrogen electrode due to lacking of three phase boundary.

จุฬาลงกรณ์มหาวิทยาลัย
Chulalongkorn University

Field of Study:	Chemical Engineering	Student's Signature .....
Academic Year:	2019	Advisor's Signature .....

ACKNOWLEDGEMENTS

I would like to express my deepest gratitude to my advisor Asst. Prof. Pattraporn Kim for her patience, motivation and her kindness advice. Her guidance and support helped me a lot in the research and thesis writing. Also, the SOEC project student for giving their consulting in life and projects and happiness sharing.

Secondly, this research was financially by the PTT public company limited. I would like to express my special thanks to All of the PTT hydrogen project's staffs for providing me an opportunity and the valuable guidance. My sincerely thanks are also to lecturers, scientists, officers and friends in faculty of chemical engineering, Chulalongkorn university.

Last but not the least I would like to express my sincerely acknowledge to my family for their support, inspiration and encouragement in everyday life.

Aritat Wongmaek

จุฬาลงกรณ์มหาวิทยาลัย
CHULALONGKORN UNIVERSITY

TABLE OF CONTENTS

Page

..... iii

ABSTRACT (THAI) iii

..... iv

ABSTRACT (ENGLISH) iv

ACKNOWLEDGEMENTS v

TABLE OF CONTENTS vi

LIST OF TABLES viii

LIST OF FIGURES ix

Chapter I 1

1.1. Motivation 1

1.2. Research objective 2

1.3. Research scope 3

1.4. Expected benefit 3

Chapter II 4

2.1. Solid oxide electrolysis cell (SOEC) 4

2.2. Hydrogen electrode (cathode) 8

2.3. Hydrogen electrode degradation 9

2.4. Ni-Cr-Fe alloys 15

Chapter III 26

3.1. Material and powder preparation 26

3.2. Cell fabrication 27

จุฬาลงกรณ์มหาวิทยาลัย
Chulalongkorn University

3.2.1. Fabrication of a conventional SOEC 27

3.2.2. Fabrication of SOEC having Ni-alloy as a component in cathode 30

3.2.3. Fabrication of SOEC having Ni-alloy /YSZ cathode 30

3.2.3.1. Fabrication of SOEC having the cathode fabricated from Ni-alloy washed coated Ni-YSZ powder 30

3.2.3.2. Fabrication of SOEC having Ni-alloy impregnated Ni-YSZ cathode 31

3.3. Characterization 31

3.4. Electrochemical performance measurement 32

Chapter IV 36

4.1. Thermogravimetric analysis (TGA) 36

4.2. X-ray photoelectron spectra (XPS) 37

4.3. X-ray powder diffraction (XRD) and X-ray Fluorescence analysis 42

4.4. Hydrogen Temperature programmed reduction (H_2-TPR) analysis 44

4.5. Scanning electron microscope (SEM) 45

4.6. Electrochemical performance 50

Chapter V 57

REFERENCES 59

APPENDICES 66

Appendix A 68

VITA 82

จุฬาลงกรณ์มหาวิทยาลัย
CHULALONGKORN UNIVERSITY

LIST OF TABLES

Page

Table 1 The typical characteristics of the main electrolysis technologies [4]. 7

Table 2 Electrolysis cell performance, at 1,000 °C [30] 8

Table 3 Cell and test conditions for Cell A, B, C and D [31]. 9

Table 4 Thermal expansion coefficients of pure nickel at various temperature [40] .. 17

Table 5 Average coefficients of expansion of hot-rolled nickel-chromium alloys [41]20

Table 6 Curie temperature (Tc) and average CTE [7]. 22

Table 7 Chemical composition of Alloy 600 (wt%) [44] 24

Table 8 Composition of Ni-Fe-Cr/-YSZ 26

Table 9 YSZ electrolyte slurry composition 29

Table 10 steam to H_2 ratio of operating condition 34

Table 11 The calculated OCV at operating temperature 35

Table 12 The ratio of Cr^{6+}/Cr^{3+} of the various NiCr-YSZ composition 40

Table 13 Composition of Ni-Fe-Cr/-YSZ obtained from XPS 41

Table 14 Composition of Ni-Fe-Cr/-YSZ obtained from SEM-EDX 48

Table 15 Resistance of the various electrolyte support NiCr-YSZ/ YSZ/ Pt. R0, RHF and RLF are referred to ohmic resistance and polarization resistance in high frequency region and low frequency region, respectively. 54

Table 16 Resistance of the Ni-YSZ/ YSZ/ BSCF and Ni alloys impregnated Ni-YSZ/ YSZ/ BSCF. R0, RHF and RLF are referred to ohmic resistance and polarization resistance in high frequency region and low frequency region, respectively. 56

จุฬาลงกรณ์มหาวิทยาลัย
Chulalongkorn University

LIST OF FIGURES

Page

Fig. 1 The schematic drawing of SOEC principle[9] 5

Fig. 2 The schematic drawing of the triple phase boundary in hydrogen electrode-electrolyte [9] 6

Fig. 3 The calculation of required energy for H_2 production from steam electrolysis [8] 7

Fig. 4 SOEC unit with waste thermal energy recovery [8] 7

Fig. 5 Long term electrolysis testing of Cell A, B and C at 1A/cm^2, 800°C. A) Cell potentials , B) total polarization resistances (R_p) , C) ohmic resistances (R_s) and D) ohmic resistances (R_s) over time at the same beginning [31]. 10

Fig. 6 Schematic drawing of Ni agglomeration in Ni-YSZ electrodes at 840 °C; Ni (blue), YSZ (yellow); a) Large Ni particles are easier to agglomerate, which reduce the interface connectivity and TPB active sites; b) Small Ni particles are harder to agglomerate over time [6]. 11

Fig. 7 Thermodynamic data for Ni(g) and $Ni(OH)_2$(g) in the gas mixture of hydrogen gas and steam at 950 °C [33]. 12

Fig. 8 Schematic drawing of local Ni alignment and vaporization–deposition processes at TPB [34]. 12

Fig. 9 DoO of a Ni-YSZ cermet at 600 - 800 °C, under 20% O_2 in helium (and a total flow rate 5 Lh^{-1}) [35]. 13

Fig. 10 Effect of the oxidation degree on the structural expansion of the studied cermet upon oxidation in 0.3 and 20% O_2 at 600 and 800 °C. [35]. 14

Fig. 11 LSVs of Fe-Ni-Cr/NC, Fe-Cr/Nc, Ni-Cr/Nc, Ni-Fe/C and Pt/C with a scanning rate of 5mVs^{-1} in 1M KOH (a) and corresponding Tafel slopes (b), (b) Bar plots of

จุฬาลงกรณ์มหาวิทยาลัย
Chulalongkorn University

overpotentials (@10 $mAcm^{-2}$) and Tafel slope, (d) Long-term stability measurement of Fe-Ni-Cr/NC and Pt/C in 1 M KOH via chronoamperometry measurement. [37] 15

Fig. 12 specific weight gain of the porous Ni-Fe alloys anode supports oxidized in air at (a) 600 °C ,(b) 750 °C and (c) Thermal expansion of Ni-Fe alloy anode supports in Ar as a function of temperature [38] 16

Fig. 13 weight gain measurement for NiCr model alloys exposed to superheated steam at 700 °C for 500 hr: (a) emery-polished (#2400), (b) mirror polished (c) electro-polished and (d) mirror polished of Ni-Cr-Fe [39] 17

Fig. 14 CTE versus temperature of nickel [40] 18

Fig. 15 Lattice parameter and α of sample B, 99.985% Fe at the Curie temperature. Expansion coefficient α – to the right. [40] 19

Fig. 16 CTE of Fe-Ni-Cr (Fe:Ni=1) alloys and 8 mol% YSZ. [7]. 21

Fig. 17 CTE of Fe-Ni-Cr alloys with constant %wt Cr and 8 mol% YSZ. [7]. 21

Fig. 18 Expansion mismatch with YSZ at room temperature to 1000°C [7]. 22

Fig. 19 SEM micrographs of metallographic cross-section of for mirror polished specimens exposed to superheated steam at 700 °C for 500 hr [39] 23

Fig. 20 Schematic representation of the oxidation behavior of Ni-Cr model alloys exposed to superheated steam at 700°C for 500 hr as a function of Cr-content in Ni-xCr: (a) $x < 24$ wt.%, (b) $24 \leq x \leq 26$ wt.% and (c) $x > 26$ wt.%. [39] 24

Fig. 21 The effect of (a) temperature and (b) pH for Alloy 600 on OCP [44]. 25

Fig. 22 The effect of temperature on the absolute impedance [44]. 25

Fig. 23 Preparation of Ni Alloys-YSZ hydrogen electrode 28

Fig. 24 Electrolyte layer fabrication on hydrogen electrode 29

Fig. 25 Oxygen electrode fabrication on sintered YSZ/hydrogen electrode 29

Fig. 26 Equivalent circuit for impedance response fitting [47] 33

Fig. 27 Schematic drawing of the test system 34

จุฬาลงกรณ์มหาวิทยาลัย
CHULALONGKORN UNIVERSITY

Fig. 28 Degree of oxidation (%) of: (a) Ni-Fe-YSZ; (b) Ni-Cr-YSZ; (c) Ni alloy: containing 72 wt% Ni, 14-16 wt% Cr and 6-10 wt% Fe with the ratio of Ni alloy to YSZ at 60:40 wt% compared to conventional Ni-YSZ in air atmosphere at 800 ℃; and, (d) Ni alloy-YSZ compared to conventional Ni-YSZ in air atmosphere from room temperature – 800 ℃. 37

Fig. 29 The XPS of different Fe and Cr loading Ni-YSZ electrodes: (a) Ni spectra of NiCr-YSZ; (b) Ni spectra of NiFe-YSZ; (c) Cr 2p3/2 spectra of NiCr-YSZ and (d) Fe 2p3/2 spectra of NiFe-YSZ 39

Fig. 30 The deconvolution of Cr XPS spectra of various NiCr-YSZ composition 40

Fig. 31 The deconvolution of Ni XPS spectra of various (a) NiCr-YSZ and (b) NiFe-YSZ composition 41

Fig. 32 pattern of sintered powder at 1,100 ℃ for 2 hr of (a) NiCr-YSZ (b) NiFe-YSZ (c) Impregnated Ni-YSZ compared to conventional Ni-YSZ and (d) Alloy 600-YSZ[56] 43

Fig. 33 Hydrogen TPR profile of cathode starting powder with different Cr or Fe loading from 5 to 20 wt%, sintered at 1,100 ℃ for 2 hr: (a) NiCr-YSZ and (b) NiFe-YSZ and (c) conventional Ni-YSZ and alloy 45

Fig. 34 SEM images at 5000X magnification of various Ni-Fe-Cr content in cathode sintered at 1100 ℃ for 2 hr, (a-d) sintered hydrogen electrode containing 5 to 20 wt% Cr, respectively, (e-h) sintered hydrogen electrode containing 5 to 20 wt% Fe, respectively, (i) sintered conventional electrode, (j) sintered Ni-alloys impregnated electrode and (k) sintered Ni alloys wash-coated electrode. 47

Fig. 35 Sintered hydrogen electrode on the electrolyte supporting layer at 1,100℃ for 2hr, using 5 ℃/min. (a-d) hydrogen electrode containing 5 to 20 wt% Cr respectively, (e) hydrogen electrode containing 5 %wt Fe loading , (f) Ni alloys impregnated Ni-YSZ cathode 49

Fig. 36 SEM patterns at 700X magnification of Ni Alloy impregnated Ni-YSZ electrode (a) before and (b) after electrochemical performance test, and (c) the EDX mapping of Ni Alloy impregnated Ni-YSZ electrode 50

จุฬาลงกรณ์มหาวิทยาลัย
Chulalongkorn University

Fig. 37 Comparison of the electrochemical performance of various operating temperature and steam to H_2 ratio at 70:30 of (a) electrolyte-supported conventional Ni-YSZ/YSZ/Pt and (b-e) electrolyte-supported NiCr/YSZ/Pt with varying Cr contents from 5 to 20 wt%, respectively 52

Fig. 38 Comparison of the electrochemical performance of various Cr contents from 0 to 20 wt% and steam to H_2 ratio at 70:30 of conventional at 800 °C (a) IV profiles and (b) electrochemical impedance response (EIS) 54

Fig. 39 Comparison of the electrochemical performance between (Red lines) Ni alloy impregnated Ni-YSZ/YSZ/BSCF electrode and (Black lines) conventional Ni-YSZ/YSZ/BSCF electrode using steam to H_2 ratio at 70:30: (a) at 800 °C and (b) from 650 °C to 900 °C 55

Fig. 40 Comparison of Ni alloy impregnated Ni-YSZ/YSZ/BSCF and conventional Ni-YSZ/YSZ/BSCF (a) the durability at applied 1.1 V and (b) electrochemical impedance response at different duration (800 °C and H_2O:H_2 = 70:30) 56

จุฬาลงกรณ์มหาวิทยาลัย
Chulalongkorn University

Chapter I

Introduction

1.1. Motivation

Thailand energy sources are mainly depending on the petroleum resources [1]. They are imported in form of processed and crude oil. The prices are unstable, and uncontrollable. These affects to the energy security of Thailand. The definitions of energy security are adequate, affordable and reliable supplied [2]. The technology of energy production with low price and environmental sustainability is the key priorities to increase Thailand energy security. The requirement for clean and sustainable fuel sources has encouraged great interests in electrochemical technologies such as high temperature solid oxide electrolysis cell (SOEC). Hydrogen produced from renewable electricity through SOEC is promising as a next generation fuel. The operating temperature of SOEC was in the range of 700 – 1000 °C. The advantage of using high temperature electrolysis is the improvement of electrochemical reaction rates and reduction of electrical energy demand. It can also provide an efficient hydrogen production [3-5]. However, high operating temperature also accelerates oxidation of electrode under high steam environment [6, 7]. Yttria-stabilized zirconia (YSZ) has been widely used as an electrolyte material because it shows a good thermal and chemical stability and performs as a good oxide-ion conductor with enough mechanical strength [8]. Nickel-yttria stabilized zirconia (Ni-YSZ) is therefore generally used as hydrogen electrode in SOEC because of its good thermal compatibility with the electrolyte [9] and good catalytic properties [10-12].; nevertheless, the material shows low durability due to Ni oxidation under high steam partial pressure, resulting in lowered electronic conductivity and catalytic activity of the electrode. The Ni-Cr-Fe

จุฬาลงกรณ์มหาวิทยาลัย
Chulalongkorn University

alloys are introduced to improve the hydrogen electrode oxidation resistance. These alloys are generally used as an electrode for hydrocarbon cracking reaction and coke prevention [13-15], an interconnect [16-18] and the supported metal [19-21] of solid oxide fuel cell (SOFC). The alloy supports have a good thermal conductivity and ductility which may develops the thermal shock resistance, cell temperature gradient [22] and also improved the mechanical strength of the electrode. The oxidation resistance was reported to enhance with the increasing of alloys contents [7, 23]. Two most critical properties of SOEC's hydrogen electrode are a similar thermal expansion matching with electrolyte and high oxidation resistance in the operating environment of the SOEC. To achieve both characteristics, the suitable alloy composition was considered.

In this study, the effects of chromium and iron additions to a Ni-alloy based hydrogen electrode was investigated. Thermal expansion behavior, oxidation rate, and electrochemical performance was measured. The electrode application in SOEC was also investigated.

จุฬาลงกรณ์มหาวิทยาลัย
Chulalongkorn University

1.2. Research objective

To study the effect of Ni-alloy on the performance of hydrogen electrode in solid oxide electrolysis cell

Subobjective includes:

1.2.1 To study the effect of alloy contents on the hydrogen electrode fabrication.

1.2.2 Improve the oxidation resistance and electrochemical performance of hydrogen electrode in operating environment comparing to conventional electrode.

1.2.3 To investigate the electrochemical performance and stability of conventional and Ni alloy based SOEC

1.3. Research scope

1.3.1 Varying the content of Fe and Cr in the range of 0-20 wt% when the weight ratio of metal to YSZ is maintained constantly at 60:40.

1.3.2 Comparing the effects of alloy deposition method between wash-coating and conventional dry-pressing on electrochemical performance test using current/potential characteristic curve and electrochemical impedance spectroscopy (EIS)

1.3.3 Comparing the durability between alloys wash-coated Ni-YSZ/YSZ/BSCF and conventional Ni-YSZ/YSZ/BSCF at constant potential at 1.1V.

1.4. Expected benefit

จุฬาลงกรณ์มหาวิทยาลัย
Chulalongkorn University

1.4.1 Electrode material which has a higher electrochemical performance and higher oxidation resistance

1.4.2 Research project to Fabricate a SOEC to decrease the emission of carbon to the environment with renewable energy source toward Thailand Low-Carbon Societies.

1.4.3 Development of Thailand energy security with reducing hydrogen synthesized from hydrocarbon.

Chapter II

Literature review

2.1. Solid oxide electrolysis cell (SOEC)

Solid oxide electrolysis cell is a device to produce hydrogen and oxygen by applying electricity to water. This is the reverse of the process that occurs in a fuel cell. The cell consists of three parts, hydrogen electrode, oxygen electrode and electrolyte. The schematic drawing of SOEC is shown in Fig.1. Steam is fed into the porous cathode. Steam reacts with the electron to form hydrogen gas and oxygen ion. Oxygen ion pass through electrolyte membrane and reacts at anode to form oxygen gas and generate electron as shown in equation (1)-(3).

Hydrogen electrode reaction

$$H_2O + 2e^- \rightarrow H_2 + O^{2-} \quad (1)$$

Oxygen electrode reaction

$$2O^{2-} \rightarrow O_2 + 4e^- \quad (2)$$

Overall reaction

$$2H_2O \rightarrow 2H_2 + O_2 \quad (3)$$

จุฬาลงกรณ์มหาวิทยาลัย
Chulalongkorn University

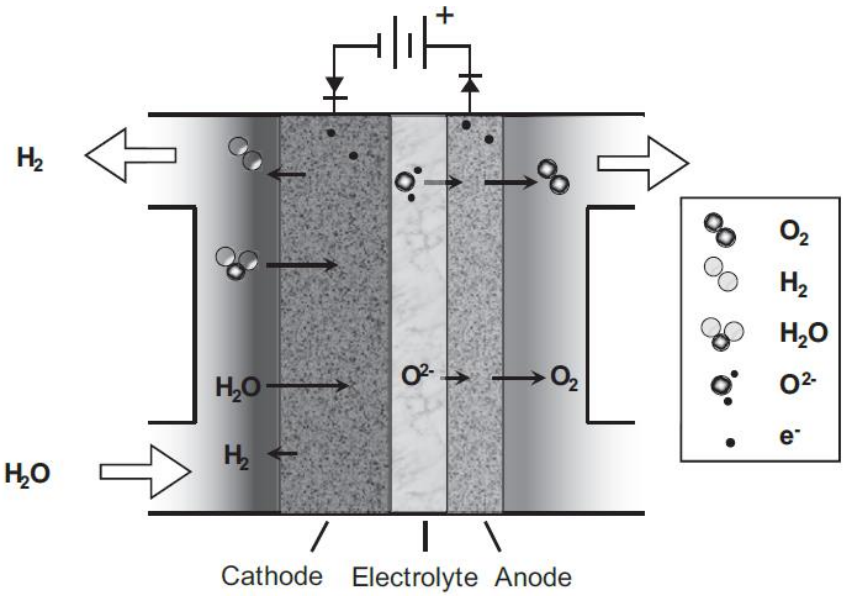

Fig. 1 The schematic drawing of SOEC principle[9]

The reaction takes place at the triple phase boundary (TPB). Three phases are ion conductor (electrolyte), electron conductor (metal) and pore phase for transporting gas and steam. TPBs are electrochemical active site. Increasing TPB density will increase the reaction rate and increase the electrochemical performance. The schematic diagram of TPB can be seen on Fig. 2

จุฬาลงกรณ์มหาวิทยาลัย

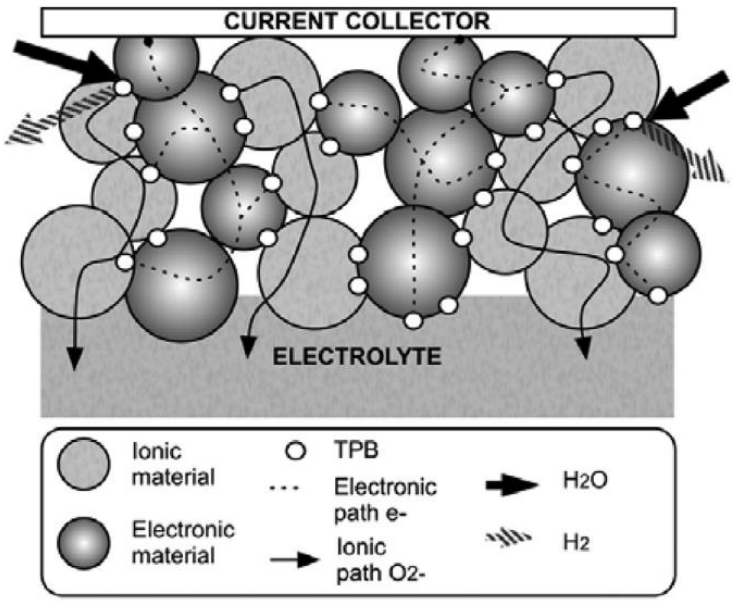

Fig. 2 The schematic drawing of the triple phase boundary in hydrogen electrode-electrolyte [9]

The low temperature electrolysis such as proton exchange membrane (PEM) [24-27] are generally used with low operating temperature (<100℃). The disadvantage is high demand of electrical energy due to thermodynamics. The total energy demand (ΔH) for SOEC can be showed by equation (4)

$$\Delta H = \Delta G + T\Delta S \qquad (4)$$

Where ΔG is the required electrical energy (Gibbs free energy), TΔS is the demand of thermal energy for the process (J/mol H_2). From Fig. 3, when increasing operating temperature, the demand of electrical energy decreases. Therefore, high operating temperature electrolysis provides opportunities to use the waste thermal energy from industry to produce hydrogen. Waste thermal energy from output gasses can also be recovered as shown in Fig. 4. The comparison of electrolysis technologies is demonstrated in table 1.

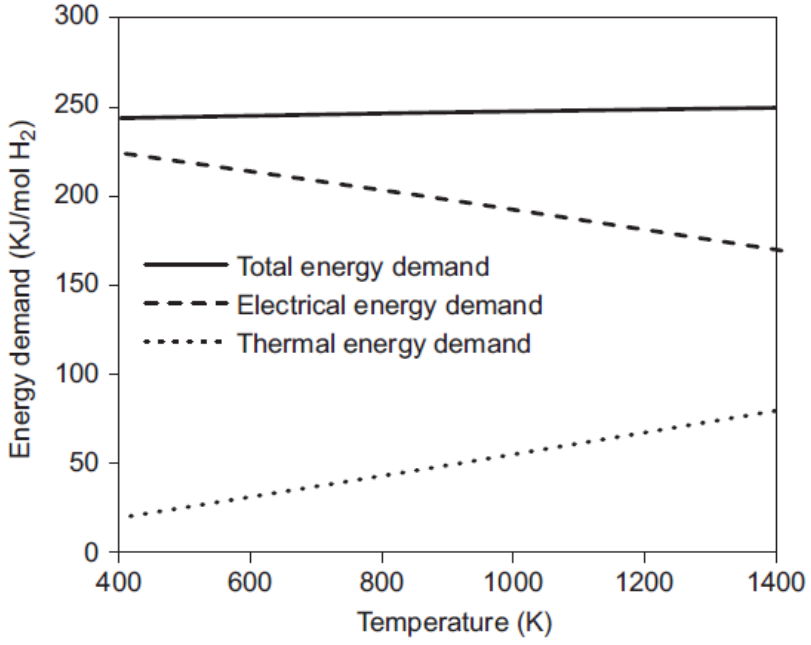

Fig. 3 The calculation of required energy for H_2 production from steam electrolysis [8]

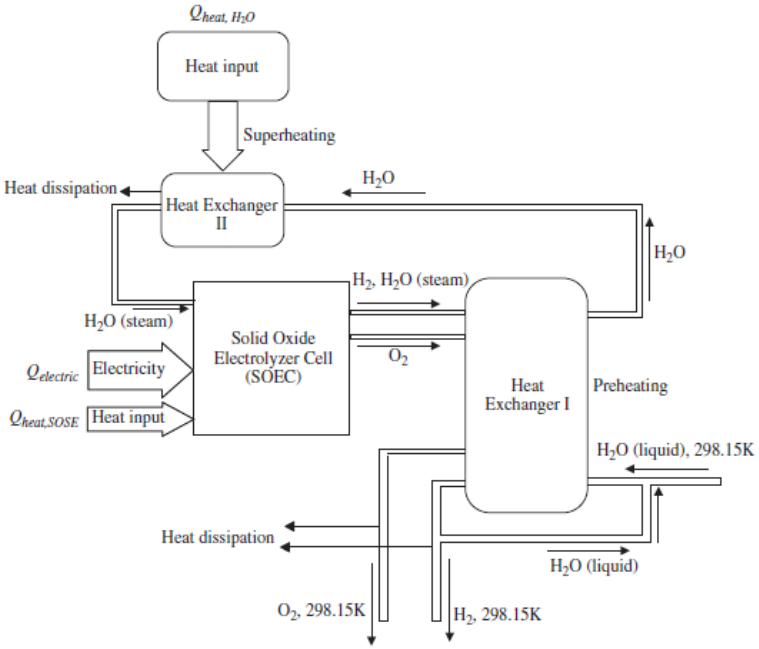

Fig. 4 SOEC unit with waste thermal energy recovery [8]

Table 1 The typical characteristics of the main electrolysis technologies [4].

	Low Temperature Electrolysis			High Temperature Electrolysis		
	Alkaline (OH^-) electrolysis		Proton Exchange (H^+) electrolysis	Oxygen ion(O^{2-}) electrolysis		
	Liquid	Polymer Electrolyte Membrane		Solid Oxide Electrolysis (SOE)		
	Conventional	Solid alkaline	H^+ - PEM	H^+ - SOE	O^{2-} - SOE	Co-electrolysis
Operation principles	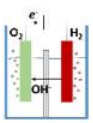	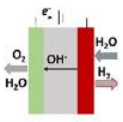	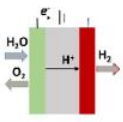	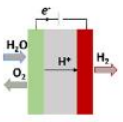	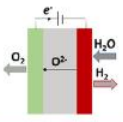	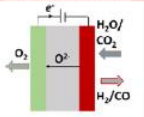
Charge carrier	OH^-	OH^-	H^+	H^+	O^{2-}	O^{2-}
Temperature	20-80°C	20-200°C	20-200°C	500-1000°C	500-1000°C	750-900°C
Electrolyte	liquid	solid (polymeric)	solid (polymeric)	solid (ceramic)	solid (ceramic)	solid (ceramic)
Anodic Reaction (OER)	$4OH^- \rightarrow 2H_2O + O_2 + 4e^-$	$4OH^- \rightarrow 2H_2O + O_2 + 4e^-$	$2H_2O \rightarrow 4H^+ + O_2 + 4e^-$	$2H_2O \rightarrow 4H^+ + 4e^- + O_2$	$O^{2-} \rightarrow {}^1/_2O_2 + 2e^-$	$O^{2-} \rightarrow {}^1/_2O_2 + 2e^-$
Anodes	Ni > Co > Fe (oxides) Perovskites: $Ba_{0.5}Sr_{0.5}Co_{0.8}Fe_{0.2}O_{3-\delta}$, $LaCoO_3$	Ni-based	IrO_2, RuO_2, $Ir_xRu_{1-x}O_2$ Supports: TiO_2, ITO, TiC	Perovskites with protonic-electronic conductivity	$La_xSr_{1-x}MnO_3$ + Y-Stabilized ZrO_2 (LSM-YSZ)	$La_xSr_{1-x}MnO_3$ + Y-Stabilized ZrO_2 (LSM-YSZ)
Cathodic Reaction (HER)	$2H_2O + 4e^- \rightarrow 4OH^- + 2H_2$	$2H_2O + 4e^- \rightarrow 4OH^- + 2H_2$	$4H^+ + 4e^- \rightarrow 2H_2$	$4H^+ + 4e^- \rightarrow 2H_2$	$H_2O + 2e^- \rightarrow H_2 + O^{2-}$	$H_2O + 2e^- \rightarrow H_2 + O^{2-}$ $CO_2 + 2e^- \rightarrow CO + O^{2-}$
Cathodes	Ni alloys	Ni, Ni-Fe, $NiFe_2O_4$	Pt/C MoS_2	Ni-cermets	Ni-YSZ Subst. $LaCrO_3$	Ni-YSZ perovskites
Efficiency	59-70%		65-82%	up to 100%	up to 100%	-
Applicability	commercial	laboratory scale	near-term commercialization	laboratory scale	demonstration	laboratory scale
Advantages	low capital cost, relatively stable, mature technology	combination of alkaline and H^+-PEM electrolysis	compact design, fast response/start-up, high-purity H_2	enhanced kinetics, thermodynamics: lower energy demands, low capital cost		+ direct production of syngas
Disadvantages	corrosive electrolyte, gas permeation, slow dynamics	low OH^- conductivity in polymeric membranes	high cost polymeric membranes; acidic: noble metals	mechanically unstable electrodes (cracking), safety issues: improper sealing		
Challenges	Improve durability/reliability; and Oxygen Evolution	Improve electrolyte	Reduce noble-metal utilization	microstructural changes in the electrodes: delamination, blocking of TPBs, passivation		C deposition, microstructural change electrodes

2.2. Hydrogen electrode (cathode)

Hydrogen electrode is used to support steam and hydrogen diffusion. Noble metals, such as Platinum (Pt) and non-valuable metal such as Nickel (Ni) can be selected as SOEC cathode. Because of high cost of noble metal, formation of volatile oxides and aging of porous structure at a high temperature, the used of Pt is not suitable [28]. To develop the TPB active site, Ni is mixed with ion conductor Yttria stabilized zirconia (YSZ). Electrochemical performance of Ni-YSZ electrode is studied by many researches. Eguchi et al. [29] studies the characteristic of IV polarization of Ni-YSZ and Pt hydrogen electrode. It is found that Ni–YSZ performs better in the Solid Oxide Fuel Cell (SOFC) mode but suffers from higher potential used in the SOEC mode. It is assumed that the Ni is oxidized to form NiO which has lower active site, resulting in low performance. The long-term performance is interested in many literatures. Maskalick [30] studies and tests the electrochemical performance stability of SOEC. The test is maintained for 450 hr at 1,000 °C. The performances at operating time between 0 – 500 h are shown on Table 2. The electrical resistance of the cell is constant at 5.5 mΩ.

Chulalongkorn University

Table 2 Electrolysis cell performance, at 1,000 °C [30]

Time on Test (h)	Current		Voltage		H_2/H_2O Ratio	
	(A)	($mAcm^{-2}$)	(Total)	(IR-free)	Inlet	Outlet
70	23.9	319	1.245	1.087	0.272	1.603
95	24.0	320	1.253	1.122	0.316	1.593
240	24.9	332	1.251	1.114	0.289	0.852
430	24.9	332	1.253	1.116	0.011	0.181

455	22.5	300	1.231	1.108	0.004	0.052
500	25.0	333	1.358	1.146	0.499	0.656

2.3. Hydrogen electrode degradation

High temperature SOEC has many advantages compared to low temperature electrolysis. Both ohmic conductivity and reaction kinetics are developed by elevating temperature, which reduces the internal resistance in cell and increase the efficiency. However, the initial performance is not the only requirement, but also long-term stability in operating conditions. Hydrogen electrode degradation is considered as a key limitation that lower the performance of the SOEC. To increase the durability and extend the electrode lifetime, the cathode is required to develop the microstructure by changing or replacing the electrode with alternative materials.

Haunch et al. [31] investigates on microstructure of hydrogen electrode and reports that for long-term stability for SOEC at high current density and high humidity condition, the NiO-YSZ precursor should be 1) as dense with fine particle and pore size as possible, 2) the three phases should be size-matched and homogeneously dispersed. The cell specifications are shown on the table 3. Cell C with fine microstructure with dense structure provides the highest durability for both polarization and ohmic resistance over time compared to others (Fig. 5).

Table 3 Cell and test conditions for Cell A, B, C and D [31].

Name	Cell specifications	Qualitative microstructure information	Test specifications
Cell A	No specific fuel electrode layer. Support layer functioning as fuel electrode (Ni/3YSZ)	Coarse structure. Significantly higher pore fraction than Cell B, C and D	800 °C, $p(H_2O)/p(H_2)$:90/10, 56% H_2O conversion, −1 A/cm^2, 1000 h
Cell B	Support layer (Ni/3YSZ) and active fuel electrode layer (Ni/8YSZ)	Coarse microstructure. As dense as possible for a Ni/YSZ:40/60 fuel electrode.	800 °C, $p(H_2O)/p(H_2)$:90/10, 56% H_2O conversion, −1 A/cm^2, 1000 h
Cell C	Support layer (Ni/3YSZ) and active fuel electrode (Ni/8YSZ)	Fine microstructure. As dense as possible for a Ni/YSZ:40/60 fuel electrode.	800 °C, $p(H_2O)/p(H_2)$:90/10, 56% H_2O conversion, −1 A/cm^2, 2000 h
Cell D	Sister-cell to cell C	Fine microstructure. As dense as possible for a Ni/YSZ:40/60 fuel electrode.	800 °C, $p(H_2O)/p(H_2)$:90/10, 56% H_2O conversion, −1.25 A/cm^2, 1000 h

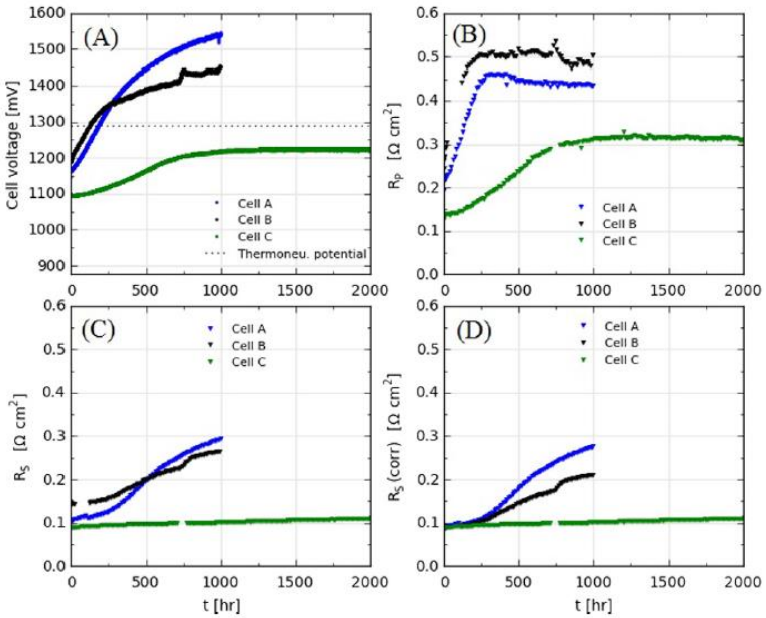

Fig. 5 Long term electrolysis testing of Cell A, B and C at 1A/cm^2, 800°C. A) Cell potentials , B) total polarization resistances (R_p) , C) ohmic resistances (R_s) and D) ohmic resistances (R_s) over time at the same beginning [31].

จุฬาลงกรณ์มหาวิทยาลัย
Chulalongkorn University

Ni particle agglomeration in the hydrogen electrode decreases the density of active TPB sites. It affects in both SOFC and SOEC. Hauch et al. [32] also reports that the initial rate of agglomeration is caused by the increasing of H_2O partial pressure. The role of initial microstructure of Ni-YSZ cathode is also important. The initial performance decreases with the increasing of initial particle size because of Ni agglomeration increased [6]. The schematic drawing of Ni agglomeration was shown in Fig.6.

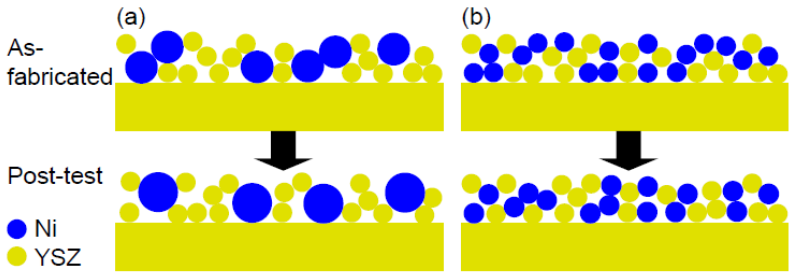

Fig. 6 Schematic drawing of Ni agglomeration in Ni-YSZ electrodes at 840 °C; Ni (blue), YSZ (yellow); a) Large Ni particles are easier to agglomerate, which reduce the interface connectivity and TPB active sites; b) Small Ni particles are harder to agglomerate over time [6].

Other several phenomena that affect the stability of Ni-YSZ cermet have been observed. The evaporation and re-precipitation due to variable oxygen activities within the cathode layer are investigated. At equilibrium with a humid gas, The thermodynamic data from Fig. 7 indicates that $Ni(OH)_2(g)$ is the most volatile species in a gas mixture of H_2O and H_2. Its partial pressure is six order higher than the pure Ni(g). The partial pressure of Ni significantly increases due to the addition of small quantities of water vapor. The deposition process can be described by equation 5 and 6. The illustration of vaporization-deposition process is shown on Fig. 8.

จุฬาลงกรณ์มหาวิทยาลัย
CHULALONGKORN UNIVERSITY

$$Ni(OH)_2(g) \leftrightarrow NiO(s) + H_2O(g) \qquad (5)$$

$$NiO(s) + H_2 \leftrightarrow Ni(s) + 2H_2O(g) \qquad (6)$$

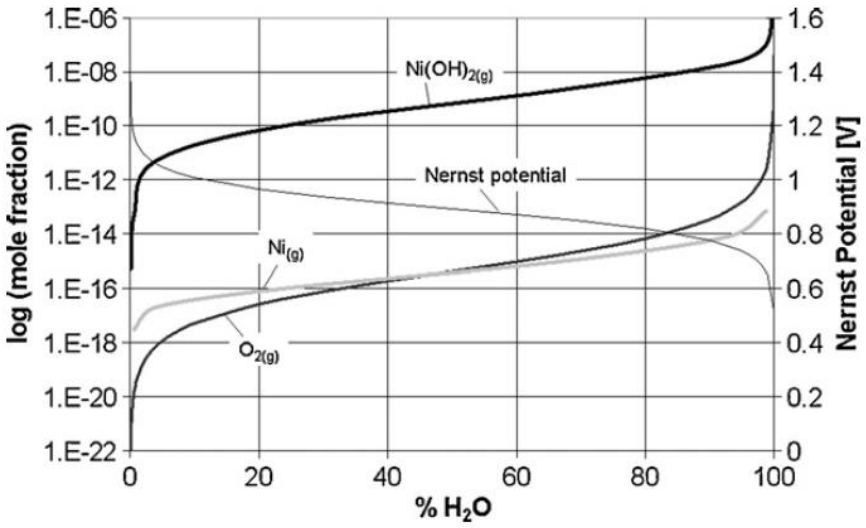

Fig. 7 Thermodynamic data for Ni(g) and $Ni(OH)_2$(g) in the gas mixture of hydrogen gas and steam at 950 °C [33].

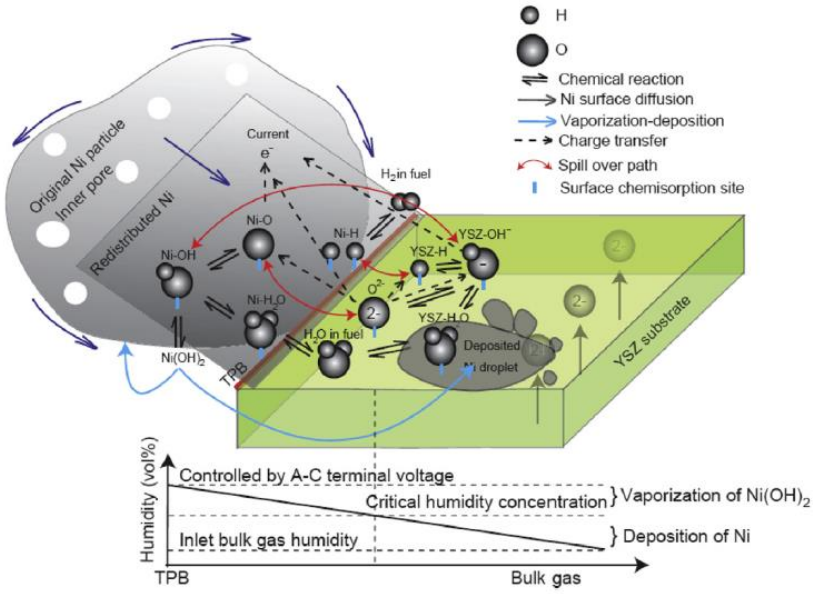

Fig. 8 Schematic drawing of local Ni alignment and vaporization–deposition processes at TPB [34].

The conventional Ni-YSZ electrode suffers from a reduction-oxidation cycle. The structural instabilities occur during re-oxidation, it leads to serious degradation in

SOEC performance. The oxidation tolerance of Ni-YSZ is studied at several temperatures by Laurencin et al. [35]. Fig. 9 shows the result of Ni-YSZ tolerance under 20% O_2 between 600 to 800 °C. The oxidation rate boosts when the temperature increases. At 800 °C, the oxidation of the cermet is fully oxidized in a few minutes. The degree of oxidation (DoO) is expressed by equation 7

$$\mathrm{DoO}\ (t) = \frac{m(t) - m_{Ni-YSZ}}{m_{NiO-YSZ} - m_{Ni-YSZ}} \qquad (7)$$

Where $m_{Ni\text{-}YSZ}$ is the initial mass of the reduced sample, m(t) is the mass at time t during oxidation and $m_{NiO\text{-}YSZ}$ is the fully oxidized mass of sample.

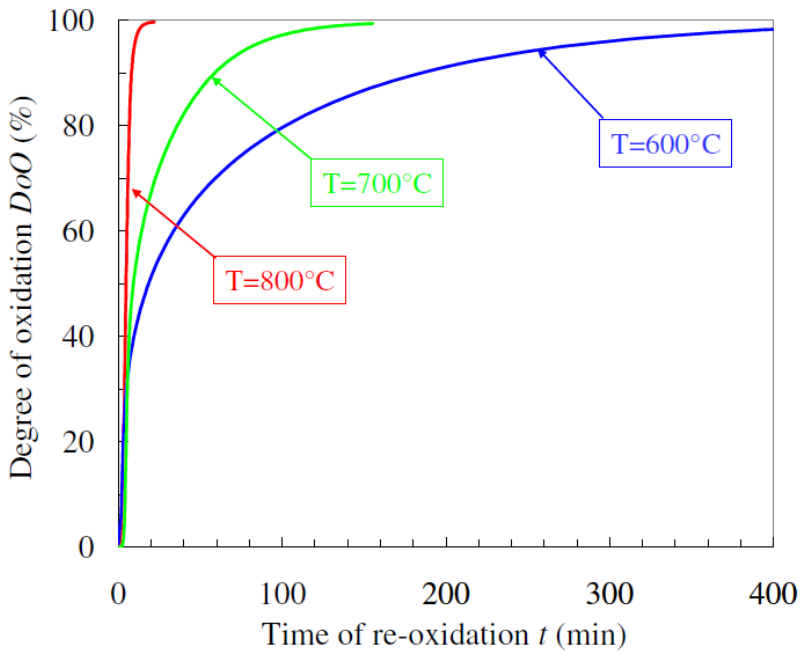

Fig. 9 DoO of a Ni-YSZ cermet at 600 - 800 °C, under 20% O_2 in helium (and a total flow rate 5 Lh^{-1}) [35].

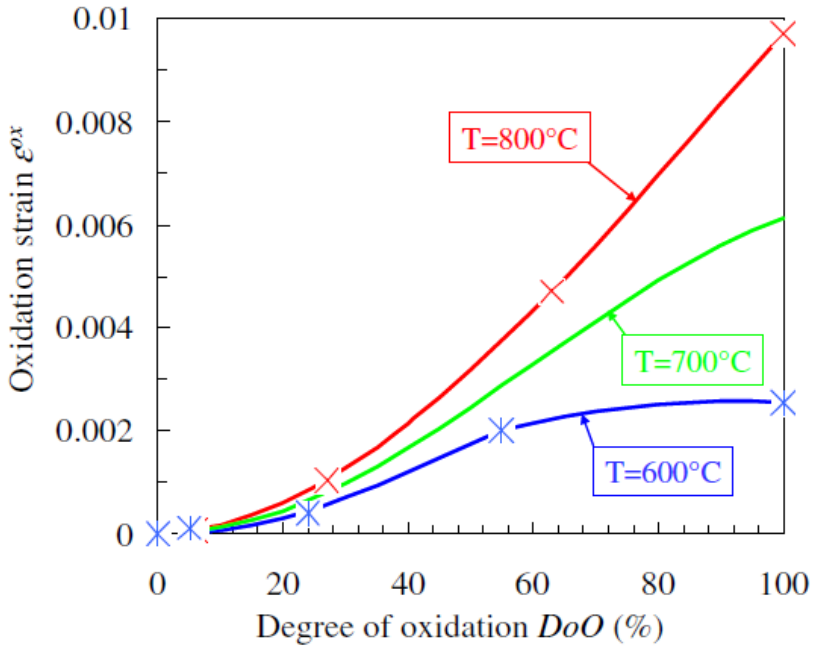

Fig. 10 Effect of the oxidation degree on the structural expansion of the studied cermet upon oxidation in 0.3 and 20% O_2 at 600 and 800 °C. [35].

Fig. 10 shows the plot between oxidation strain and degree of oxidation. At low oxidation degree (DoO < 5%). Dimensional expansion is not detected. At high oxidation degree (DoO > 5%), the cermet expansion is boosted with the increasing oxidation temperature. When the 1 mm thick cermet was fully oxidized, the expansion strain was reported at 0.97% at 800 °C.

To enhance the performance of hydrogen evolution reaction (HER) of the hydrogen electrode, the doped metal such as manganese (Mn), neodymium (Nd), iron (Fe) and chromium (Cr) is suggested. It improves the adsorption due to the higher catalytic active sites [36]. Zhang J. et al. [37] develops N-doped bamboo-like carbon nanotube consisted of Fe-Ni-Cr as an electrocatalysts for water-splitting. The HER electrochemical performance is shown in Fig. 11. Fe-Ni-Cr/NC shows lowest over-

potential (exclude Pt/C) to drive 10 mA/cm^2 which indicates the best catalytic performance for HER.

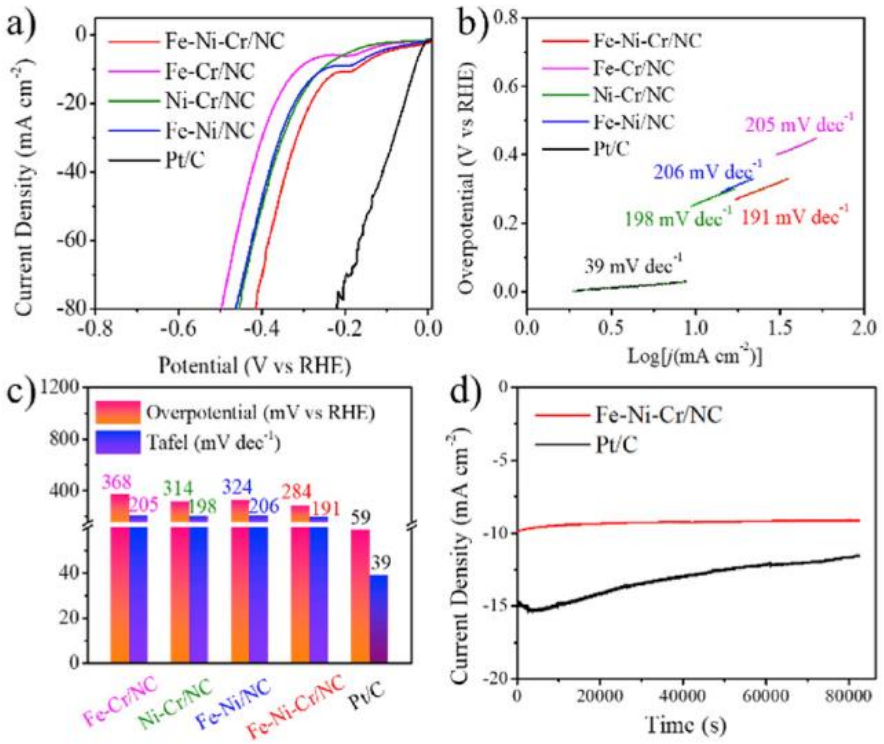

Fig. 11 LSVs of Fe-Ni-Cr/NC, Fe-Cr/Nc, Ni-Cr/Nc, Ni-Fe/C and Pt/C with a scanning rate of 5mVs^{-1} in 1M KOH (a) and corresponding Tafel slopes (b), (b) Bar plots of overpotentials (@10 mAcm^{-2}) and Tafel slope, (d) Long-term stability measurement of Fe-Ni-Cr/NC and Pt/C in 1 M KOH via chronoamperometry measurement. [37]

จุฬาลงกรณ์มหาวิทยาลัย
CHULALONGKORN UNIVERSITY

2.4. Ni-Cr-Fe alloys

To develop the oxidation tolerance of hydrogen electrode, The Ni-Cr-Fe alloys are introduced. Ni-Fe alloys are known as the primary material for the hydrogen electrode support due to their oxidation resistance. The effects of Fe loading in Ni based support are studied by Wang X. et al. [38]. The Fe_2O_3 loading are varied from 0 -50 % wt. the oxidation behavior is shown in Fig. 12a and 12b at 600 and 750 °C

respectively. The addition of Fe loading improves the oxidation tolerance in both operating temperatures. They also investigated the thermal expansion which is considered as a key parameter for cell fabrication. Coefficient of thermal expansion (CTE) of 0 – 50 % wt. Fe are 16.1 15.9 14.5 and 12.1 x $10^{-6}K^{-1}$ respectively, as seen in Fig. 12c.

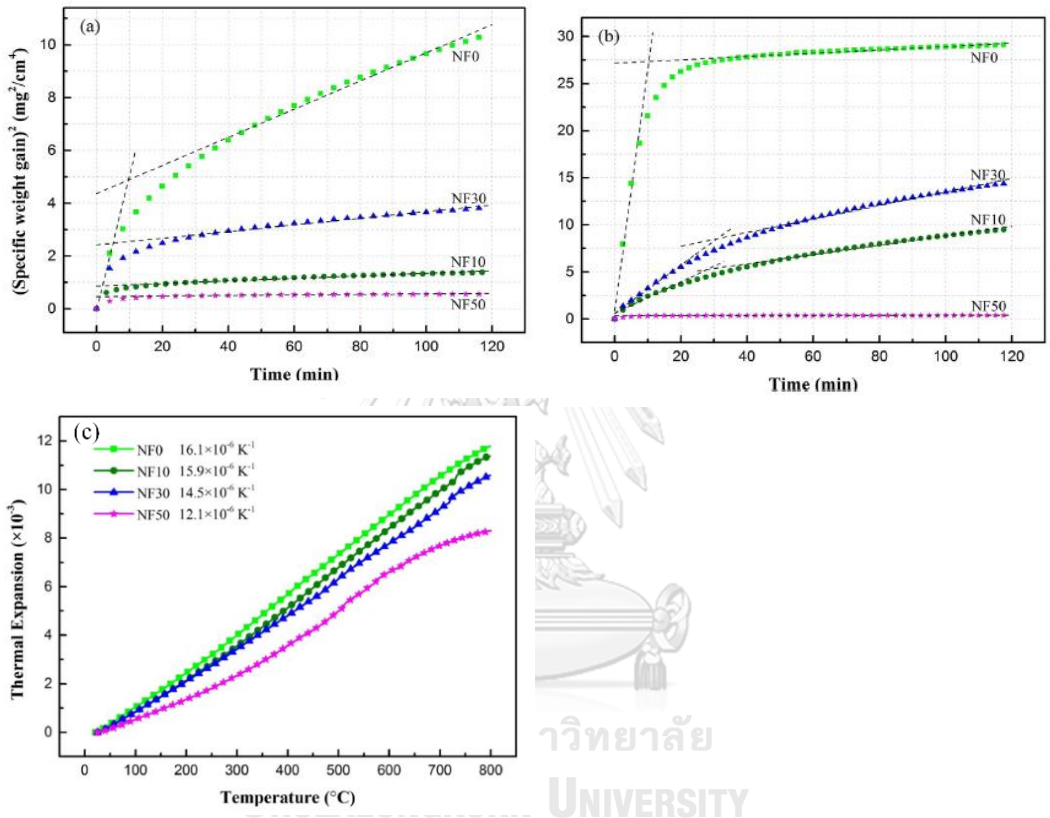

Fig. 12 specific weight gain of the porous Ni-Fe alloys anode supports oxidized in air at (a) 600 ℃ ,(b) 750 ℃ and (c) Thermal expansion of Ni-Fe alloy anode supports in Ar as a function of temperature [38]

The important of Ni based alloys on corrosion and oxidation at superheated steam is investigated by Hamdani [39]. Fig. 13 shows the oxidation behavior of Ni-Cr-Fe alloys which exposed to the 700 ℃ steam for 500 hr. The effect of Cr content is

varied. Both mirror and electro-polished samples show a higher oxidation rate. The addition of Fe content reduces the oxidation resistance of Ni-Cr based alloys.

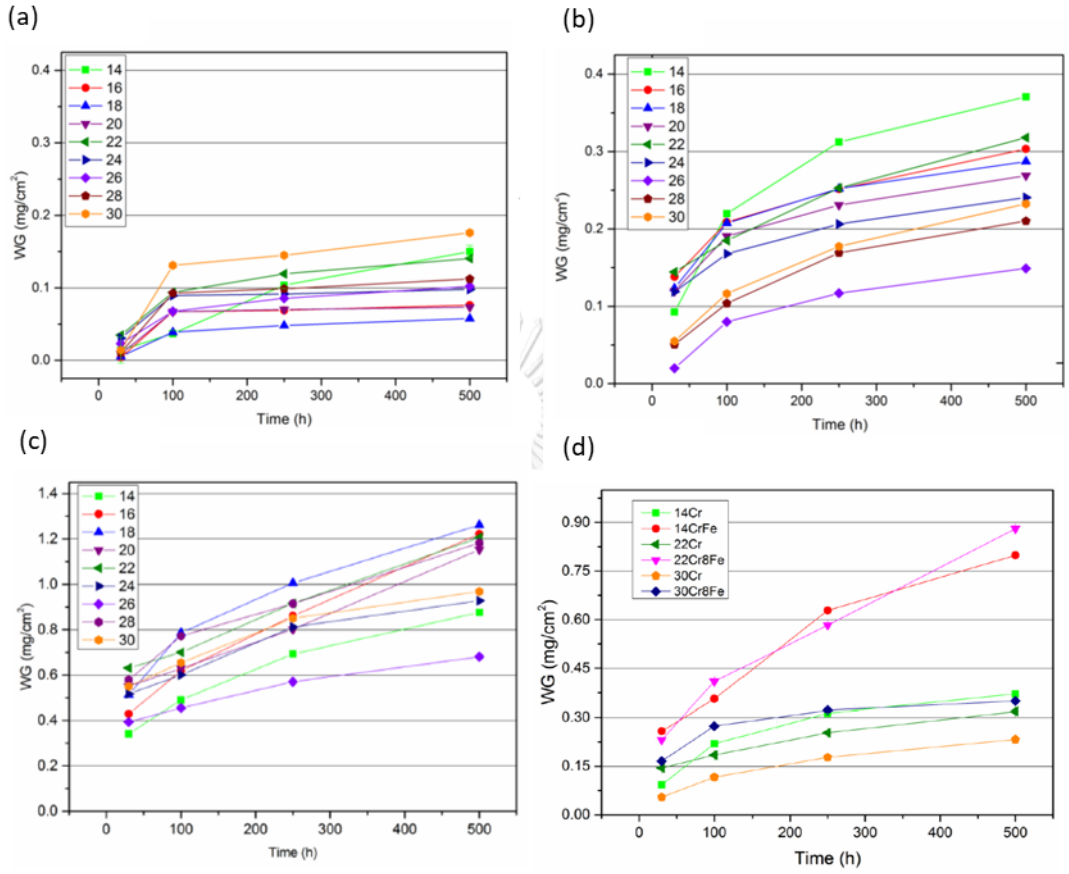

จุฬาลงกรณ์มหาวิทยาลัย
CHULALONGKORN UNIVERSITY

Fig. 13 weight gain measurement for NiCr model alloys exposed to superheated steam at 700 °C for 500 hr: (a) emery-polished (#2400), (b) mirror polished (c) electro-polished and (d) mirror polished of Ni-Cr-Fe [39]

CTE of pure Nickel at various temperature is studied by Hwang J.W. [40] and the results shows in Table 4 and Fig. 14. It presents that the highest expansion occurs at 330 °C.

Table 4 Thermal expansion coefficients of pure nickel at various temperature [40]

Temperature (^{o}C)	Thermal expansion coefficient ($x10^{6}$) $^{o}C^{-1}$
100	15.3
270	17.6
320	21.1
340	20.1
356	18.1
380	13.1
400	12.4
450	14.1
500	15.4
700	16.3
800	16.7
900	19.2
1000	22.1

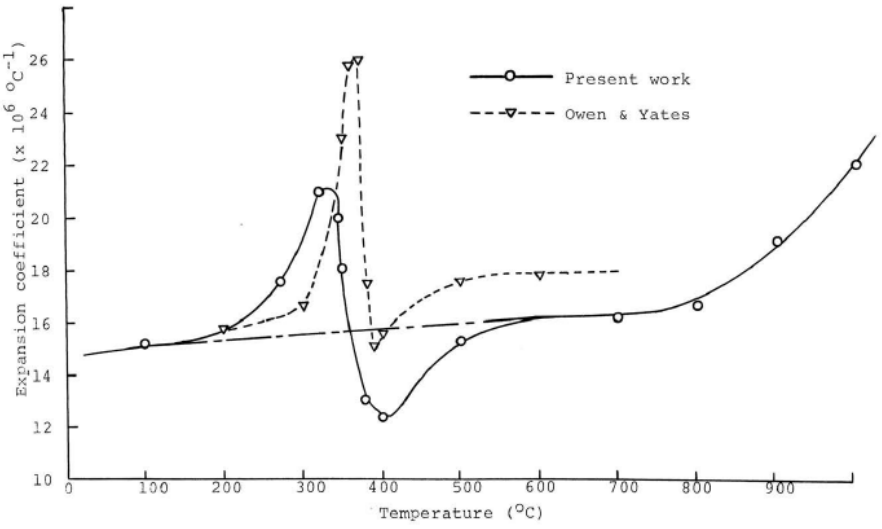

Fig. 14 CTE versus temperature of nickel [40]

Then the expansion of pure iron is reported in Fig. 15. It increases with the increasing of temperature. The CTE rapidly correlates to the anomalous change of

lattice parameter. This clearly represents that the thermal expansion of pure iron is affected by the magnetostriction. The expansion of iron increases and becomes constant and falling at the Curie temperature. The Curie temperature is a temperature which magnetic materials sharp transform their magnetic properties. At Curie point, ferromagnetic turns to paramagnetic.

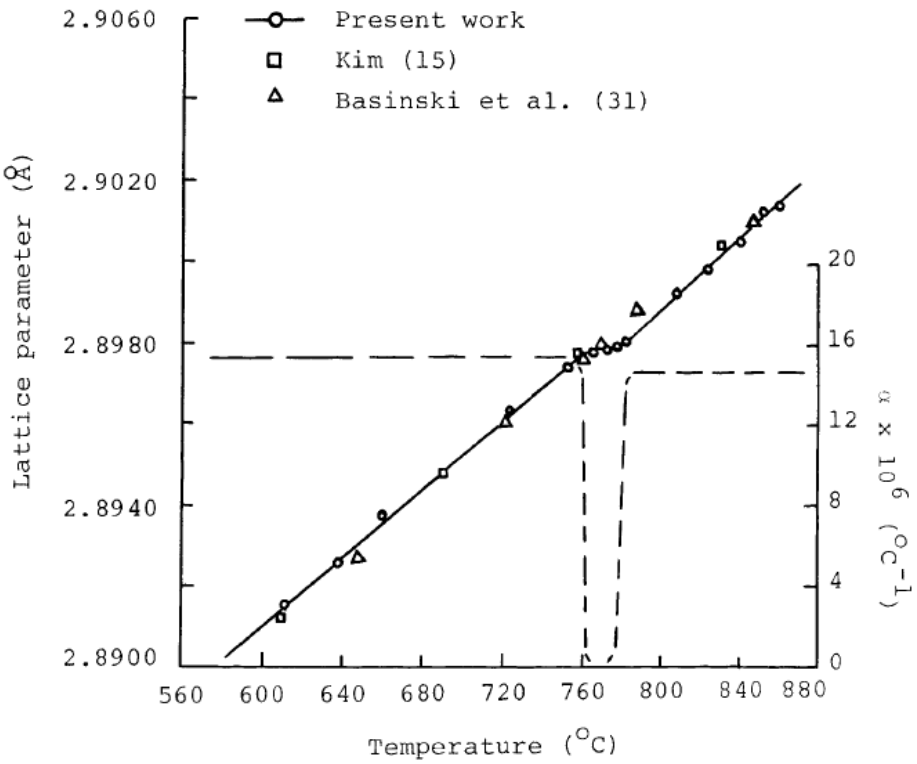

Fig. 15 Lattice parameter and α of sample B, 99.985% Fe at the Curie temperature. Expansion coefficient α – to the right. [40]

Hidnert [41] studied the thermal expansion behavior of Ni-Cr alloys. The average coefficients of expansion are shown in Table 5. The anomalous change is not detected.

Table 5 Average coefficients of expansion of hot-rolled nickel-chromium alloys [41]

Sample	Chemical composition		Average coefficients of expansion per degree centigrade										
	Ni	Cr	20° to 60°C	20° to 100°C	20° to 200°C	20° to 300°C	20° to 400°C	20° to 500°C	20° to 600°C	20° to 700°C	20° to 800°C	20° to 900°C	20° to 1000°C
	(%)	(%)	$\times 10^6$	$\times 10^6$	$\times 10^6$	$\times 10^6$	$\times 10^6$	$\times 10^6$	$\times 10^6$	$\times 10^6$	$\times 10^6$	$\times 10^6$	$\times 10^6$
1292	77	19.3	…	13.6	14.0	14.3	14.5	15.1	15.6	16.1	16.5	17.0	17.6
1402	77	19.6	13.1	13.3	13.8	14.0	14.4	15.0	15.7	16.2	16.7	17.2	17.8
1293	76.8	20.4	13.8	13.0	13.0	13.3	13.9	14.7	15.3	15.8	16.2	16.7	17.2

Church et al. [7] studies both coefficient of thermal expansion (CTE, α_T) and oxidation resistance of varying alloy contents. Fig 16 shows the effect of Cr contents (Fe:Ni = 1) on CTE. Increasing Cr contents, decreases the Curie temperature and increase the CTE at above Curie point. The thermal expansion behavior below Curie temperature is the result from strong spontaneous magnetostriction in the magnetic state [42, 43]. For Fig. 17, the constant Cr with increasing Ni content affect both Curie temperature and also the average of CTE values (before and after the Curie Temperature). With increasing Ni content, CTE decreases at pre-Curie and increases at post-Curie. The Curie temperature and average CTE are shown on table 6.

จุฬาลงกรณ์มหาวิทยาลัย
CHULALONGKORN UNIVERSITY

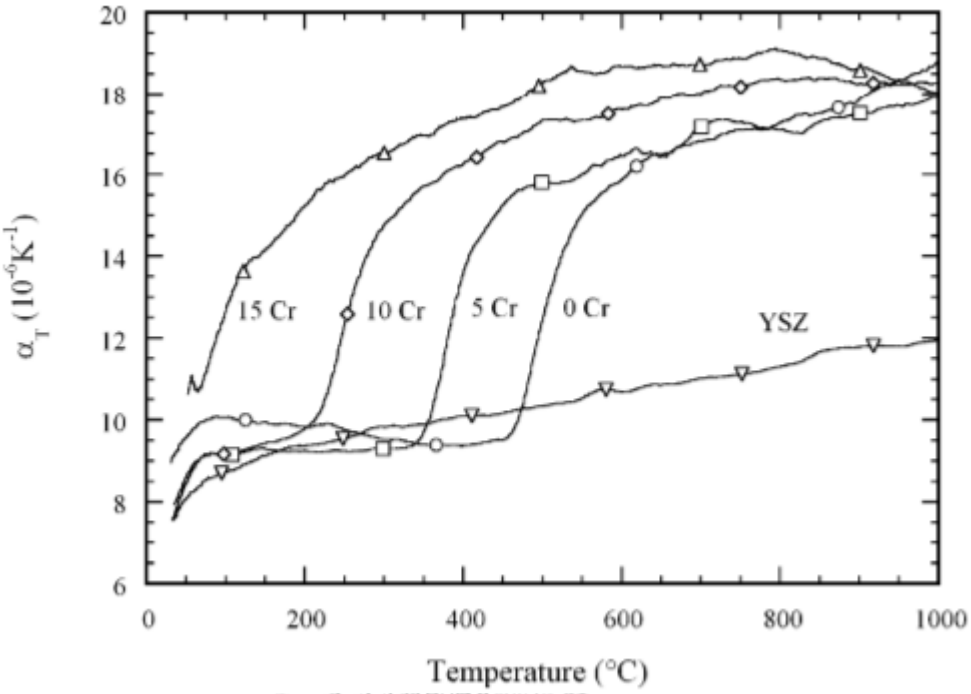

Fig. 16 CTE of Fe-Ni-Cr (Fe:Ni=1) alloys and 8 mol% YSZ. [7].

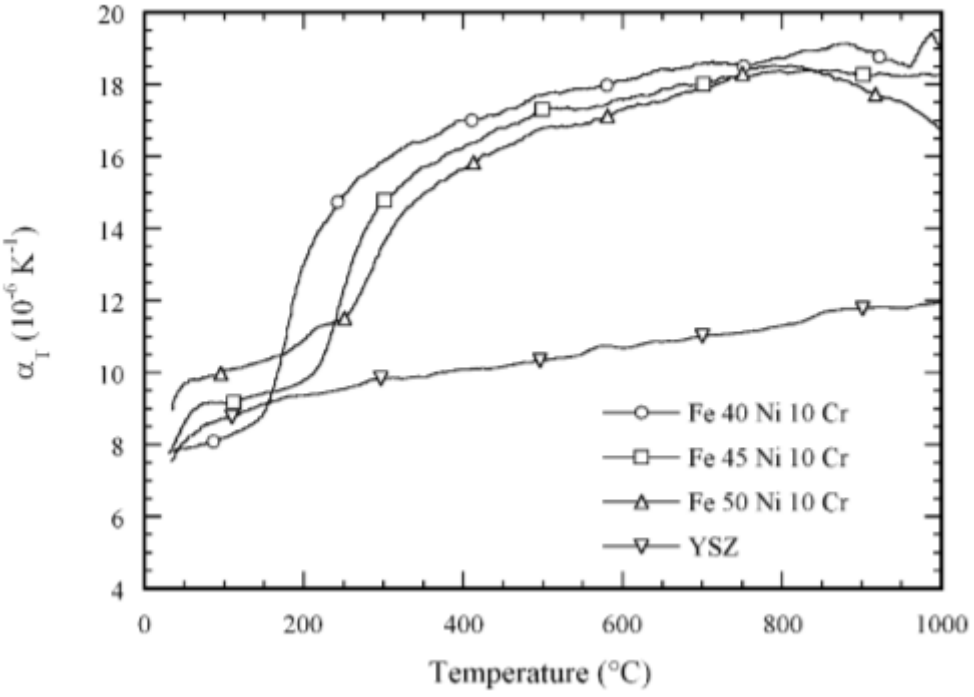

Fig. 17 CTE of Fe-Ni-Cr alloys with constant %wt Cr and 8 mol% YSZ. [7].

Table 6 Curie temperature (Tc) and average CTE [7].

Sample composition (wt.%)	Curie temperature (°C)	Low temperature CTE, α_M (10^{-6} K^{-1})	High temperature CTE, α_M (10^{-6} K^{-1})
YSZ[a]	n/a	9.05	10.88
Fe50Ni	493	9.73	17.09
Constant Fe			
Fe45Ni5Cr	324	7.93	17.24
Fe40Ni10Cr	156	8.02	17.84
Fe35Fe15Cr	[b]	[b]	17.99
Fe:Ni = 1			
Fe47.5Ni5Cr	353	9.17	17.12
Fe45Ni10Cr	221	9.16	17.52
Fe42.5Ni15Cr	64	9.14	17.94
Constant Ni			
Ni45Fe5Cr	375	10.07	16.98
Ni40Fe10Cr	251	10.32	17.42
Ni35Fe15Cr	89	10.20	17.83
Fe–Cr			
Fe	749	15.09	[c]
Fe5Cr	750	13.43	[c]
Fe10Cr	715	12.69	[c]
Fe12Cr	704	12.38	15.40
Fe15Cr	674	11.87	14.96
Fe20Cr	635	11.52	16.06
Fe25Cr	602	11.42	15.58

Low and high temperature CTE were calculated in the range of 20 °C to (T_C −50) and from (T_C +50) to 1000 °C, respectively.
[a] α_M calculated from 20 to 500 °C (low) and 500 to 1000 °C (high).
[b] Curie temperature was not measureable.
[c] CTE was not reported due to the α–γ phase transition in this temperature range.

Thermal expansion mismatch is one of the important properties that affects the stability of electrode at operating environment. The results of Cr addition are shown on Fig. 18. The Fe50Ni and Fe47.5 have similar CTE with YSZ up to 450 °C.

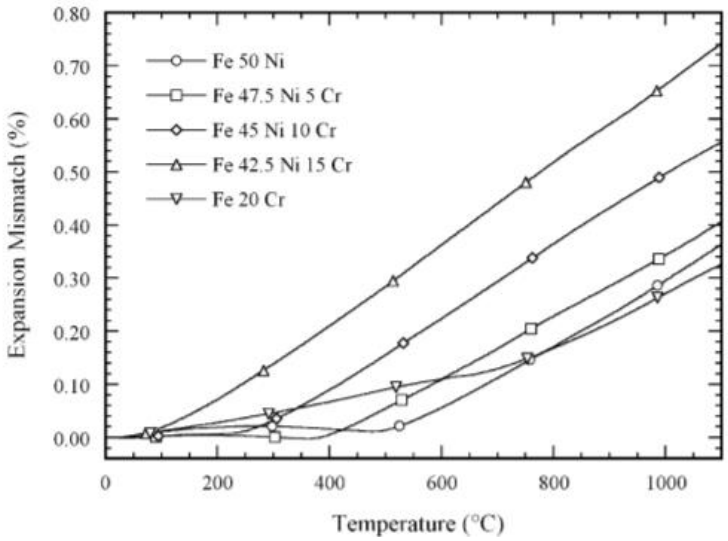

Fig. 18 Expansion mismatch with YSZ at room temperature to 1000°C [7].

Ni based alloys has a capacity to form a protective oxide layer which mainly involves of chromium. The Ni based alloys at various compositions is investigated by Hamdani [39]. The outer layer is affected by the steam corrosion as seen in Fig. 19. The existing nodules trends to decrease with the increasing of Cr content and cannot be seen within the Ni-Cr-Fe samples. The schematic drawing of oxidation behavior of Ni-Cr alloys is shown in Fig. 20.

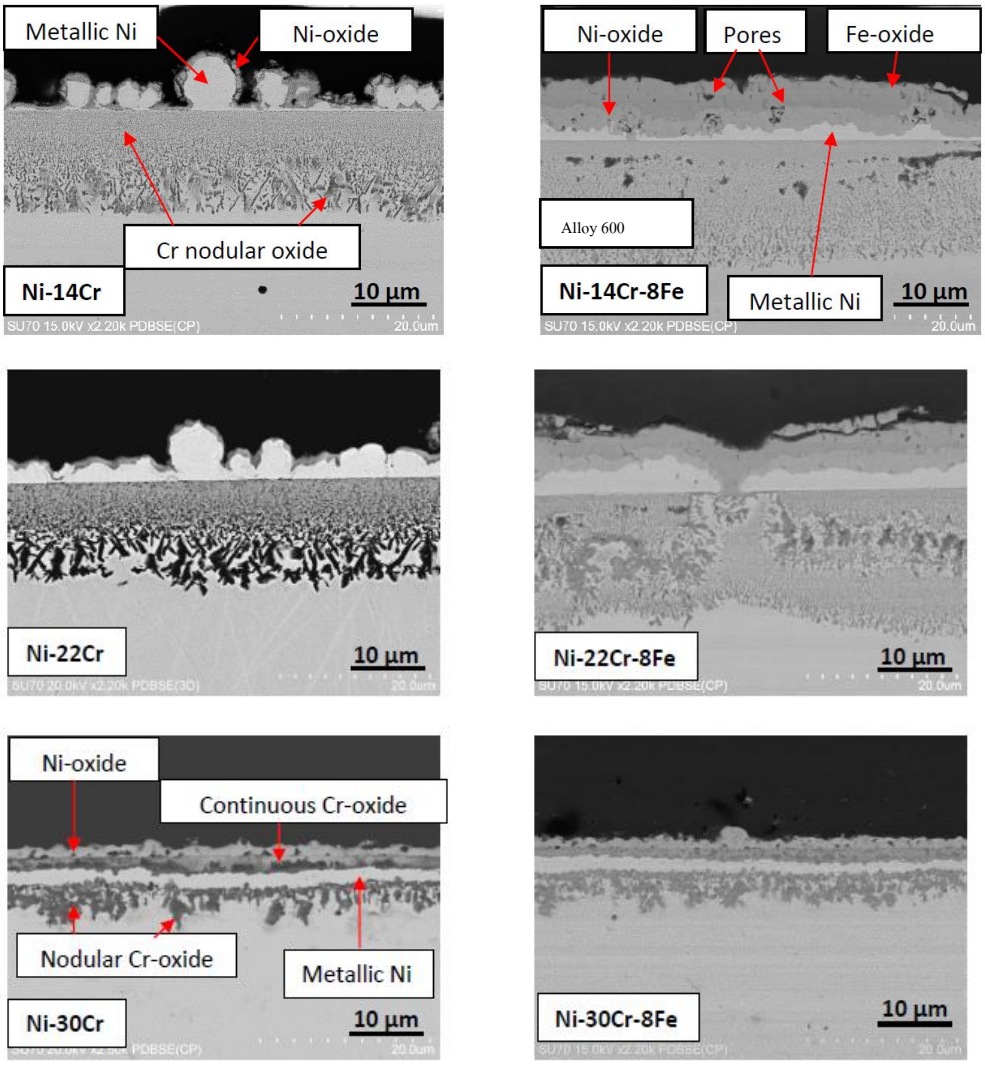

Fig. 19 SEM micrographs of metallographic cross-section of for mirror polished specimens exposed to superheated steam at 700 °C for 500 hr [39]

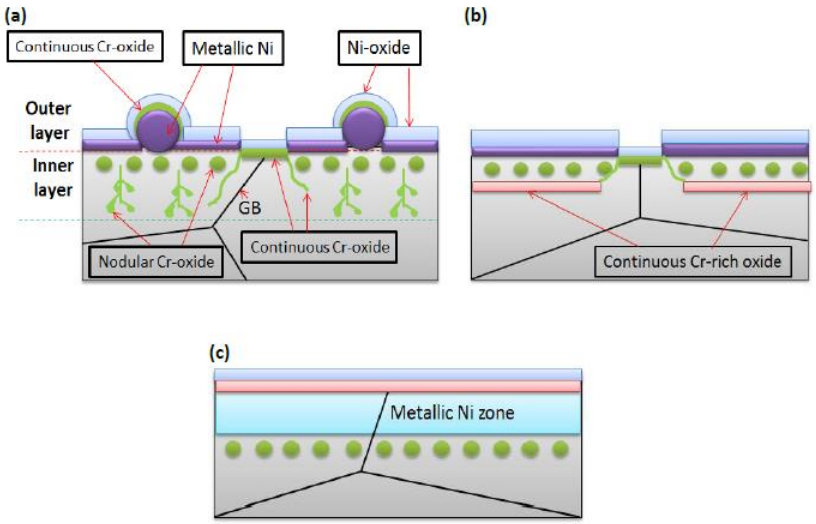

Fig. 20 Schematic representation of the oxidation behavior of Ni-Cr model alloys exposed to superheated steam at 700°C for 500 hr as a function of Cr-content in Ni-xCr: (a) x < 24 wt.%, (b) 24 ≤ x ≤ 26 wt.% and (c) x > 26 wt.%. [39]

Alloy 600 is a standard material used for steam generator tube in primary coolant circuit of pressurized water reactor (PWR) for nuclear power plant. It provides a good tolerance to general corrosion and pitting. Yang et al. [44] study the operating temperature and pH which affect alloy 600 material. Table 7 shows the composition of the alloy 600. Boron (B) and Lithium (Li) are used as the neutron absorber and pH control of the reactor coolant respectively. From Fig. 21, the open circuit potential (OCP) is significantly decreased by the increasing of operating temperature, but slightly decreases with the increasing of pH at the same temperature.

จุฬาลงกรณ์มหาวิทยาลัย
Chulalongkorn University

Table 7 Chemical composition of Alloy 600 (wt%) [44].

Alloy	Ni	Cr	Fe	Mn	Si	C	Cu	S
600	73.593	16.040	9.020	0.200	0.310	0.071	0.045	0.001

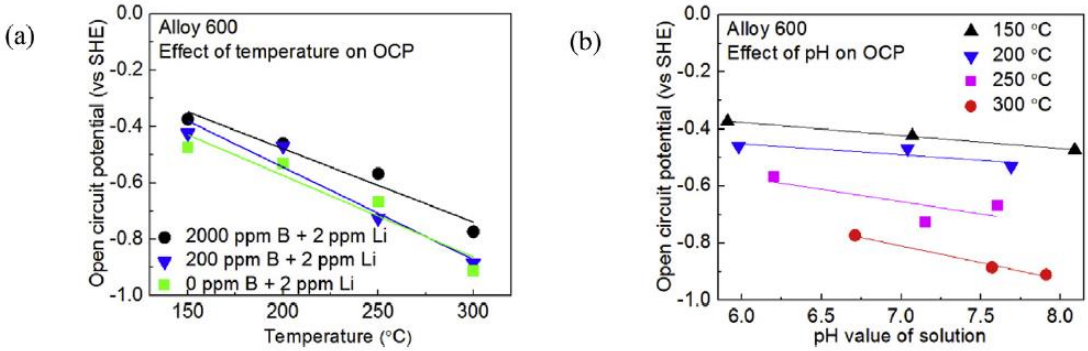

Fig. 21 The effect of (a) temperature and (b) pH for Alloy 600 on OCP [44].

The effect of temperature on the absolute impedance was also studied. The increasing of temperature reduces the impedance as see in Fig. 22. This indicates the improvement of corrosion resistance with the increased temperature.

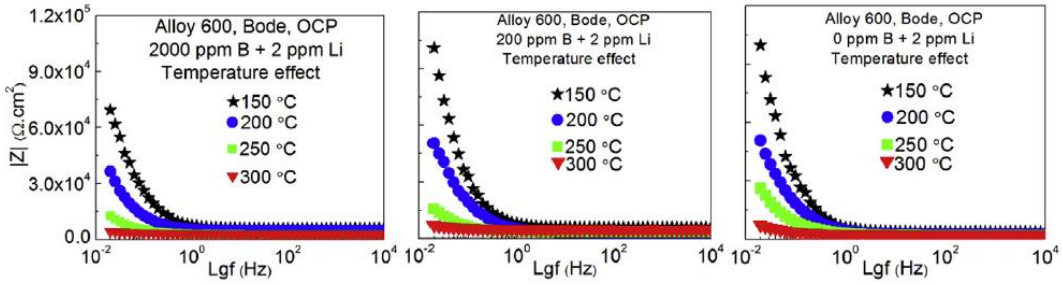

Fig. 22 The effect of temperature on the absolute impedance [44].

Chapter III

Experimental

3.1. Material and powder preparation

Starting powder for hydrogen electrode was prepared. The compositions of the Ni–Cr–Fe/YSZ were varied with a constant ratio of total metal to YSZ (wt%) at 60:40. For Ni_x-Fe_{1-x}/YSZ and Ni_x-Cr_{1-x}-YSZ, x was in a range of 0-20 wt% as shown in Table 8. It should be noted that in Sample 9 (Ni-Fe-Cr/YSZ), the Fe-Cr composition was chosen following a composition of SOFC's interconnect [7] and steam-corrosion resistance tube [39]. To prepare the starting powder, NiO (Sigma-Aldrich, USA) and metal (Cr50/Ni50, CRO26010/2, Sigma-Aldrich, USA or Fe50/Ni50, Fe076020/1, Sigma-Aldrich, USA) were mixed in ethanol. The mixture was ball-milled for 24 hr to form a uniform slurry, followed by drying and grinding. Polyvinylpyrrolidone (PVP10) was introduced to modify the strength of Ni alloy based electrode [45]. The amount of PVP 10 was 5 %vol/vol in ethanol.

จุฬาลงกรณ์มหาวิทยาลัย
CHULALONGKORN UNIVERSITY

Table 8 Composition of Ni-Fe-Cr/-YSZ

Composition	Conventional (wt%)	Sample 1 (wt%)	Sample 2 (wt%)	Sample 3 (wt%)	Sample 4 (wt%)
Ni	60	55	50	45	40
Fe	0	5	10	15	20
Cr	0	0	0	0	0
YSZ	40	40	40	40	40

Composition	Sample 5 (wt%)	Sample 6 (wt%)	Sample 7 (wt%)	Sample 8 (wt%)	Sample 9 (wt%)
Ni	55	50	45	40	40
Fe	0	0	0	0	2
Cr	5	10	15	20	18
YSZ	40	40	40	40	40

3.2. Cell fabrication

3.2.1. Fabrication of a conventional SOEC

Conventional Ni-YSZ was prepared by dry pressing method. 10 wt% of starch powder was added as a pore former to form an adequate porosity of porous cathode (Ni-YSZ at 60:40 wt%) [46]. The mixed powder was pressed into a disc with diameter of 2.54 cm under of 10 MPa for 30s. The green disc was pre-sintered at 1,100 ℃ for 2 hr. Then, electrolyte was deposited on one side of the pre-sintered cathode using dip-coating technique. The other side of electrode was covered by the plastic tape. The electrolyte slurry composition is shown on Table 9. After depositing electrolyte, the cell was sintered at 1,450 ℃ for 4 hr to form dense layer of YSZ. The $Ba_{0.5}Sr_{0.5}Co_{0.8}Fe_{0.2}O_{3-\delta}$ (Kceracell, Republic of Korea) was used as an oxygen electrode which was deposited using doctor blade technique and sintered at 950 ℃ for 2 hr to

form a thin layer on the sintered YSZ with an effective area of 0.5 cm^2. The oxygen electrode slurry was made by mixing BSCF powder with alpha terpineol at the weight ratio of 1:1. The flow diagrams were shown in Fig. 23-25.

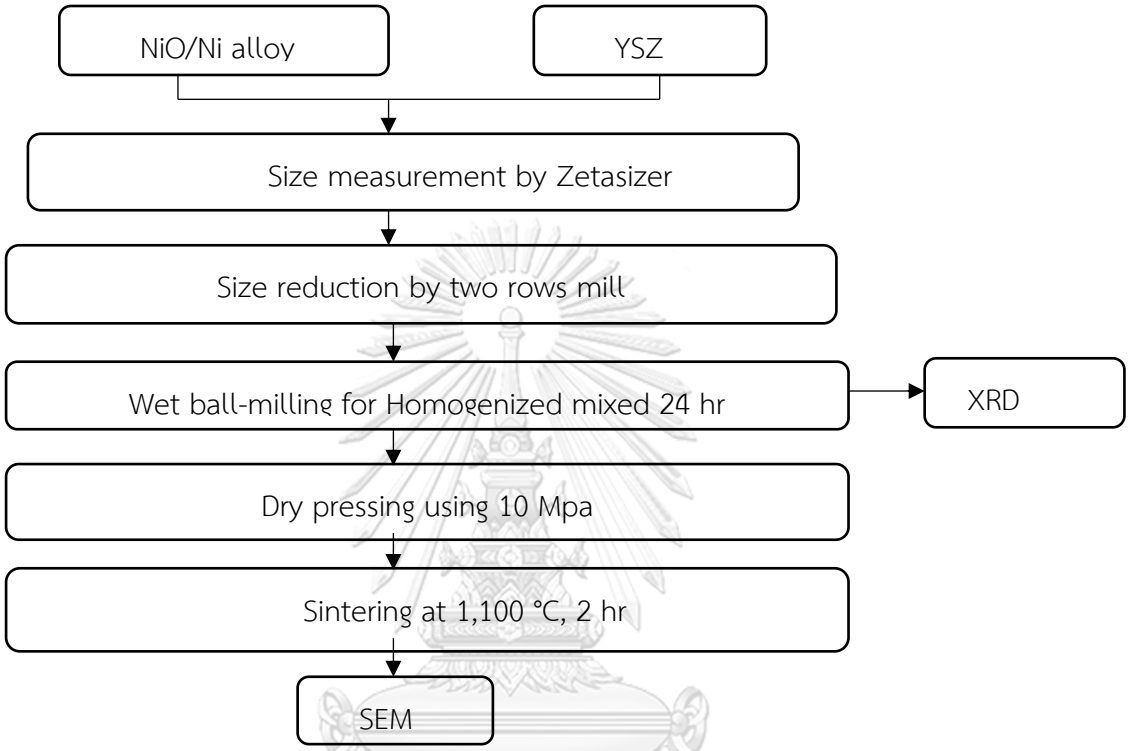

Fig. 23 Preparation of Ni Alloys-YSZ hydrogen electrode

จุฬาลงกรณ์มหาวิทยาลัย
Chulalongkorn University

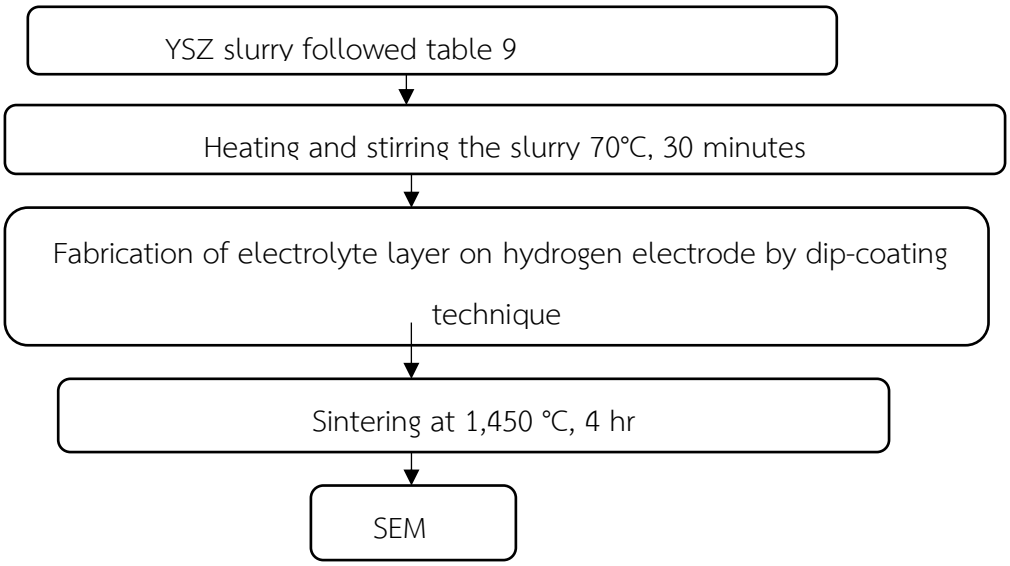

Fig. 24 Electrolyte layer fabrication on hydrogen electrode

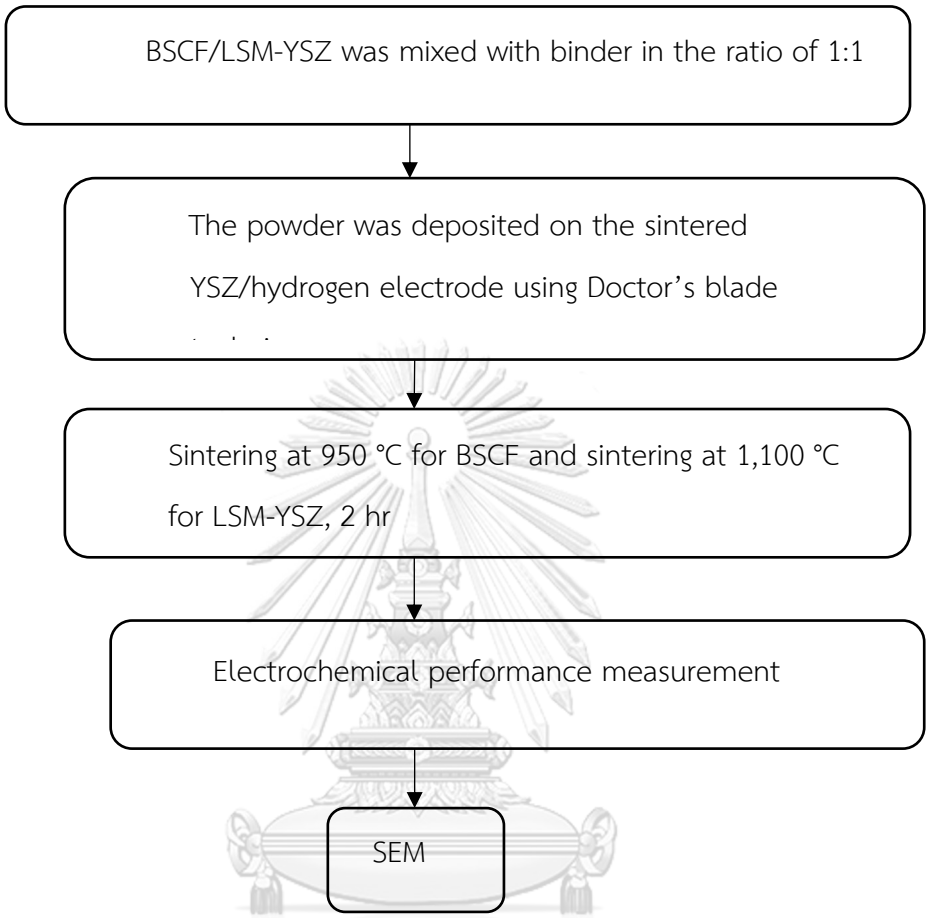

จุฬาลงกรณ์มหาวิทยาลัย
Chulalongkorn University

Fig. 25 Oxygen electrode fabrication on sintered YSZ/hydrogen electrode

Table 9 YSZ electrolyte slurry composition

YSZ (g)	Solvent System		Polyvinyl butyral resin (butar98) (g)	Polyethylene glycol (g)	Polyvinyl pyrrolidone (g)
	Xylene (ml)	Buthyraldehyde (ml)			
10	36.3	11	0.3	0.002	0.5

3.2.2. Fabrication of SOEC having Ni-alloy as a component in cathode

To prevent oxidation of Ni in cathode under high steam partial pressure, the SOEC having Ni alloy containing cathode was fabricated. The cell fabrication was divided into 3 types having different cathodes: 1) The cathode was fabricated from Ni-alloys/YSZ powder; 2) The cathode was fabricated from Ni-alloys washed coated Ni-YSZ powder; and, 3) The fabricated Ni-YSZ cathode was impregnated by Ni-alloys.

3.2.3. Fabrication of SOEC having Ni-alloy /YSZ cathode

Sample 1-8 were used to fabricate the Ni-based alloy cathodes (Ni-Fe/YSZ or Ni-Cr/YSZ) by dry pressing. For cathode-supported cell, the mixed powder was pressed into a disc with diameter of 2.54 cm under of 10 MPa for 30s, similar to the conventional SOEC in 3.2.1. The green disc was pre-sintered at 1,100 °C for 2 hr. For electrolyte-supported cell, the electrolyte disc was prepared by pressing YSZ powder into a disc and then sintered at 1,450 °C for 4 hr. The powders (Table 8) were mixed with the alpha terpineol (Sigma-Aldrich, USA) in the weight ratio of 1:1 to form a cathode slurry. The cathode slurries were then painted by doctor blade technique on the electrolyte. For oxygen electrode in the electrolyte-supported cell, platinum paste (70 wt% Pt loading, Nexceris, USA) was used and painted in the same way as the cathode.

จุฬาลงกรณ์มหาวิทยาลัย
CHULALONGKORN UNIVERSITY

3.2.3.1. Fabrication of SOEC having the cathode fabricated from Ni-alloy washed coated Ni-YSZ powder

Alternative method to prevent the oxidation while minimizing thermal expansion issue was used. Ni-YSZ powder were wash-coated by Ni-alloy slurry before fabricated into the cathode. The sintered Ni-YSZ was wash-coated by the alloy slurry. The slurry was prepared with the same composition as electrolyte slurry, presented in

Table 9, except Ni alloy powder was used instead of YSZ. Ni-alloy: containing 72 wt% Ni, 14-16 wt% Cr and 6-10 wt% Fe (66 wt% Ni, 30 wt% Cr and 4 wt% Fe confirmed by XRF) with the ratio of Ni alloy to YSZ at 60:40 wt%. This composition of alloy is called Alloy 600. It is generally used to prevent steam oxidation in various kind of work [39, 44]. The slurry was stirred with Ni-YSZ powders, 100℃ 4 hr. Then the wash-coated powder was dried in the oven at 110 ℃ for 24 hr.

3.2.3.2. Fabrication of SOEC having Ni-alloy impregnated Ni-YSZ cathode

Alternative method was to introduce Ni-alloy composition after the cell was fabricated. Ni-YSZ cathode in the fabricated cell was impregnated by Ni alloy slurry. It was relatively more simple method, especially when considering that the starting powder containing Ni alloy composition was rather difficult to be fabricated. The slurry was prepared by using the same Ni alloys loading as the wash-coated technique. The loading was 1.71 mg Ni alloys-YSZ per cm^2.

3.3. Characterization

จุฬาลงกรณ์มหาวิทยาลัย
CHULALONGKORN UNIVERSITY

The oxidation resistances were studied by thermogravimetric analysis (TGA, TA Instruments SDT Q600). The metal alloy/YSZ electrodes were tested under extremely condition in air at operating temperature of 800 ℃. Before TGA measurement, the starting powder was reduced under 30%H_2/N_2 at 800°C for 2 hr to convert metal oxide into metal. The degree of oxidation [35] can be calculated from weight gain of the sample as presented in equation (7).

$$\text{Degree of oxidation (t)} = \frac{m_{(t)} - m_{Ni-YSZ}}{m_{NiO-YSZ} - m_{Ni-YSZ}} \qquad (7)$$

Where $\mathbf{m_{Ni-YSZ}}$ is the initial mass of the reduced sample, $\mathbf{m_{(t)}}$ is the mass of the sample at time t during the oxidation and $\mathbf{m_{NiO-YSZ}}$ is the mass of fully oxidized sample.

The binding energies of samples were observed by x-ray photoelectron spectra (XPS, Kratos Analytical - AMICUS) using Mg anode emission 20 mA, Accel HT 10 kV.

The Sample crystallite characteristic was performed by X-ray diffraction (XRD, Brunker D8 Advance powder X-ray diffractometer) with a Cu-target X-ray tube (40 kVm 30 mA) and angle of 2θ range from 20 - 80 degree (scan step 0.02°). The crystallite sizes were calculated by the Scherrer equation (2).

$$\mathbf{B(2\theta) = \frac{K\lambda}{L \cdot Cos\theta}} \qquad (8)$$

Where L is crystallite dimension, B is the peak width in radians, θ is the Bragg angle and K is a Scherrer constant.

Temperature programmed reduction (TPR, micromeritics chemisorp 2750 pulse chemisorption system) was performed. In the experiment, 0.05 grams of the sample was placed in a quartz tube and preheated at 300 ℃ in a flow of nitrogen before further heated to 850 ℃ with a heating rate of 10 ℃/minhr under a flow of 10% H_2/argon.

จุฬาลงกรณ์มหาวิทยาลัย
Chulalongkorn University

Morphology of electrodes was analyzed by scanning electron microscope (SEM, Hitachi S-3400N JEOL model S-3400). The magnification used is range from 800 to 5000 times.

3.4. Electrochemical performance measurement

Single cell polarization curves were generated using linear sweep techniques. A potentiostat/gavanostat (Metrohm Autolab, Utrecht, The Netherlands) was used to control the voltage between 0.5 and 1.8 V with a scan rate of 20 mV/s. Electrochemical impedance spectroscopy (EIS) measurements were functioned using a sinusoidal signal amplitude of 20 mV_{rms}, across the frequency range of 100 kHz to 0.1 Hz. The equivalent circuit for the impedance response fitting is shown in Fig. 26. The feed contained humidified hydrogen at cathode chamber using varied steam to hydrogen (60:40, 70:30 and 80:20) when operating temperature was maintained at 800 °C (see Table 10).

The electrical connection was made to the cell electrodes via platinum wires and paste. The cell ridge was sealed using gas sealant (Ceramabond 552, Aramco, Houston, TX, USA) to create a separation of the gas environment of two electrodes. Fig. 27 shows the experimental set-up for the delivery of the gas to the cell in the furnace. The feed of H_2, H_2O and N_2 with various of composition were allowed to be introduced to the H_2 electrode. N_2 was used to balance the gas flow and control the steam ratio in the gas compositions. Deionized water was transferred using an HPLC liquid pump (Teledyne SSI, State College, PA, USA). Steam was generated in a heated tube and mixed with the N_2 and H_2 lines.

จุฬาลงกรณ์มหาวิทยาลัย

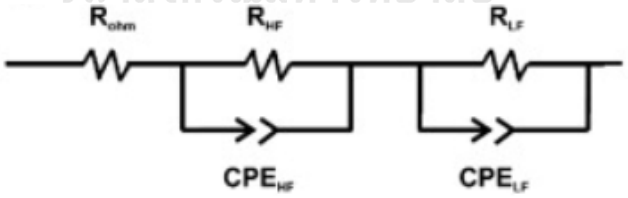

Fig. 26 Equivalent circuit for impedance response fitting [47]

Table 10 steam to H_2 ratio of operating condition

Steam to H_2 ratio	H_2 flow (ml/min)	N_2 flow (ml/min)	Steam flow (ml/min)	Total flow (ml/min)
60:40	20	100	30	150
70:30	20	83	47	150
80:20	20	50	80	150

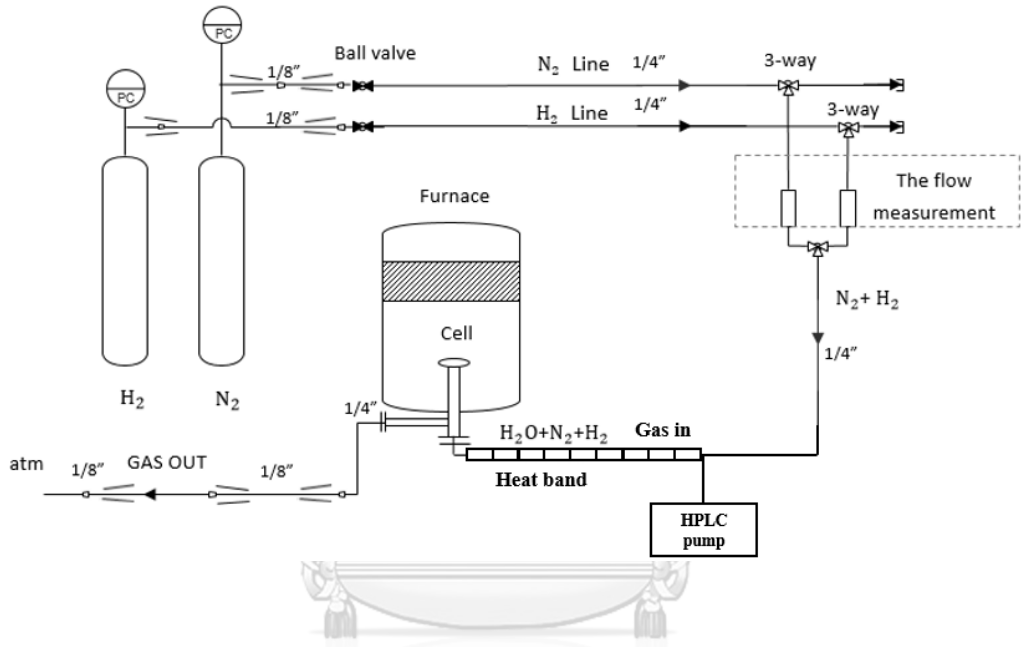

Fig. 27 Schematic drawing of the test system

จุฬาลงกรณ์มหาวิทยาลัย
CHULALONGKORN UNIVERSITY

The open circuit voltages (OCV) are calculated by Nernst equation [48, 49] expressed by equation (3)

$$E = E^0 - \frac{RT \ln\left(\frac{p_{H_2O}}{p_{H_2}\sqrt{p_{O_2}}}\right)}{nF} \qquad (9)$$

when E is the cell potential at the interested temperature, E^0 is the standard cell potential, R is the universal gas constant (8.314 $JK^{-1}mol^{-1}$), T is the temperature in

kelvins, n is the number of electron transferred and F is Faraday constant (96485 C mol^{-1}) The calculated OCV of 70:30 steam to hydrogen ratio at each operating temperature are shown in Table 11. The calculated OCVs were corresponded with Chiodelli and Malavasi [50]

Table 11 The calculated OCV at operating temperature

Operating temperature, °C	Calculated OCV, V
650	0.95
700	0.94
750	0.92
800	0.90
850	0.88
900	0.87

จุฬาลงกรณ์มหาวิทยาลัย
CHULALONGKORN UNIVERSITY

Chapter IV
Result and discussion

4.1. Thermogravimetric analysis (TGA)

The oxidation resistance was observed using TGA. Figs 28(a) and 28(b) show the degree of oxidation of the binary metals and ceramic (Ni-Fe/YSZ and Ni-Cr/YSZ), comparing to conventional Ni-YSZ. Increasing Fe content significantly reduced oxidation rate of the cathode. It should be noted that when increasing Fe content, Ni content decreased. Fe was reported to exhibit a higher oxidation tolerance than Ni [38]. For Ni-Cr/YSZ, increasing Cr content decreased oxidation tolerance. However, 5 wt% Cr addition decreased the oxidation resistance of the cathode when compared to conventional Ni-YSZ. Hamdani [39] also reports the fluctuation trends in weight gain measurement For Ni Cr alloys. In this study, the oxidation tolerance of 0-30 wt% Cr loading in Ni-Cr alloys are studied. Ni-26Cr of mirror and electro polished demonstrates the best oxidation resistance. Fig. 28(c) and (d) show the degree of oxidation of Alloy 600-YSZ compared to conventional Ni-YSZ in air atmosphere at 800 °C and ramping from room temperature-800 °C, respectively. There was no difference was seen between both electrode at 800 °C due to severe oxidation condition. However, it can be seen in Fig. 28(d) when the temperature was ramp from room temperature to 800 °C, Ni alloy-YSZ exhibited relatively higher oxidation resistance than the conventional Ni-YSZ.

จุฬาลงกรณ์มหาวิทยาลัย
Chulalongkorn University

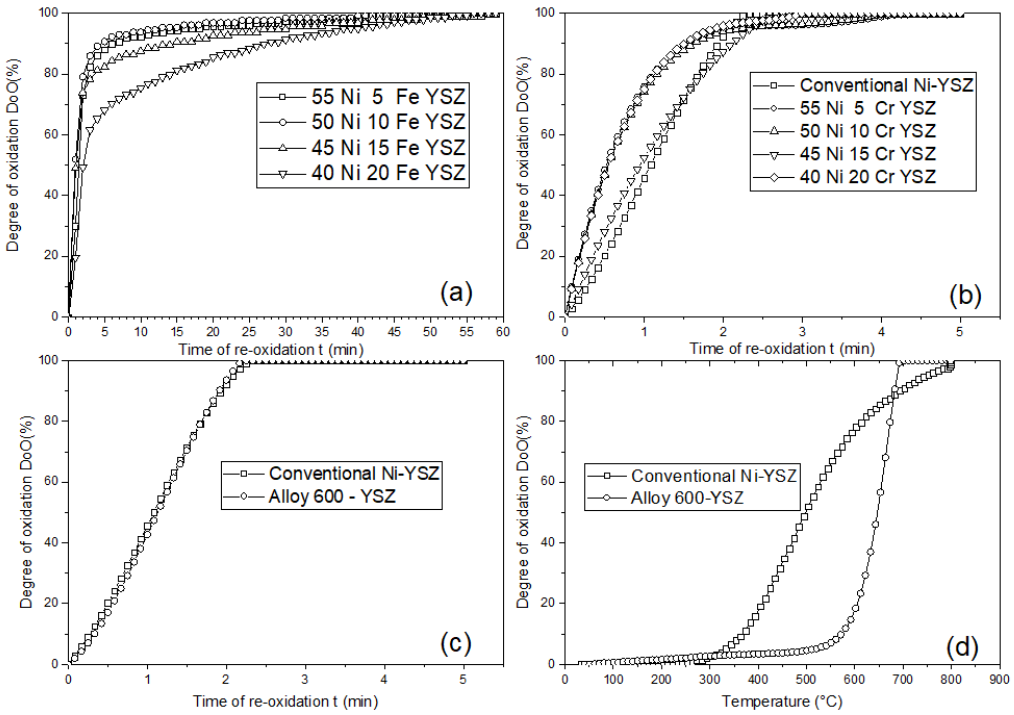

Fig. 28 Degree of oxidation (%) of: (a) Ni-Fe-YSZ; (b) Ni-Cr-YSZ; (c) Ni alloy: containing 72 wt% Ni, 14-16 wt% Cr and 6-10 wt% Fe with the ratio of Ni alloy to YSZ at 60:40 wt% compared to conventional Ni-YSZ in air atmosphere at 800 °C; and, (d) Ni alloy-YSZ compared to conventional Ni-YSZ in air atmosphere from room temperature – 800 °C.

จุฬาลงกรณ์มหาวิทยาลัย
Chulalongkorn University

4.2. X-ray photoelectron spectra (XPS)

The starting powder of hydrogen electrode was characterized by XPS. Fig. 29 shows the valence state of Ni $2p_{1/2}$, Ni $2p_{3/2}$, Cr $2p_{3/2}$ and Fe$2p_{3/2}$ of NiCr-YSZ) and NiFe-YSZ. The XPS of Ni $2p_{1/2}$ and Ni $2p_{3/2}$ spectra can be distinguished into 4 peaks as can be seen in Fig 29(a) and 29(b) for NiCr-YSZ and NiFe-YSZ, respectively. The negative shift refers to the lower electronegativity of the chromium and iron ion. As presented in Fig. 29(c), the peak position of the Cr $2p_{3/2}$ spectra from 5, 10, 15 and 20 wt% Cr

were 578.3, 577.8, 576.9 and 577.3 eV, respectively. the binding energy peak position of the Cr $2p_{1/2}$ spectra from 5, 10, 15 and 20 wt% Cr were 588.4, 587.5, 586.7 and 586.2 eV, respectively. The valence state at lower and higher Cr loading were identified as Cr^{6+} and Cr^{3+}, respectively. Fig. 29(d) show the XPS of $Fe2p_{3/2}$ spectra. The peaks were unclear in the low Fe composition (5 wt%). The binding energy peak positions of the Fe $2p_{3/2}$ spectra were around 710 to 715 eV, indicating a Fe^{3+}. The reference of binding energy peak positions of Cr and Fe were obtain from the study of Sainio et al. [51] and Yamashita et al. [52], respectively.

Then the devolution of Cr spectra was plotted and shown in Fig. 30. The peaks at 577.4 and 579.9 eV in $Cr2p_{3/2}$ can be assigned to Cr^{3+} and Cr^{6+}, respectively. The peaks at 586.9 and 588.9 eV in $Cr2p_{1/2}$ can be assigned to Cr^{3+} and Cr^{6+}, respectively. As seen in Table 12, the ratio of Cr^{6+}/Cr^{3+} decreased with the increasing of Cr content. The electronic conductivity may increase with increasing ionic radius [53]. The devolution of Fe spectra was undefined due to the low amount of Fe content. Then, Ni spectra was deconvoluted as seen in Fig. 31. The intensity of NiFe sample was higher than the NiCr sample. The metallic Ni peaks were found at 874.9 eV. The others were identified as a Ni^{2+}. After that the compositions of Ni-Fe-Cr/YSZ were calculated from the integrated area of XPS peaks. The data was shown in Table 13. Ni has a lower content than the expectation while YSZ was higher. This indicates that the prepared powders were not homogeneously mixed.

จุฬาลงกรณ์มหาวิทยาลัย
Chulalongkorn University

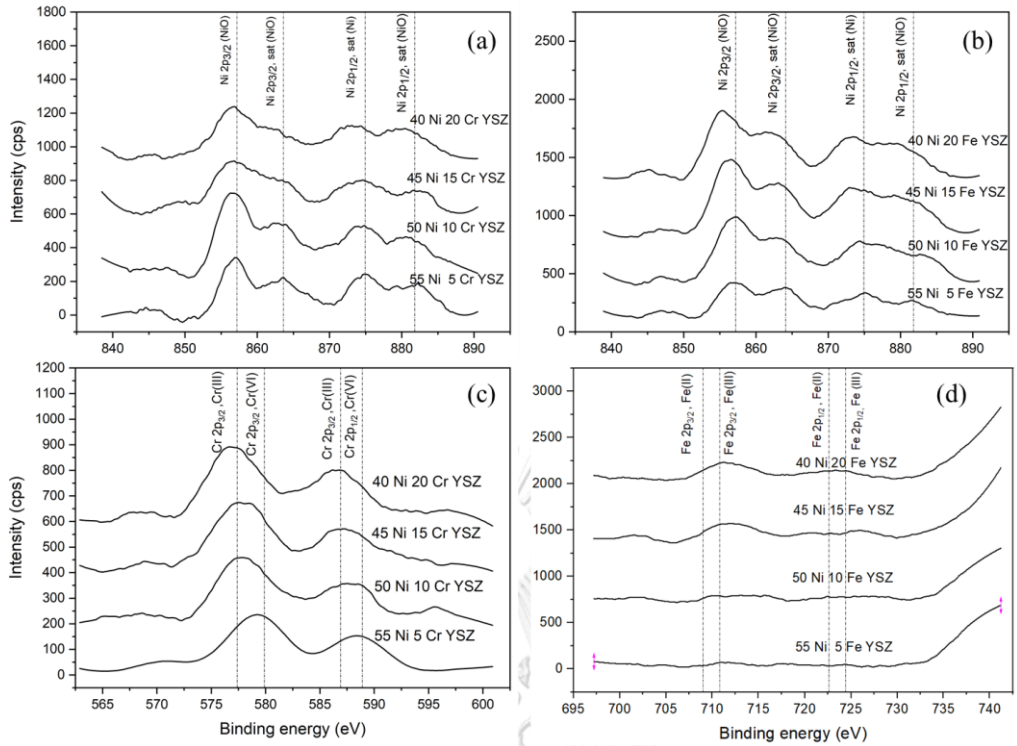

Fig. 29 The XPS of different Fe and Cr loading Ni-YSZ electrodes: (a) Ni spectra of NiCr-YSZ; (b) Ni spectra of NiFe-YSZ; (c) Cr 2p3/2 spectra of NiCr-YSZ and (d) Fe 2p3/2 spectra of NiFe-YSZ

จุฬาลงกรณ์มหาวิทยาลัย
Chulalongkorn University

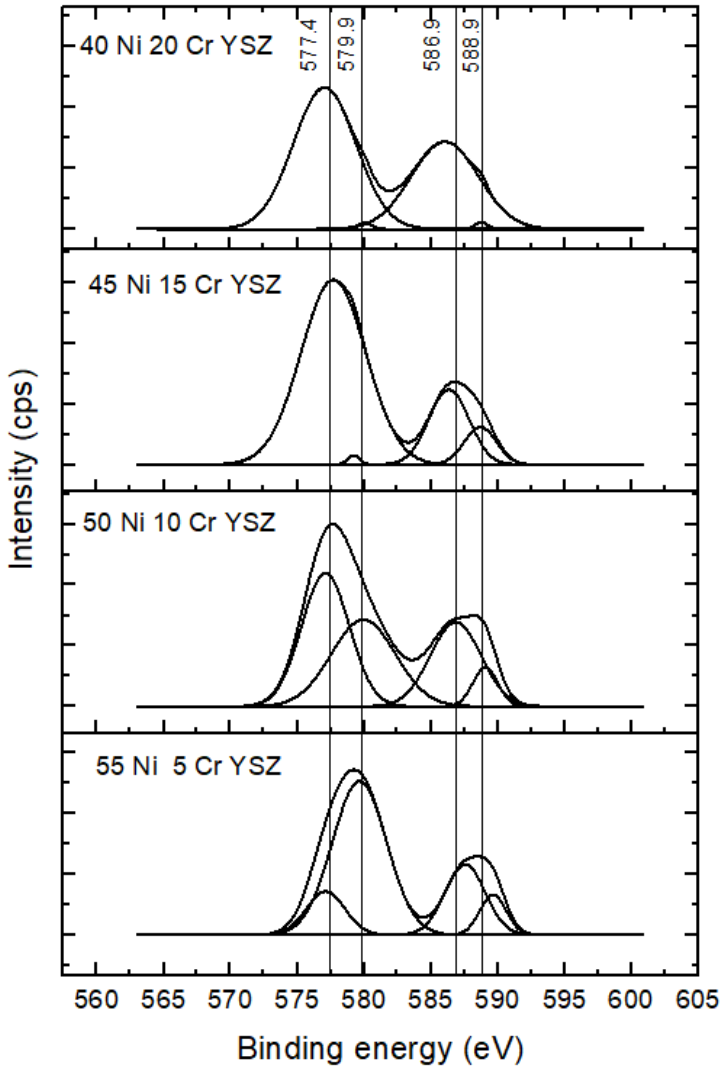

จุฬาลงกรณ์มหาวิทยาลัย
Chulalongkorn University

Fig. 30 The deconvolution of Cr XPS spectra of various NiCr-YSZ composition

Table 12 The ratio of Cr^{6+}/Cr^{3+} of the various NiCr-YSZ composition

Composition	The ratio of Cr^{6+}/Cr^{3+}
55 Ni 5 Cr YSZ	2.09
50 Ni 10 Cr YSZ	0.61
45 Ni 15 Cr YSZ	0.08
40 Ni 20 Cr YSZ	0.01

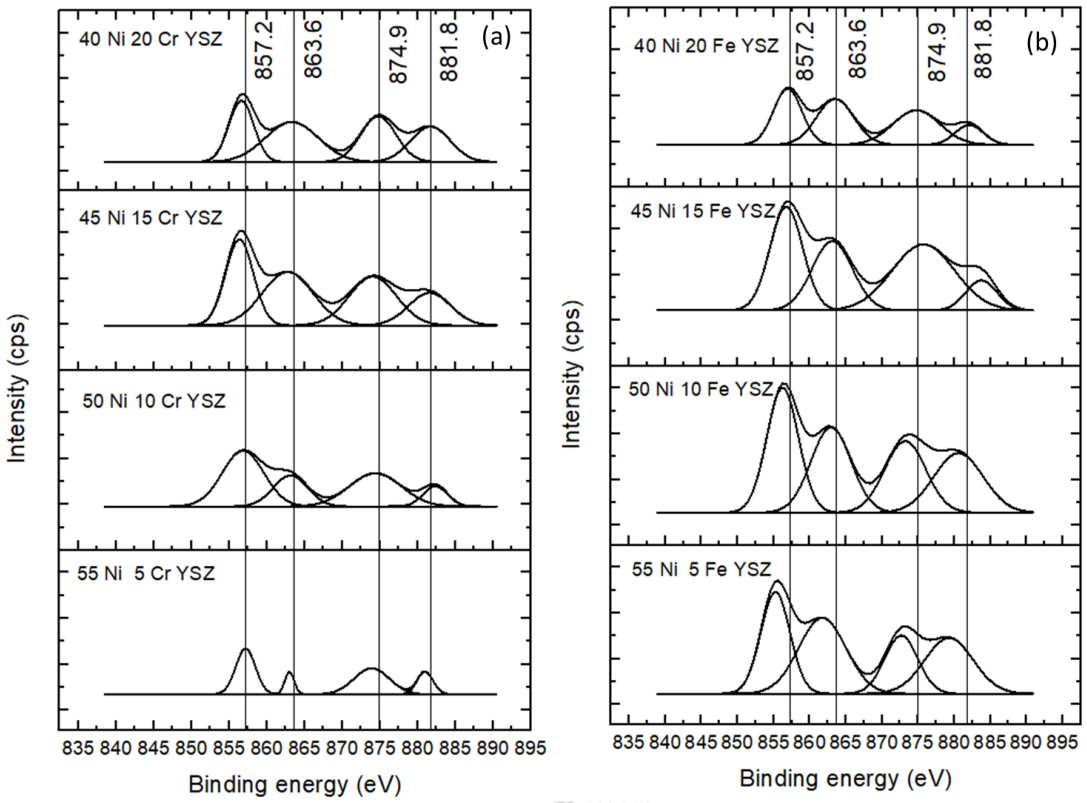

Fig. 31 The deconvolution of Ni XPS spectra of various (a) NiCr-YSZ and (b) NiFe-YSZ composition

Table 13 Composition of Ni-Fe-Cr/-YSZ obtained from XPS

Composition	Ni 2p (wt%)	Cr 2p (wt%)	Zr 3d (wt%)	Y 3d (wt%)
55 Ni 5 Cr YSZ	16.97	17.42	51.65	13.96
50 Ni 10 Cr YSZ	29.69	16.39	46.34	7.58
45 Ni 15 Cr YSZ	14.49	19.02	51.59	14.91
40 Ni 20 Cr YSZ	15.54	25.69	45.86	12.91
Composition	**Ni 2p (wt%)**	**Fe 2p (wt%)**	**Zr 3d (wt%)**	**Y 3d (wt%)**
55 Ni 5 Fe YSZ	13.89	16.80	50.99	18.33
50 Ni 10 Fe YSZ	21.41	14.94	53.01	10.64
45 Ni 15 Fe YSZ	13.85	14.01	59.20	12.94
40 Ni 20 Fe YSZ	18.72	10.77	59.81	10.70

4.3. X-ray powder diffraction (XRD) and X-ray Fluorescence analysis

XRD patterns of sintered NiCr-YSZ and NiFe-YSZ cathode having various Cr or Fe loading from 0 to 20 wt% (sintered at 1,100 °C for 2 hr) are presented in Fig. 32(a) and 31(b). A low-intensity peak of $NiCr_2O_4$ were detected in NiCr-YSZ (Fig 32(a)) while $NiFe_2O_4$ were detected in NiFe-YSZ (Fig 32(b)). In NiFe-YSZ sample, segregated Fe_2O_3 was also observed after the heat treatment. Similarly, the XRD pattern of alloy 600-YSZ also showed Fe_2O_3 phase. The peak location was corresponding well with the work of Qi [54]. The formation of $NiFe_2O_4$ in Ni-Fe system was also reported by Fiuza et al [55]. For 20Fe15Ni/YSZ-GDC and 30Fe5Ni/YSZ-GDC composition, the peaks at 43.6° 50.84° and 74.69° was suggested as Ni-Fe alloy with an FCC structure. The crystallite size was calculated by Scherrer equation (Eq.(8)). The average crystallite sizes of NiCr-YSZ with Cr loading from 0 to 20 wt% were 47.14 53.72 65.40 and 66.12 nm, respectively. The average crystallite size of NiFe-YSZ with Fe loading from 0 to 20 wt% were 36.65 37.49 43.06 and 51.39 nm, respectively. The average crystallite size was increased with the increasing of alloy content.

จุฬาลงกรณ์มหาวิทยาลัย
Chulalongkorn University

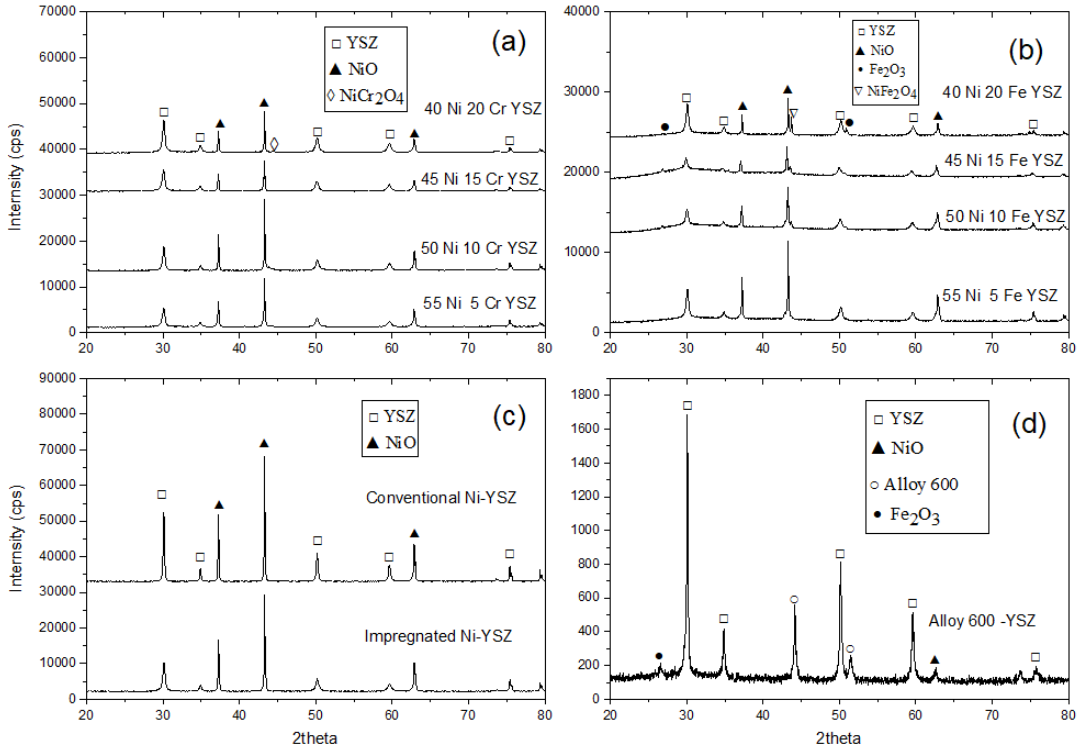

Fig. 32 pattern of sintered powder at 1,100 °C for 2 hr of (a) NiCr-YSZ (b) NiFe-YSZ (c) Impregnated Ni-YSZ compared to conventional Ni-YSZ and (d) Alloy 600-YSZ[56]

Figure 32(c) shows the XRD patterns of Ni alloys impregnated Ni-YSZ while Fig. 32(d) shows the XRD pattern of alloy 600-YSZ. The alloys peak was not detected. This may be caused by low amounts of Ni alloy loading and a well-mixed with YSZ forming a composite. The crystallite size of Ni alloys impregnated Ni-YSZ, Alloy 600-YSZ and conventional Ni-YSZ were 53.54 34.64 and 60.16 nm respectively. The alloys loading reduced the size of crystallite.

4.4. Hydrogen Temperature programmed reduction (H_2-TPR) analysis

The reducibility of NiCr-YSZ and NiFe-YSZ powders was investigated by hydrogen temperature programmed reduction (H_2-TPR). Fig. 33(a) and 33(b) show the H_2-TPR profiles of NiCr-YSZ and NiFe-YSZ, respectively. No peaks were detected at temperature below 400 °C. NiCr-YSZ samples exhibited only one reduction peak at around 500 to 700 °C, corresponding well with other work [57]. The peaks shift to the lower temperature when increasing the Cr content as seen in Fig. 33(a) [58]. The single dominant peak indicated that all the Cr^{6+} species were reduced into the oxidation state of Cr^{3+}. No further reducibility was found due to the Cr_2O_3 is the most difficult oxide to reduce into metallic Cr [59]. The reduction peaks of 5 wt% to 20 wt% Cr loading are located at 609, 605, 576 and 575 °C respectively.

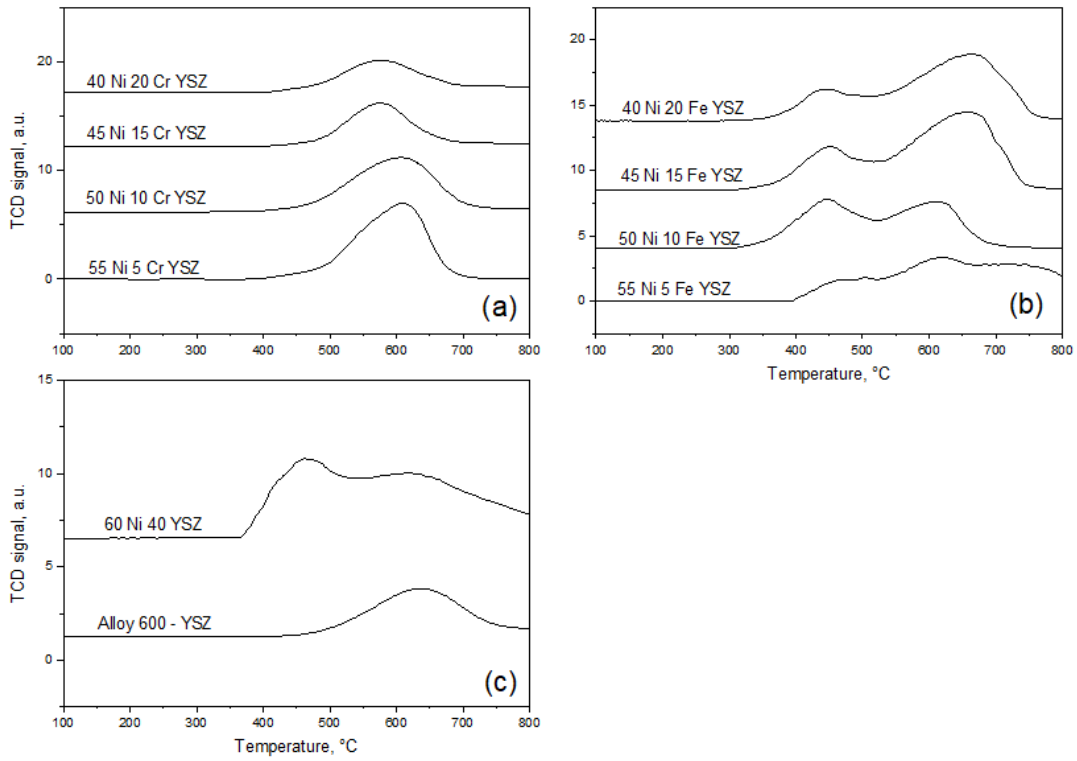

Fig. 33 Hydrogen TPR profile of cathode starting powder with different Cr or Fe loading from 5 to 20 wt%, sintered at 1,100 ℃ for 2 hr: (a) NiCr-YSZ and (b) NiFe-YSZ and (c) conventional Ni-YSZ and alloy

For NiFe-YSZ samples, there were two reduction peaks. All sample showed the first and second reduction peak around 400 ℃ and above 600 ℃, respectively. According to Al-Dossary et al. [60], The Fe_2O_3 can be reduced into two or even three steps. The reduction sequence is as follow: $Fe_2O_3 \rightarrow Fe_3O_4 \rightarrow [FeO] \rightarrow$ metallic Fe

The first step takes place around 400 ℃. It is a reduction of Fe_2O_3 (hematite) into Fe_3O_4 (magnetite). For the second peak is a reduction into FeO and metallic Fe phase which might coexist. High Fe loading increased the reduction temperature, corresponding to other work [61]. It should be noted that from the TGA result, increase Fe content also increased oxidation tolerance (Fig 28(a)). The first peak of 5 wt% to 20 wt% of Fe loading were located at 466, 449, 451 and 449 ℃, respectively. The second peak of 5 wt% to 20 wt% of Fe loading were located at 623, 624, 658 and 669 ℃, respectively. For conventional Ni-YSZ, The TPR profiles were in a broad range of 300 to 600 ℃ [62].

จุฬาลงกรณ์มหาวิทยาลัย
Chulalongkorn University

4.5. Scanning electron microscope (SEM)

When fabricating the hydrogen electrode directly from Ni alloy-YSZ starting powder, it was very difficult to fabricate the cell. Polyvinylpyrrolidone (PVP10) was introduced to modify the strength of Ni alloy electrode [45]. The amount of PVP 10 added is 5 %v/v of ethanol. Then the electrodes were sintered at 1,100 ℃ for 2 hr, using 5 ℃/min. The morphology of sintered hydrogen electrodes was shown on Fig. 34. The particle alignment and uniformity of NiCr-YSZ seemed better than NiFe-YSZ. Fabricated cathode from NiFe-YSZ was crack and therefore was not suitable for

electrolyte deposition. For NiCr-YSZ cathode, the particle was packed with the increasing of Cr loading. However, all NiCr-YSZ cathode was fragile and brittle. The study of Lopes et al. [63] shows that the metal-ceramic (Ni-Cr alloys -ceramic) bond strength is affected by the CTE. The high difference of CTE can leads to the bonding fail. After that the compositions of sample were obtained from EDX as seen in Table 14. This results also confirmed that the ball-milling's time was not enough to get the well mixed slurry. The conventional Ni-YSZ electrode has a bigger size particle compared to the impregnated electrode. Then, the morphology of Ni alloys wash-coated Ni-YSZ electrode was shown in Fig.34(k). The particles were formed into a dense grain which was not suitable to use as a cathode due to the lack of TPBs.

จุฬาลงกรณ์มหาวิทยาลัย
Chulalongkorn University

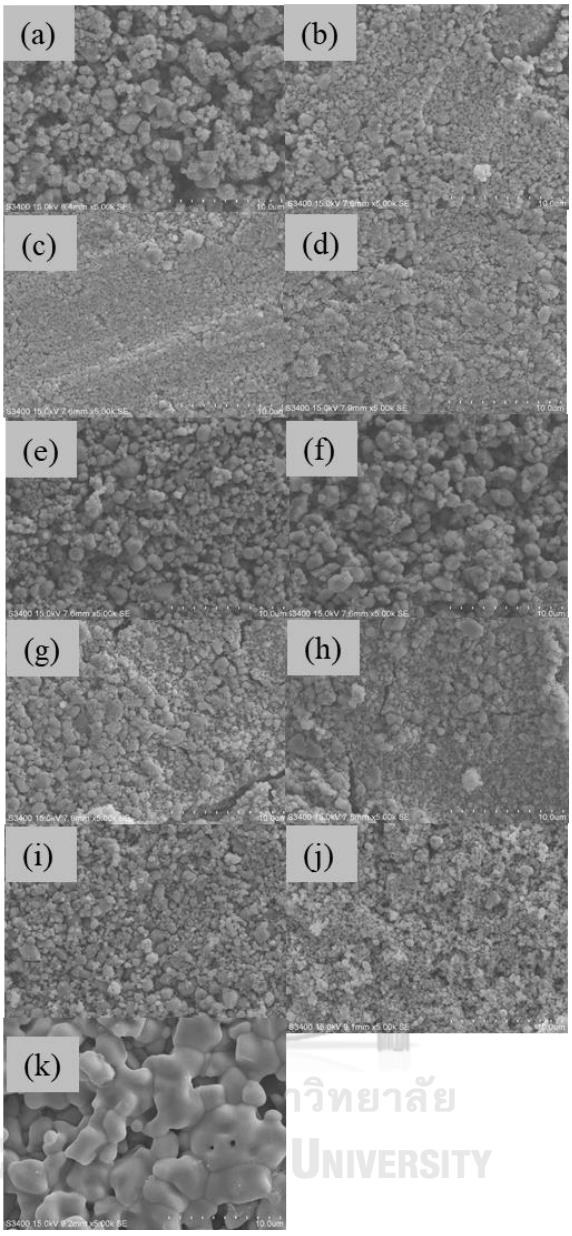

Fig. 34 SEM images at 5000X magnification of various Ni-Fe-Cr content in cathode sintered at 1100 ℃ for 2 hr, (a-d) sintered hydrogen electrode containing 5 to 20 wt% Cr, respectively, (e-h) sintered hydrogen electrode containing 5 to 20 wt% Fe, respectively, (i) sintered conventional electrode, (j) sintered Ni-alloys impregnated electrode and (k) sintered Ni alloys wash-coated electrode.

Table 14 Composition of Ni-Fe-Cr/-YSZ obtained from SEM-EDX

Composition	Ni(wt%)	Cr (wt%)	Y (wt%)	Zr (wt%)
55 Ni 5 Cr YSZ	58.46	4.99	3.32	33.22
50 Ni 10 Cr YSZ	42.56	4.19	5.83	47.43
45 Ni 15 Cr YSZ	38.50	7.92	5.69	47.88
40 Ni 20 Cr YSZ	20.93	13.67	7.30	58.1
Composition	**Ni (wt%)**	**Fe (wt%)**	**Y (wt%)**	**Zr (wt%)**
55 Ni 5 Fe YSZ	50.25	1.18	5.55	43.02
50 Ni 10 Fe YSZ	54.21	8.70	3.45	33.65
45 Ni 15 Fe YSZ	37.15	14.44	5.92	42.49
40 Ni 20 Fe YSZ	34.95	16.70	5.99	42.37

The fabrication of SOEC using direct Ni alloy-YSZ cathode as a support was not suitable due to its low strength and fragile property. However, for comparison of the electrochemical performance, YSZ electrolyte support cell was used. Electrolyte layer was fabricated using dry-pressing method and sintering at 1,450 ℃ for 4 hr using heating rate of 5 ℃/min. The sintered electrolyte thickness was about 2 mm. Then the cathode was painted by using doctor's blade technique. The cathode slurries consist of $Ni_{1-x}Cr_x$-YSZ and $Ni_{1-x}Fe_x$-YSZ, when x is varying from 5 to 20 wt%, and using alpha terpineol at 1:1 ratio as a binder. The sintered electrode was presented in Fig 35. The thickness of cathode layer was about 25 μm.

After sintering the NiFe-YSZ/YSZ (electrolyte support) at 1,100 ℃ for 2 hr with heating rate of 5 ℃/min, the cathode layer of NiFe-YSZ electrode was peel off due to the thermal expansion. The sintering electrode was shown in Fig. 35(e).

The Ni-alloy impregnated Ni-YSZ powder was fabricated into the cathode disc. The disc was easily to fabricate due to the lower content of the alloy. The sintering temperature was controlled by the same condition as conventional electrode. The undefined black dot appears as seen in Fig. 35(f). Phase change may occur at high sintering temperature of 1,100 °C. It is required for further investigation.

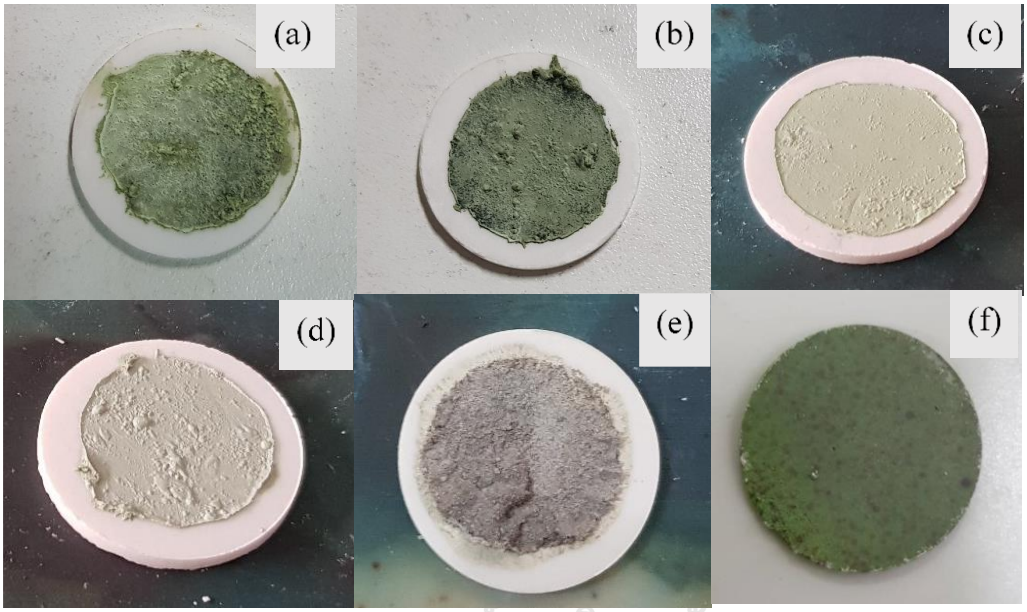

จุฬาลงกรณ์มหาวิทยาลัย
Chulalongkorn University

Fig. 35 Sintered hydrogen electrode on the electrolyte supporting layer at 1,100°C for 2hr, using 5 °C/min. (a-d) hydrogen electrode containing 5 to 20 wt% Cr respectively, (e) hydrogen electrode containing 5 %wt Fe loading , (f) Ni alloys impregnated Ni-YSZ cathode

The Alternative method to prevent the oxidation while minimizing thermal expansion issue was to impregnate conventional Ni-YSZ cathode with Ni alloy slurry. The impregnated slurry composition is shown in Table 9 but using Ni alloys instead of YSZ. The cross-sectional morphology of Ni-alloy impregnated Ni-YSZ/YSZ/BSCF before

and after electrochemical performance test was presented in Fig. 36. The impregnated layer was about 10.52 μm thick.

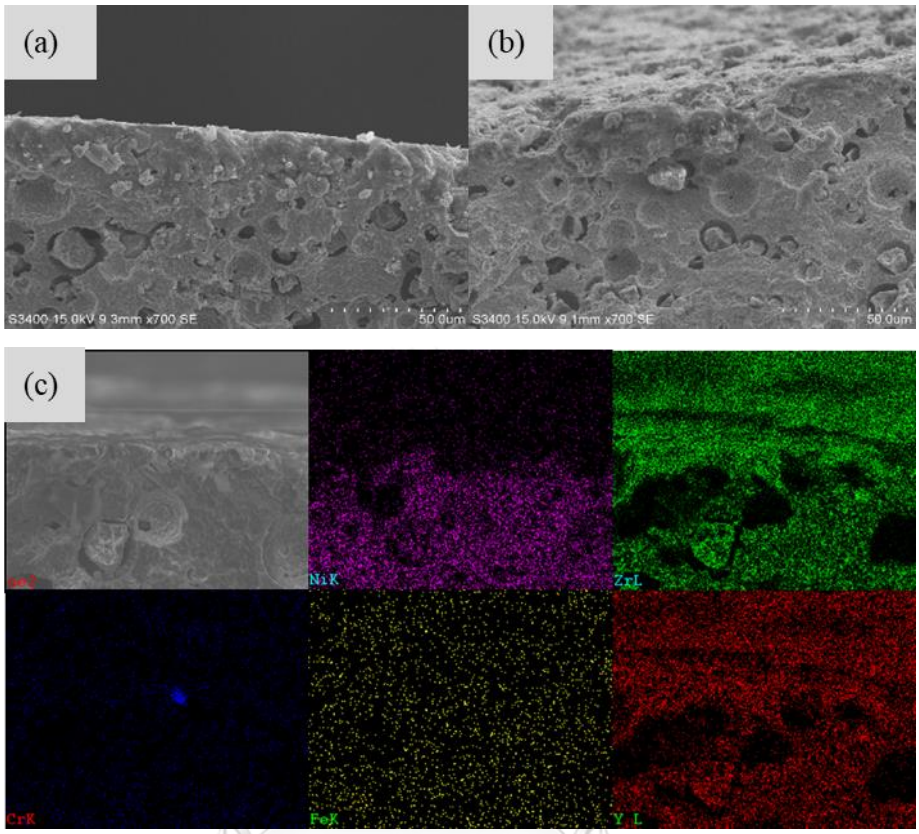

Fig. 36 SEM patterns at 700X magnification of Ni Alloy impregnated Ni-YSZ electrode (a) before and (b) after electrochemical performance test, and (c) the EDX mapping of Ni Alloy impregnated Ni-YSZ electrode

จุฬาลงกรณ์มหาวิทยาลัย
CHULALONGKORN UNIVERSITY

4.6. Electrochemical performance

The electrochemical performance of electrolyte supported conventional Ni-YSZ/YSZ/Pt and NiCr-YSZ/YSZ/Pt of varying Cr contents from 0 to 20 wt% are shown in Fig. 37(a-e) respectively. The measured OCV was slightly lower than the theoretical OCV calculated using Nernst equation (Eq. (9)). The OCV decreased with the increasing of operating temperature.

The linear sweep technique was used to describe the single polarization when operating potential was controlled from 0.6 to 1.8 V. The highest current density was obtained from the 55Ni 5Cr-YSZ/YSZ/Pt at various operating temperature from 650 to 900 °C. The electrochemical performance significantly increased above 800 °C. The performance increased with the increasing operating temperature. Increasing Cr content in the cathode decreased the electrochemical performance of the cell. It was reported that Cr-containing alloys can form a layer of chromatic scale which can protect the material from heavy oxidation. However, thicker layer of the scale can reduce the conductivity and contact in electrode [64]. However, under high partial pressure of steam at elevated temperature, Cr was reported to volatile and deposit on the cathode, leading to a loss of oxidation tolerance [65]. The small amount of Cr was reported to improve the adsorption and increase catalytic active sites [36, 66]. The higher Cr loading, the lower electronic conductivity.

จุฬาลงกรณ์มหาวิทยาลัย
Chulalongkorn University

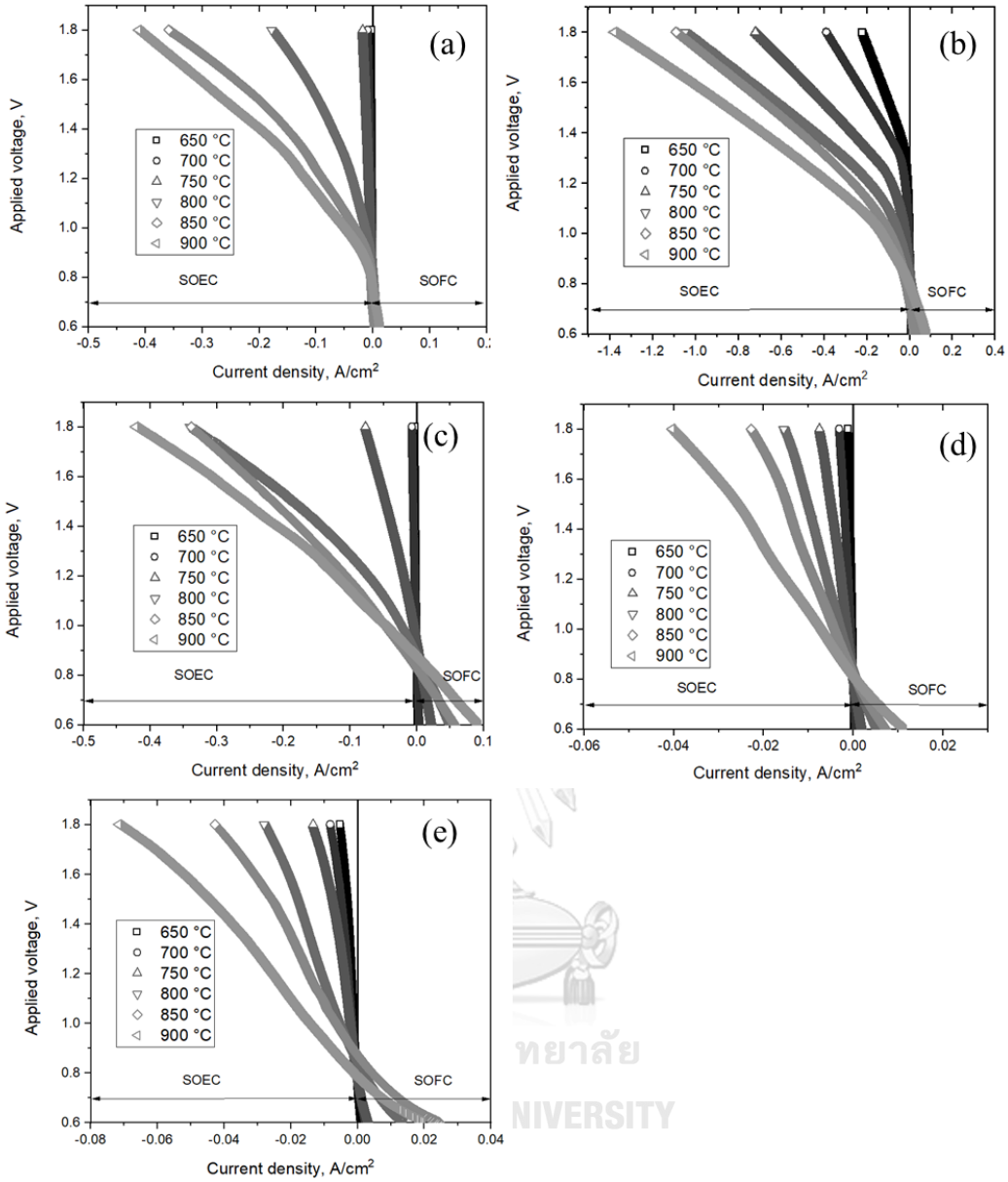

Fig. 37 Comparison of the electrochemical performance of various operating temperature and steam to H_2 ratio at 70:30 of (a) electrolyte-supported conventional Ni-YSZ/YSZ/Pt and (b-e) electrolyte-supported NiCr/YSZ/Pt with varying Cr contents from 5 to 20 wt%, respectively

The comparison of I/V profiles and electrochemical impedance response at OCV of various Cr contents from 0 to 20 wt% at operating temperature of 800 °C controlled steam to hydrogen ratio at 70:30 is presented in Fig. 38(a) and 38(b)

respectively. The highest current densities at 1.8 V of electrolyte-supported conventional Ni-YSZ/YSZ/Pt and NiCr/YSZ/Pt with varying Cr contents from 5 to 20 wt% were -0.12 -1.05 -0.34 -0.03 and -0.02 A/cm^2, respectively. For electrochemical impedance response, R_0, R_{HF} and R_{LF} are referred to Ohmic resistance and polarization resistance in high frequency region and low frequency region, respectively. The small amount of Cr loading such as 5 and 10 wt %Cr can be confirmed that it decreased the polarization resistance (HF and LF region) as seen in Fig. 38(b). The Ohmic resistance and polarization in both HF and LF region are shown in the Table 15. The frequency about 1-10 Hz represents the gas diffusion in hydrogen electrode, 10-200 Hz represent the oxygen electrode process such as chemical surface exchange of O_2 and O^{2-} bulk diffusion and a higher than 200 Hz represent charge transfer reaction and ionic transport in hydrogen electrode [67]. The addition of Cr loading should reduce the mass transport resistance due to the higher porosity while increase the activation resistance. The impedance arc cannot clearly distinguish these two characteristic resistances.

จุฬาลงกรณ์มหาวิทยาลัย

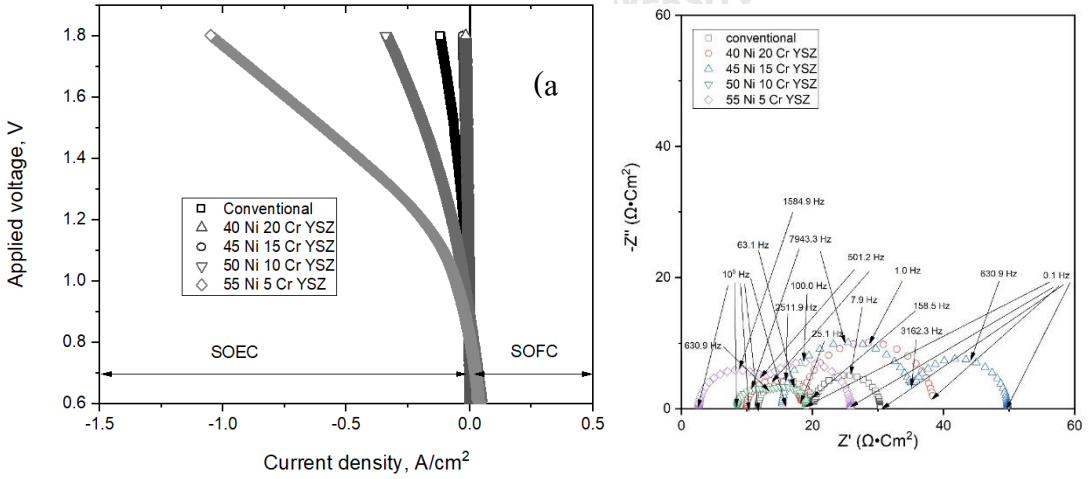

Fig. 38 Comparison of the electrochemical performance of various Cr contents from 0 to 20 wt% and steam to H_2 ratio at 70:30 of conventional at 800 °C (a) IV profiles and (b) electrochemical impedance response (EIS)

Table 15 Resistance of the various electrolyte support NiCr-YSZ/ YSZ/ Pt. R0, RHF and RLF are referred to ohmic resistance and polarization resistance in high frequency region and low frequency region, respectively.

Composition	NiCr-YSZ/ YSZ/BSCF (electrolyte support)			
	R_0 ($\Omega \cdot cm^2$)	R_{HF} ($\Omega \cdot cm^2$)	R_{LF} ($\Omega \cdot cm^2$)	Total R ($\Omega \cdot cm^2$)
Conventional 60 Ni 40 YSZ	11.67	14.48	12.19	38.34
55 Ni 5 Cr YSZ	10.41	8.24	7.16	25.80
50 Ni 10 Cr YSZ	9.64	12.94	10.26	32.84
45 Ni 15 Cr YSZ	9.08	9.02	22.60	40.70
40 Ni 20 Cr YSZ	10.40	12.38	29.37	52.15

The electrochemical performance of Ni-alloys impregnated Ni-YSZ/YSZ/BSCF and conventional Ni-YSZ/YSZ/BSCF were compared as shown in Fig. 39(a). Both OCV were slightly lower than the calculated value using Nernst equation. The calculated OCV should be around 0.87 V at operating temperature of 800 °C under steam to hydrogen ratio of 70:30. The measured OCV of Ni alloys impregnated and conventional are 0.80 and 0.82 V respectively.

จุฬาลงกรณ์มหาวิทยาลัย
Chulalongkorn University

The effect of operating temperatures was investigated between 650 and 900 °C as shown in Fig. 39(b). Increasing temperature increased the cell performance. Conventional cell exhibited relative higher performance than the impregnated cell. At higher operating temperature, the conventional electrode exhibited a better performance. This can be caused by a better electrocatalytic activity of Ni at high operating temperature as well as higher electronic conductivity of Ni compared to Fe and Cr at higher operating temperature [68]. The highest current density at 1.8V and

800 °C of conventional Ni-YSZ/ YSZ/ BSCF and impregnated Ni-YSZ/ YSZ/ BSCF was -0.50 and -0.26 A/cm^2, respectively.

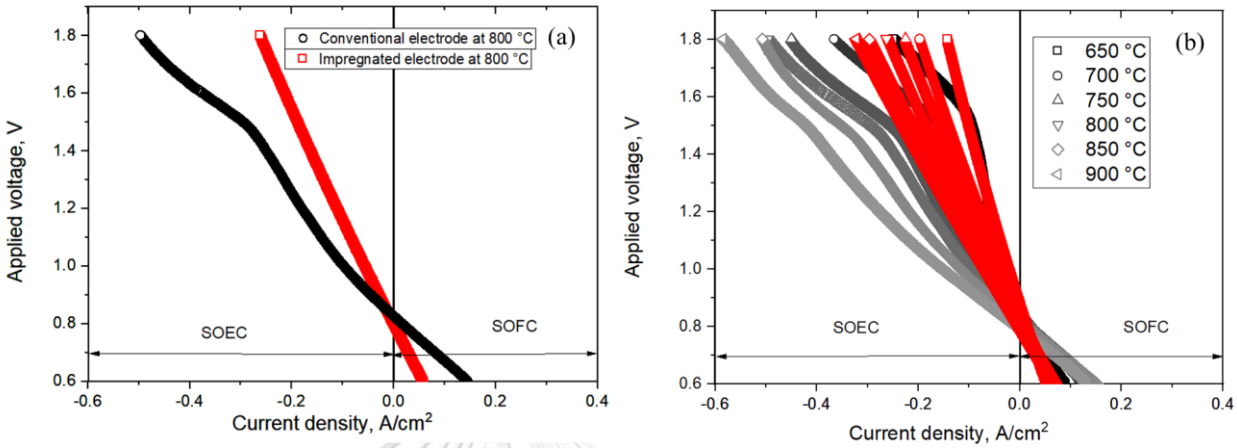

Fig. 39 Comparison of the electrochemical performance between (Red lines) Ni alloy impregnated Ni-YSZ/YSZ/BSCF electrode and (Black lines) conventional Ni-YSZ/YSZ/BSCF electrode using steam to H_2 ratio at 70:30: (a) at 800 °C and (b) from 650 °C to 900 °C

Fig. 40(a) shows a comparison of performance durability comparing between conventional Ni-YSZ/ YSZ/BSCF and Ni-alloys impregnated Ni-YSZ/YSZ/BSCF. After 48 hr of durability test, the impregnated Ni-YSZ/ YSZ/ BSCF shows lower degradation rate (0.7 mA/hr) than the conventional cell (0.9 mA/hr). Electrochemical impedance analysis is shown in Fig. 40(b). The resistances of the Ni alloy impregnated Ni-YSZ/YSZ/BSCF are shown in table 16. Ni alloy impregnated Ni-YSZ/YSZ/BSCF has higher ohmic resistance than conventional which may cause by the thickness of addition layer of impregnating. The resistance R_{HF} and R_{LF} of conventional electrode increase over operation time. But there are some fluctuation trends of obtained resistance from Ni alloy impregnated electrode. The R_{HF} trends to increase over time. However, R_{LF} trends to decrease. These can be caused by the agglomeration between Ni and alloys which

จุฬาลงกรณ์มหาวิทยาลัย
Chulalongkorn University

affects the activation resistance while increasing the porosity in the structure which lower the mass transport resistance.

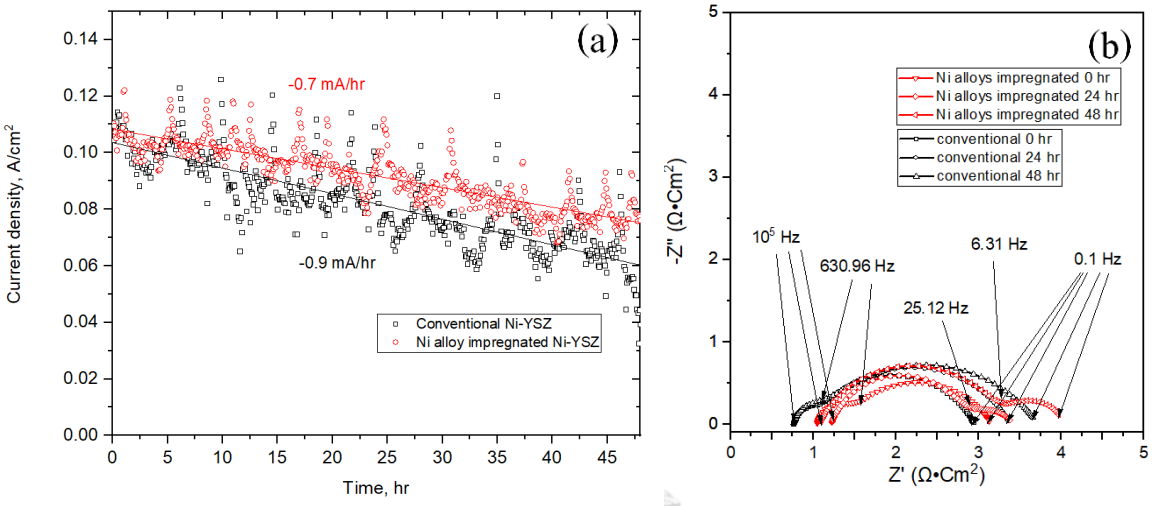

Fig. 40 Comparison of Ni alloy impregnated Ni-YSZ/YSZ/BSCF and conventional Ni-YSZ/YSZ/BSCF (a) the durability at applied 1.1 V and (b) electrochemical impedance response at different duration (800 °C and H_2O:H_2 = 70:30)

Table 16 Resistance of the Ni-YSZ/ YSZ/ BSCF and Ni alloys impregnated Ni-YSZ/ YSZ/ BSCF. R0, RHF and RLF are referred to ohmic resistance and polarization resistance in high frequency region and low frequency region, respectively.

Duration (hr)	conventional Ni-YSZ/YSZ/BSCF				Ni-alloy impregnated Ni-YSZ/YSZ/BSCF			
	R_0 ($\Omega\cdot cm^2$)	R_{HF} ($\Omega\cdot cm^2$)	R_{LF} ($\Omega\cdot cm^2$)	Total R ($\Omega\cdot cm^2$)	R_0 ($\Omega\cdot cm^2$)	R_{HF} ($\Omega\cdot cm^2$)	R_{LF} ($\Omega\cdot cm^2$)	Total R ($\Omega\cdot cm^2$)
0	0.76	0.35	1.80	2.91	1.11	0.59	1.32	3.02
24	0.76	0.38	2.19	3.33	1.23	1.66	0.49	3.38
48	0.76	0.39	2.51	3.66	1.08	2.23	0.66	3.97

Chapter V
Conclusion

Ni alloy containing Cr and Fe were introduced to improve the oxidation resistance of the conventional Ni-YSZ hydrogen electrode in solid oxide electrolysis cell. Oxidation tolerance, binding energy, crystallite size, reduction temperature, powder and electrode morphology were investigated. Electrochemical performance was measured. Increasing Fe content in the cathode improved the oxidation tolerance. However, the effect of Cr content shows unusual behavior in oxidation prevention and the similar trends of degree of oxidation with the conventional Ni-YSZ with Alloy 600-YSZ may cause by the difference surface area of the samples. The Alloy 600-YSZ begins to oxidize at 600 °C while conventional Ni-YSZ begins at 300 °C. The Cr^{6+} $Cr^{3+}$and Fe^{3+} were specified. The negative shifts of binding energy were referring to the lower electronegativity of the chromium and iron. The crystallite size and the alloy formation were investigated by XRD analysis. A small peak of $NiCr_2O_4$ and $NiFe_2O_4$ were detected. The addition of Alloys loading reduced the crystallite size compared to conventional Ni-YSZ.

จุฬาลงกรณ์มหาวิทยาลัย
Chulalongkorn University

The reducibility of NiCr-YSZ and NiFe-YSZ electrode were investigated. For NiCr-YSZ, only one TPR reduction peak was observed at around 500 to 700 °C. The negative peak shift was seen when increasing Cr contents, implying increasing reducibility. High Fe loading increased the reduction temperature. Various compositions of alloy content were used to fabricate the cathode-supported cell. Although densification of the cathode increased with increasing Cr, fabricated cathodes from alloys-YSZ were fragile and brittle. To measurement the performance of each composition, the electrolyte-

supported cell was then fabricated instead of the cathode support. NiFe-YSZ layer peeled off after sintering due to thermal expansion.

Electrochemical performance of electrolyte-support NiCr-YSZ/YSZ/Pt was investigated. The cell with the cathode with 5% Cr loading shows the highest current density at 800 ℃ compared to the other compositions. The current density was -1.09 A/cm^2 at operating voltage of 1.8 V using steam to hydrogen ratio of 70:30. The electrochemical performance of cathode-supported cells having the Ni alloy impregnated Ni-YSZ and the conventional Ni-YSZ were investigated. The highest current densities of Ni alloy impregnated Ni-YSZ and conventional Ni-YSZ at 1.8 V and 800 ℃ was -0.26 and -0.50 A/cm^2, respectively. While the electrochemical performance decreased in the Ni alloy impregnated Ni-YSZ, the durability was improved when compared to conventional Ni-YSZ.

จุฬาลงกรณ์มหาวิทยาลัย
Chulalongkorn University

REFERENCES

1. Energypedia. Thailand Energy Situation 2018 [cited 2020 02 Febuary]. Available from: https://energypedia.info/wiki/Thailand_Energy_Situation.

2. Fungtammasan B. THAILAND'S ENERGY SITUATION AND MAJOR CHALLENGES 2010 [cited 2020 02 Febuary]. Available from: http://stscholar.nstda.or.th/stscholar/csts/images/PDF/sem20130117.

3. Klotz D, Leonide A, Weber A, Ivers-Tiffée E. Electrochemical model for SOFC and SOEC mode predicting performance and efficiency. International Journal of Hydrogen Energy. 2014;39(35):20844-9.

4. Sapountzi FM, Gracia JM, Weststrate CJ, Fredriksson HOA, Niemantsverdriet JW. Electrocatalysts for the generation of hydrogen, oxygen and synthesis gas. Progress in Energy and Combustion Science. 2017;58:1-35.

5. Schiller G, Lang M, Szabo P, Monnerie N, von Storch H, Reinhold J, et al. Solar heat integrated solid oxide steam electrolysis for highly efficient hydrogen production. Journal of Power Sources. 2019;416:72-8.

6. Keane M, Fan H, Han M, Singh P. Role of initial microstructure on nickel-YSZ cathode degradation in solid oxide electrolysis cells. International Journal of Hydrogen Energy. 2014;39(33):18718-26.

7. Church BC, Sanders TH, Speyer RF, Cochran JK. Thermal expansion matching and oxidation resistance of Fe–Ni–Cr interconnect alloys. Materials Science and Engineering: A. 2007;452-453:334-40.

8. Ni M, Leung M, Leung D. Technological development of hydrogen production by solid oxide electrolyzer cell (SOEC). International Journal of Hydrogen Energy. 2008;33(9):2337-54.

9. Moçoteguy P, Brisse A. A review and comprehensive analysis of degradation mechanisms of solid oxide electrolysis cells. International Journal of Hydrogen Energy. 2013;38(36):15887-902.

จุฬาลงกรณ์มหาวิทยาลัย
Chulalongkorn University

10. Momma A, Kaga Y, Takano K, Nozaki K, Negishi A, Kato K, et al. Experimental investigation of anodic gaseous concentration of a practical seal-less solid oxide fuel cell. Journal of Power Sources. 2005;145(2):169-77.

11. O'Brien JE, Stoots CM, Herring JS, Lessing PA, Hartvigsen JJ, Elangovan S. Performance measurements of solid-oxide electrolysis cells for hydrogen production. Journal of Fuel Cell Science and Technology. 2005;2(3):156-63.

12. Shri Prakash B, Senthil Kumar S, Aruna ST. Properties and development of Ni/YSZ as an anode material in solid oxide fuel cell: A review. Renewable and Sustainable Energy Reviews. 2014;36:149-79.

13. Lv X, Chen H, Zhou W, Cheng F, Li S-D, Shao Z. Direct-methane solid oxide fuel cells with an in situ formed Ni–Fe alloy composite catalyst layer over Ni–YSZ anodes. Renewable Energy. 2020;150:334-41.

14. Fu CJ, Chan SH, Ge XM, Liu QL, Pasciak G. A promising Ni–Fe bimetallic anode for intermediate-temperature SOFC based on Gd-doped ceria electrolyte. International Journal of Hydrogen Energy. 2011;36(21):13727-34.

15. Chang H, Chen H, Yang G, Zhou W, Bai J, Li S, et al. Enhanced coking resistance of a Ni cermet anode by a chromates protective layer. Journal of Energy Chemistry. 2019;37:117-25.

16. Zhao Q, Geng S, Chen G, Wang F. Application of sputtered NiFe2 alloy coating for SOFC interconnect steel. Journal of Alloys and Compounds. 2018;769:120-9.

17. Zhao Q, Geng S, Chen G, Wang F. Influence of preoxidation on high temperature behavior of NiFe2 coated SOFC interconnect steel. International Journal of Hydrogen Energy. 2019;44(26):13744-56.

18. Zhao Q, Geng S, Gao X, Chen G, Wang F. Ni/NiFe2 dual-layer coating for SOFC steel interconnects application. Journal of Power Sources Advances. 2020;2.

19. Li K, Wang X, Jia L, Yan D, Pu J, Chi B, et al. High performance Ni–Fe alloy supported SOFCs fabricated by low cost tape casting-screen printing-cofiring process. International Journal of Hydrogen Energy. 2014;39(34):19747-52.

20. Tucker MC. Progress in metal-supported solid oxide fuel cells: A review. Journal of Power Sources. 2010;195(15):4570-82.

จุฬาลงกรณ์มหาวิทยาลัย
Chulalongkorn University

21. Lee C, Bae J. Fabrication and characterization of metal-supported solid oxide fuel cells. Journal of Power Sources. 2008;176(1):62-9.

22. Blennow P, Hjelm J, Klemensø T, Ramousse S, Kromp A, Leonide A, et al. Manufacturing and characterization of metal-supported solid oxide fuel cells. Journal of Power Sources. 2011;196(17):7117-25.

23. Simonsen SB, Muhl TT, Thydén KTS, Chatzichristodoulou C, Nielsen J, Sudireddy BR. Effect of Fe on high performing nanostructured Ni/Gd-doped ceria electrocatalysts. Solid State Ionics. 2019;340.

24. Nechache A, Cassir M, Ringuedé A. Solid oxide electrolysis cell analysis by means of electrochemical impedance spectroscopy: A review. Journal of Power Sources. 2014;258:164-81.

25. Hu X, Xie K. Active and stable Ni/Cr2O3-δ cathodes for high temperature CO2 electrolysis. Journal of Power Sources. 2019;430:20-4.

26. Jiang SP, Chen X. Chromium deposition and poisoning of cathodes of solid oxide fuel cells – A review. International Journal of Hydrogen Energy. 2014;39(1):505-31.

27. Horita T, Kishimoto H, Yamaji K, Xiong Y, Sakai N, Brito ME, et al. Effect of grain boundaries on the formation of oxide scale in Fe–Cr alloy for SOFCs. Solid State Ionics. 2008;179(27-32):1320-4.

28. Doenitz W, Schmidberger R, Steinheil E, Streicher R. Hydrogen production by high temperature electrolysis of water vapour. International Journal of Hydrogen Energy. 1980;5(1):55-63.

29. Eguchi K, Hatagishi T, Arai H. Power generation and steam electrolysis characteristics of an electrochemical cell with a zirconia- or ceria-based electrolyte. Solid State Ionics. 1996;86-88:1245-9.

30. Maskalick NJ. High temperature electrolysis cell performance characterization. International Journal of Hydrogen Energy. 1986;11(9):563-70.

31. Hauch A, Brodersen K, Chen M, Mogensen MB. Ni/YSZ electrodes structures optimized for increased electrolysis performance and durability. Solid State Ionics. 2016;293:27-36.

จุฬาลงกรณ์มหาวิทยาลัย
Chulalongkorn University

32. Hauch A, Mogensen M, Hagen A. Ni/YSZ electrode degradation studied by impedance spectroscopy — Effect of p(H2O). Solid State Ionics. 2011;192(1):547-51.

33. Holzer L, Iwanschitz B, Hocker T, Münch B, Prestat M, Wiedenmann D, et al. Microstructure degradation of cermet anodes for solid oxide fuel cells: Quantification of nickel grain growth in dry and in humid atmospheres. Journal of Power Sources. 2011;196(3):1279-94.

34. Jiao Z, Takagi N, Shikazono N, Kasagi N. Study on local morphological changes of nickel in solid oxide fuel cell anode using porous Ni pellet electrode. Journal of Power Sources. 2011;196(3):1019-29.

35. Laurencin J, Roche V, Jaboutian C, Kieffer I, Mougin J, Steil MC. Ni-8YSZ cermet re-oxidation of anode supported solid oxide fuel cell: From kinetics measurements to mechanical damage prediction. International Journal of Hydrogen Energy. 2012;37(17):12557-73.

36. Pandiyan A, Uthayakumar A, Subrayan R, Cha SW, Krishna Moorthy SB. Review of solid oxide electrolysis cells: a clean energy strategy for hydrogen generation. Nanomaterials and Energy. 2019;8(1):2-22.

37. Zhang J, Jang H, chen L, Jiang X, Kim MG, Wu Z, et al. In-situ formed N doped bamboo-like carbon nanotube decorated with Fe–Ni–Cr nanoparticles as efficient electrocatalysts for overall water-splitting. Materials Chemistry and Physics. 2020;241.

38. Wang X, Li K, Jia L, Zhang Q, Jiang SP, Chi B, et al. Porous Ni–Fe alloys as anode support for intermediate temperature solid oxide fuel cells: I. Fabrication, redox and thermal behaviors. Journal of Power Sources. 2015;277:474-9.

39. FethiHamdani Improvement of the corrosion and oxidation resistance of Ni-based alloys by optimizing

the chromium content. Materials. INSA de Lyon;Tohoku gakuin university (Sendai,Japon), 2015.

English. NNT:2015ISAL0012 .

40. Hwang, Jinn-Wen, "Thermal expansion of nickel and iron, and the influence of nitrogen on the lattice

จุฬาลงกรณ์มหาวิทยาลัย
Chulalongkorn University

parameter of iron at the Curie temperature" (1972). Masters Theses. 5049.

https://scholarsmine.mst.edu/masters_theses/5049.

41. Peter Hidnert, THERMAL EXPANSION OF HEAT-RESISTING ALLOYS: NICKEL-CHROMIUM, IRON-CHROMIUM, AND NICKELCHROMIUM-IRON ALLOYS.,J 7.1031(1931) Rp388.

42. Went JJ. Relation between the thermal expansion, the curie temperature and the lattice spacing of homogeneous ternary nickel-iron alloys. Physica. 1949;15(8):703-10.

43. Wang WQ, Su F, Xue YF, Cheng ZX, Gu QF, Campbell SJ, et al. Anomalous thermal expansion in ErFe11.4Nb0.6. Journal of Alloys and Compounds. 2020;823.

44. Yang J, Li Y, Macdonald DD. Effects of temperature and pH on the electrochemical behaviour of alloy 600 in simulated pressurized water reactor primary water. Journal of Nuclear Materials. 2020;528.

45. Egger P, Sorarù GD, Diré S. Sol-gel synthesis of polymer-YSZ hybrid materials for SOFC technology. Journal of the European Ceramic Society. 2004;24(6):1371-4.

46. Mingyi L, Bo Y, Jingming X, Jing C. Influence of pore formers on physical properties and microstructures of supporting cathodes of solid oxide electrolysis cells. International Journal of Hydrogen Energy. 2010;35(7):2670-4.

47. Kim Y-M, Kim-Lohsoontorn P, Baek S-W, Bae J. Electrochemical performance of unsintered Ba0.5Sr0.5Co0.8Fe0.2O3–δ, La0.6Sr0.4Co0.8Fe0.2O3–δ, and La0.8Sr0.2MnO3–δ cathodes for metal-supported solid oxide fuel cells. International Journal of Hydrogen Energy. 2011;36(4):3138-46.

48. Ni M, Leung M, Leung D. Parametric study of solid oxide steam electrolyzer for hydrogen production. International Journal of Hydrogen Energy. 2007;32(13):2305-13.

49. Hajabdollahi Z, Fu P-F. Multi-objective based configuration optimization of SOFC-GT cogeneration plant. Applied Thermal Engineering. 2017;112:549-59.

50. Chiodelli G, Malavasi L. Electrochemical open circuit voltage (OCV) characterization of SOFC materials. Ionics. 2013;19(8):1135-44.

จุฬาลงกรณ์มหาวิทยาลัย
CHULALONGKORN UNIVERSITY

51. Sainio J, Aronniemi M, Pakarinen O, Kauraala K, Airaksinen S, Krause O, et al. An XPS study of CrOx on a thin alumina film and in alumina supported catalysts. Applied Surface Science. 2005;252(4):1076-83.

52. Yamashita T, Hayes P. Analysis of XPS spectra of Fe2+ and Fe3+ ions in oxide materials. Applied Surface Science. 2008;254(8):2441-9.

53. Temperature Effects on Conductivity of Seawater and Physiologic Saline, Mechanism and Significance. Chemical Sciences Journal. 2016.

54. Qi W, Chen S, Wu Y, Xie K. A chromium oxide coated nickel/yttria stabilized zirconia electrode with a heterojunction interface for use in electrochemical methane reforming. RSC Advances. 2015;5(59):47599-608.

55. da Paz Fiuza R, Aurélio da Silva M, Boaventura JS. Development of Fe–Ni/YSZ–GDC electrocatalysts for application as SOFC anodes: XRD and TPR characterization and evaluation in the ethanol steam reforming reaction. International Journal of Hydrogen Energy. 2010;35(20):11216-28.

56. Pathak A, Singh AK. Mechanical properties of Ni-based solid solution alloys: A first principles study. Journal of Applied Research and Technology. 2017;15(5):449-53.

57. Teodorescu M, Banciu AC, Sitaru I, Segal E. Investigation concerning bimetallic catalysts using nonisothermal (temperature programmed reduction (TPR) and temperature programmed desorption (TPD)) and isothermal methods. Part 2. Nickel—chromium prereduced catalysts. Thermochimica Acta. 1994;240:199-205.

58. Kanervo JM, Krause AOI. Characterisation of Supported Chromium Oxide Catalysts by Kinetic Analysis of H2-TPR Data. Journal of Catalysis. 2002;207(1):57-65.

59. Ren Y, Bruce PG, Ma Z. Solid-solid conversion of ordered crystalline mesoporous metal oxides under reducing atmosphere. Journal of Materials Chemistry. 2011;21(25).

60. Al-Dossary M, Fierro JLG. Effect of high-temperature pre-reduction in Fischer–Tropsch synthesis on Fe/ZrO 2 catalysts. Applied Catalysis A: General. 2015;499:109-17.

61. Yao D, Wu C, Yang H, Zhang Y, Nahil MA, Chen Y, et al. Co-production of hydrogen and carbon nanotubes from catalytic pyrolysis of waste plastics on Ni-Fe bimetallic catalyst. Energy Conversion and Management. 2017;148:692-700.

62. Zhang Y, Liu B, Tu B, Dong Y, Cheng M. Redox cycling of Ni–YSZ anode investigated by TPR technique. Solid State Ionics. 2005;176(29-30):2193-9.

จุฬาลงกรณ์มหาวิทยาลัย
Chulalongkorn University

63. Lopes S, Pagnano V, Rollo JMDA, Leal M, Bezzon O. Correlation between metal-ceramic bond strength and coefficient of linear thermal expansion difference. Journal of applied oral science : revista FOB. 2009;17:122-8.

64. Hassan MA, Mamat OB, Mehdi M. Review: Influence of alloy addition and spinel coatings on Cr-based metallic interconnects of solid oxide fuel cells. International Journal of Hydrogen Energy. 2020.

65. Alnegren P, editor Oxidation behavior of selected FeCr alloys in environments relevant for solid oxide electrolysis applications2012.

66. Kan WH, Thangadurai V. Challenges and prospects of anodes for solid oxide fuel cells (SOFCs). Ionics. 2014;21(2):301-18.

67. Yan Y, Fang Q, Blum L, Lehnert W. Performance and degradation of an SOEC stack with different cell components. Electrochimica Acta. 2017;258:1254-61.

68. Bell T. Electrical Conductivity of Metals 2020 [cited 2020 13 August]. Available from: https://www.thoughtco.com/electrical-conductivity-in-metals-2340117.

จุฬาลงกรณ์มหาวิทยาลัย
Chulalongkorn University

APPENDICES

จุฬาลงกรณ์มหาวิทยาลัย
Chulalongkorn University

จุฬาลงกรณ์มหาวิทยาลัย
Chulalongkorn University

Appendix A

A.1 Material

Table A.1 Materials

No.	Material name	Company
1	Nickle oxide powder	Kceracell
2	Ni-Cr powder	Kceracell
3	Ni-Fe powder	Kceracell
4	LSM-YSZ ($La_{0.80}Sr_{0.20}Mn_{1.02}$ O_3-$(Y2O3)_{0.08}(ZrO_2)_{0.92}$)	Kceracell
5	BSCF ($Ba_{0.5}Sr_{0.5}Co_{0.8}Fe_{0.2}O_{3-\delta}$)	Kceracell
6	8% Yttria stabilized zirconia powder	Sigma-Aldrich
7	Polyvinyl butyral resin (Butvar98)	Chemcruz
8	Polyethylene glycol (PEG)	Sigma-Aldrich
9	Polyvinylpyrrolidone (PVPD)	Sigma-Aldrich
10	Alpha terpineol (Binder)	Sigma-Aldrich
11	Butyraldehyde	Sigma-Aldrich
12	Xylene	Sigma-Aldrich
13	Ethanol	Sigma-Aldrich

จุฬาลงกรณ์มหาวิทยาลัย
CHULALONGKORN UNIVERSITY

A.2 Porosity

The porosity of each hydrogen electrode was measured by ImageJ program. Porosity is decreased with the increasing of Cr content, as seen in Table A.2.

Table A.2 porosity (%) of various Ni-Cr-YSZ electrode

Composition	porosity (%)
55 Ni 5 Cr YSZ	32.37
50 Ni 10 Cr YSZ	8.47
45 Ni 15 Cr YSZ	2.27
40 Ni 20 Cr YSZ	6.95

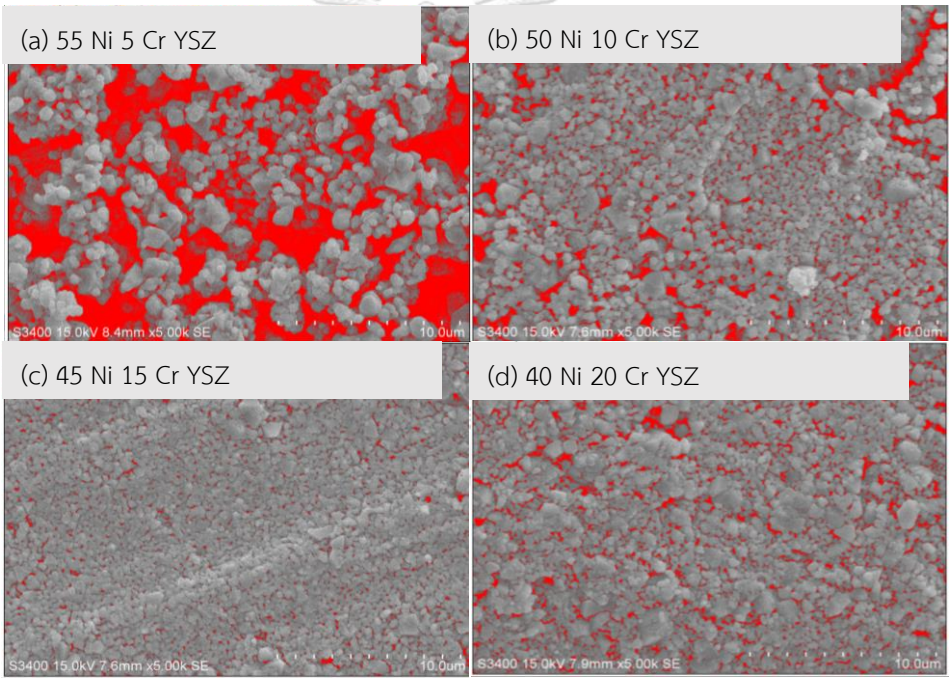

Fig. A.1 the analyzed SEM image of a) 55 Ni 5 Cr YSZ b) 50 Ni 10 Cr YSZ c) 45 Ni 15 Cr YSZ and d) 40 Ni 20 Cr YSZ electrode using the ImageJ program.

The porosity of conventional of Ni-YSZ, Alloy wash-coated Ni-YSZ and Alloys impregnated Ni-YSZ is shown in Fig. A.3.

Table A.3 porosity (%) of conventional Ni-YSZ, Alloys wash-coated Ni YSZ and Alloys impregnated Ni-YSZ

Composition	porosity (%)
Conventional Ni-YSZ	23.91
Alloys impregnated Ni YSZ	19.72
Alloys wash-coated Ni-YSZ	8.96

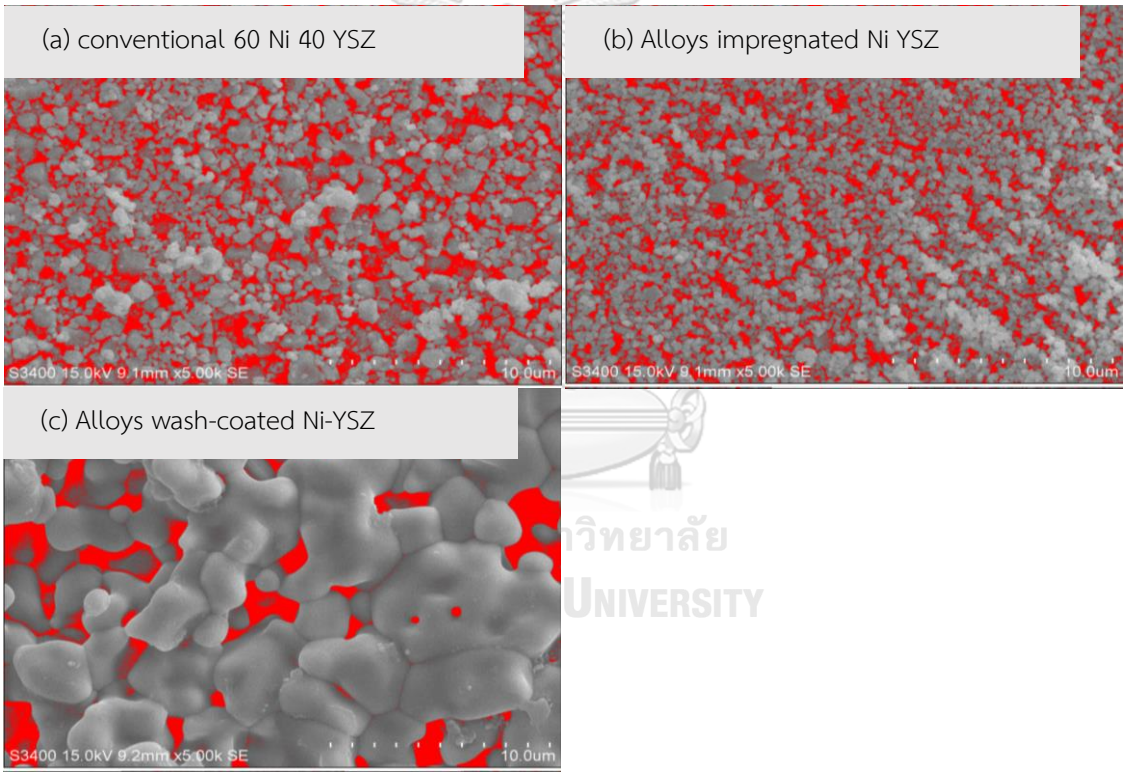

Fig. A.2 the analyzed SEM image of a) conventional Ni-YSZ b) Alloys impregnated Ni-YSZ c) and Alloys wash-coated Ni-YSZ electrode using the ImageJ program.

A.3 Scanning electron microscope and energy Dispersive X-ray Spectrometer (SEM-EDX)

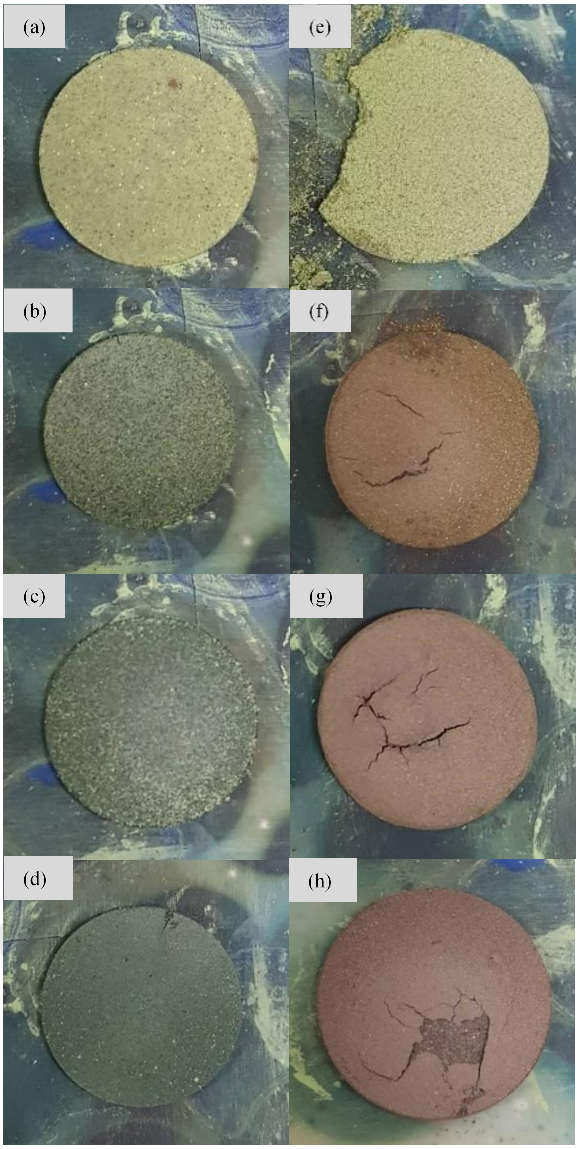

Fig. A.3 Sintered hydrogen electrode at 1,100°C for 2hr, using 5 °C/min. (a-d) hydrogen electrode containing 5 to 20 wt% Cr respectively and (e-h) hydrogen electrode containing 5 to 20 wt% Fe respectively.

Fig. A.3-A.10 show the EDX mapping of show hydrogen electrode containing of 5 to 20 wt% Fe respectively. For the NiCr-YSZ electrodes, the particle is packed and well-dispersed but for the NiFe-YSZ electrodes, the surface is already cracked and roughed.

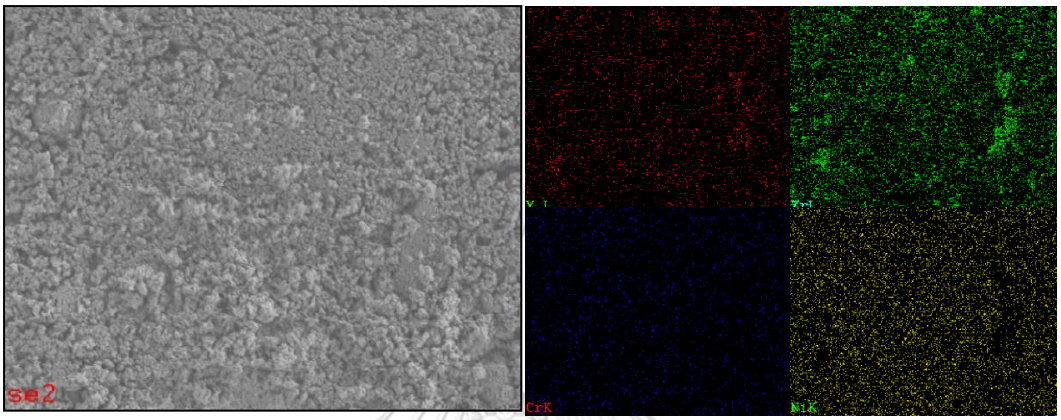

Fig. A.4 EDX mapping of sintered 55 Ni 5 Cr YSZ electrode at 1100 ℃ for 2 hr

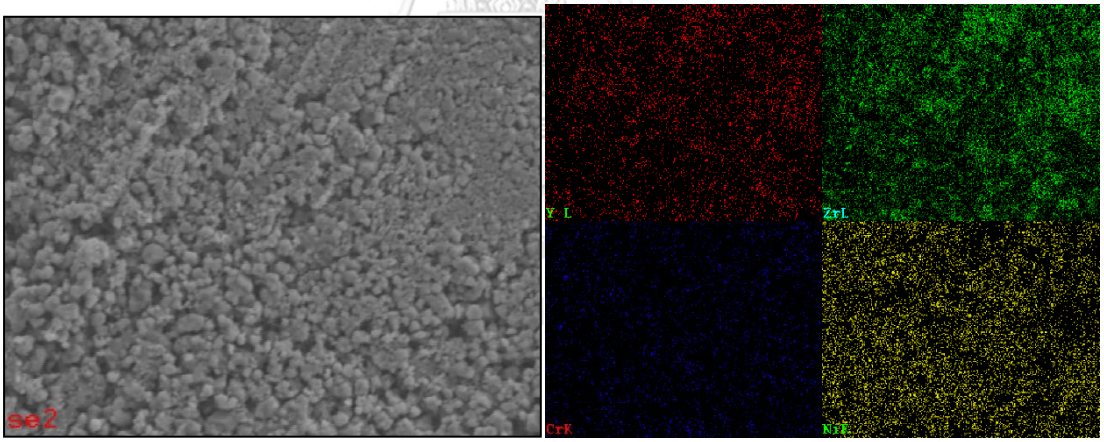

Fig. A.5 EDX mapping of sintered 50 Ni 10 Cr YSZ electrode at 1100 ℃ for 2 hr

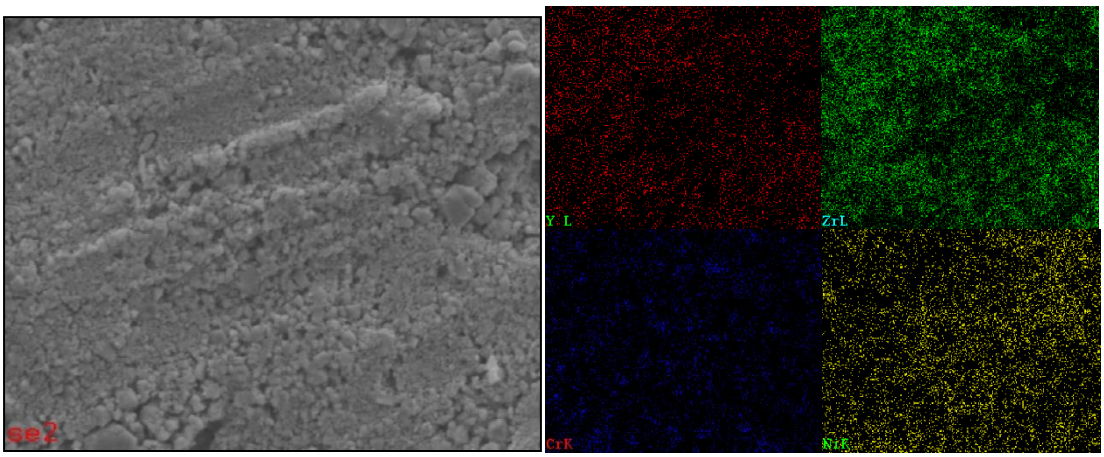

Fig. A.6 EDX mapping of sintered 45 Ni 15 Cr YSZ electrode at 1100 ℃ for 2 hr

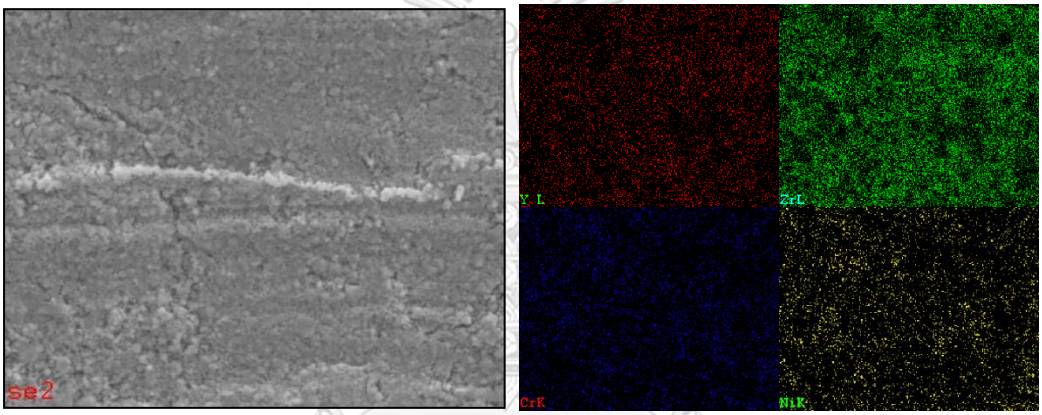

Fig. A.7 EDX mapping of sintered 40 Ni 20 Cr YSZ electrode at 1100 ℃ for 2 hr

จุฬาลงกรณ์มหาวิทยาลัย

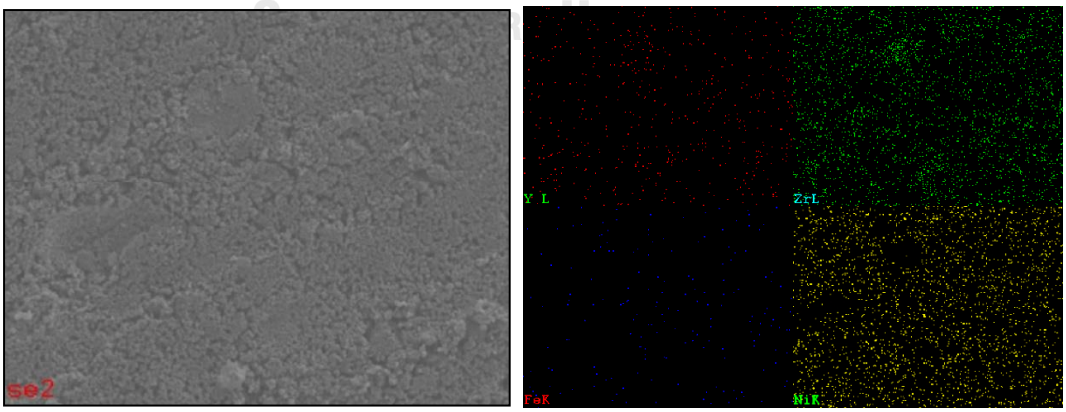

Fig. A.8 EDX mapping of sintered 55 Ni 5 Fe YSZ electrode at 1100 ℃ for 2 hr

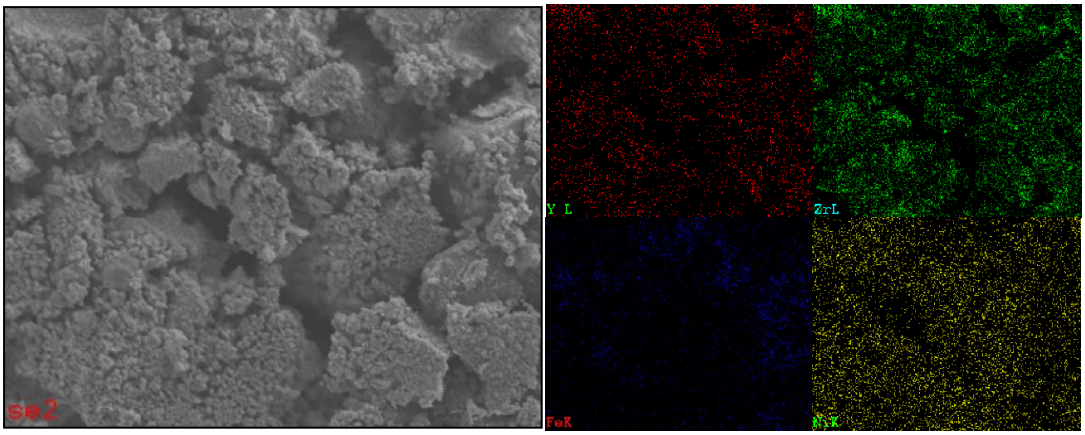

Fig. A.9 EDX mapping of sintered 50 Ni 10 Fe YSZ electrode at 1100 ℃ for 2 hr

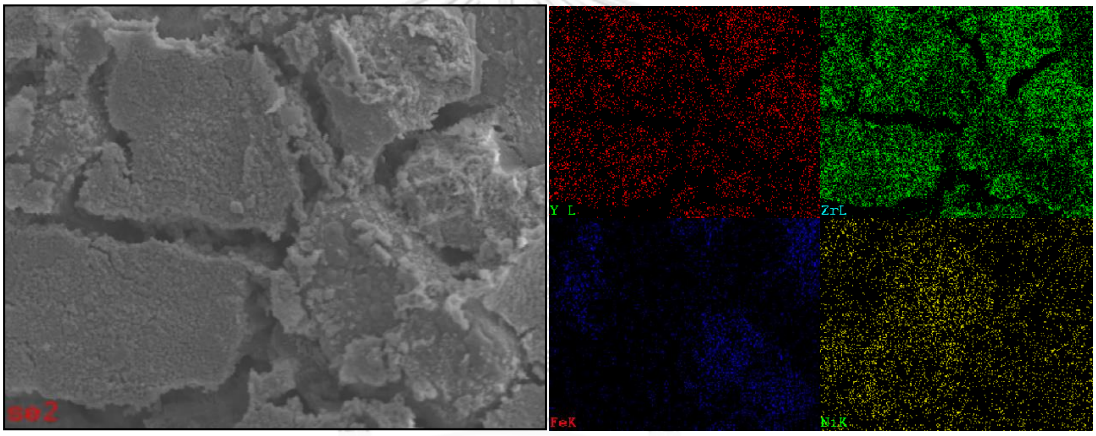

Fig. A.10 EDX mapping of sintered 45 Ni 15 Fe YSZ electrode at 1100 ℃ for 2 hr

Chulalongkorn University

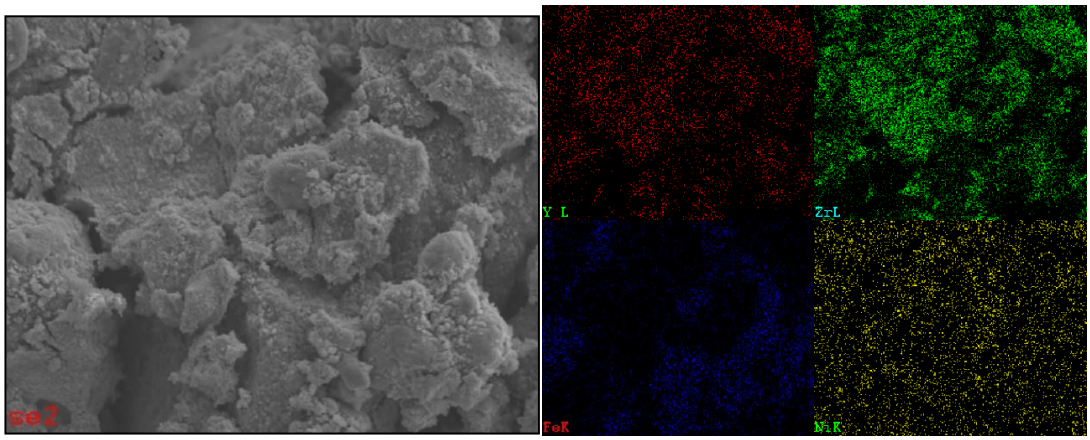

Fig. A.11 EDX mapping of sintered 40 Ni 20 Fe YSZ electrode at 1100 ℃ for 2 hr

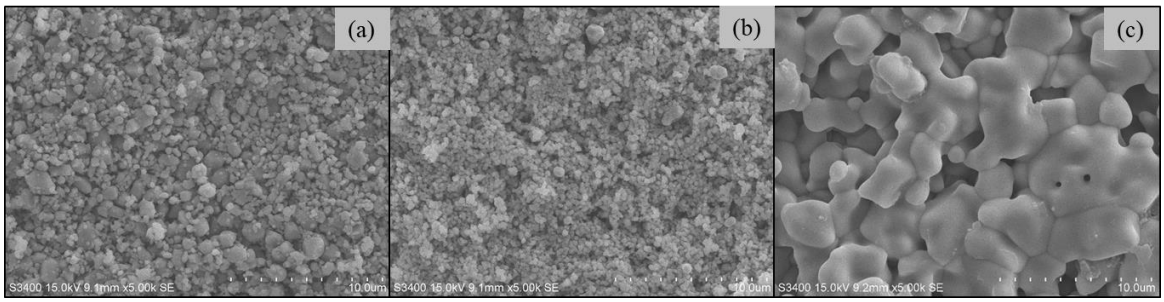

Fig. A.12 The SEM patterns at 5000X magnification of a) Ni-YSZ electrode, b) impregnated electrode and c) wash-coated electrode

After impregnated, the morphology structure and distribution of the cathode is studied by using SEM-EDX as shown in Fig. A.13. The cathode forms a structure with enough strength and well-dispersed.

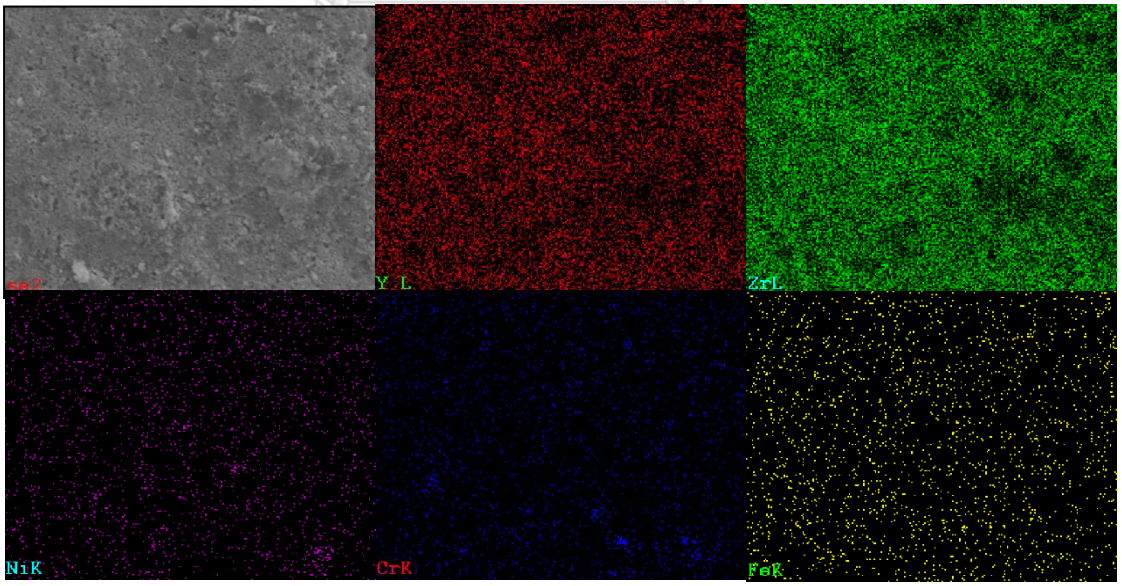

Fig. A.13 EDX mapping of sintered alloys wash-coated Ni-YSZ electrode at 1100 ℃ for 2 hr

The morphology structure and metal distribution of Impregnated hydrogen electrode is studied and shown in Fig. A.14. The fabrication method is significantly affecting the structure of electrode to form the dense sintered electrode.

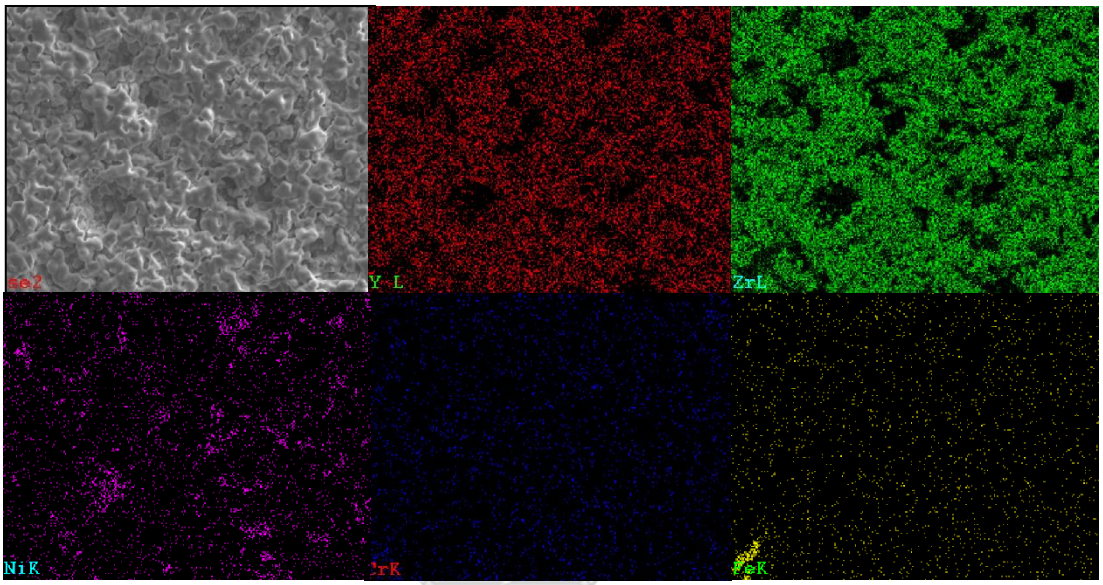

Fig. A.14 EDX mapping of sintered Impregnated hydrogen electrode at 1100 ℃ for 2 hr

จุฬาลงกรณ์มหาวิทยาลัย

The cross-section of the electrolyte supported cell was shown in Fig. A.15 The thickness of each cathode was shown in

Table A.4 Cathode thickness of the electrolyte supported cell

Composition	Cathode thickness, μm
Conventional Ni-YSZ	16.01
55Ni 5Cr-YSZ	26.52
50Ni 10Cr-YSZ	51.97
45Ni 15Cr-YSZ	29.70
40Ni 20Cr-YSZ	25.35

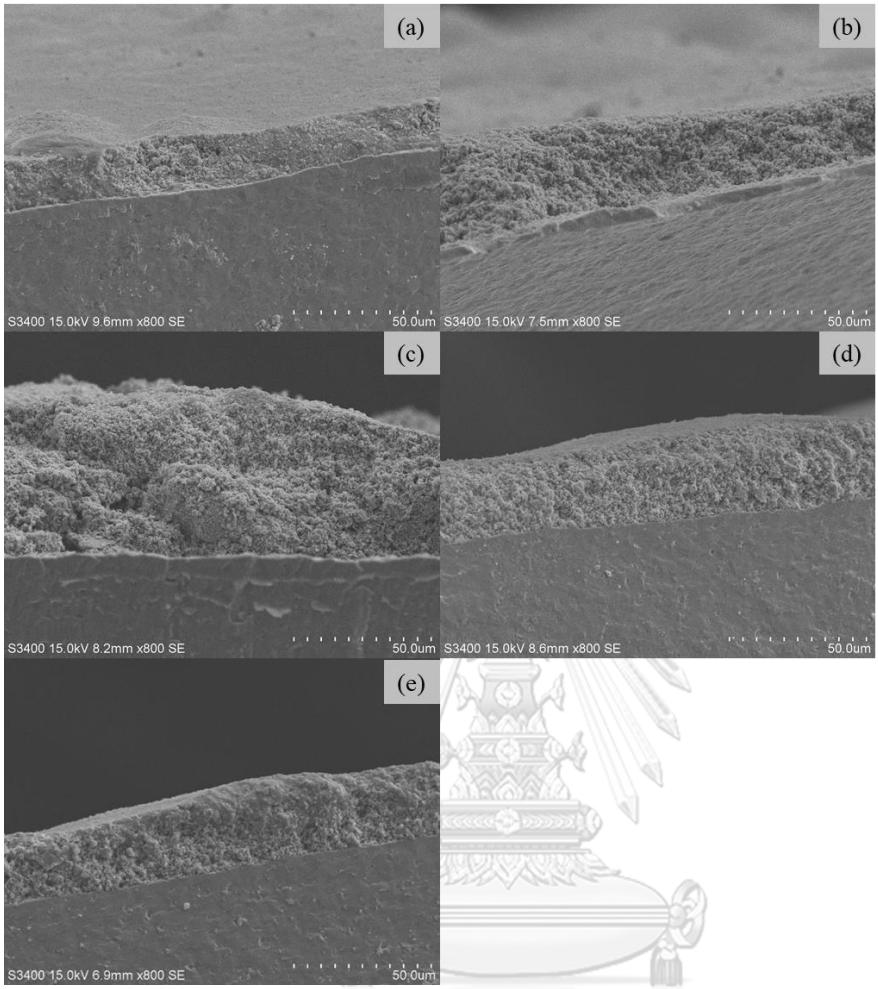

จุฬาลงกรณ์มหาวิทยาลัย
Chulalongkorn University

Fig. A.15 The SEM patterns at 800X magnification of cross sectional sintered (a) conventional Ni-YSZ (b) 55Ni 5Cr-YSZ (c) 50Ni 10Cr-YSZ (d) 45Ni 15Cr-YSZ and (e) 40Ni 20Cr-YSZ electrode using electrolyte as a support at 1100 ℃ for 2 hr

A.4 Calculation of hydrogen production rate

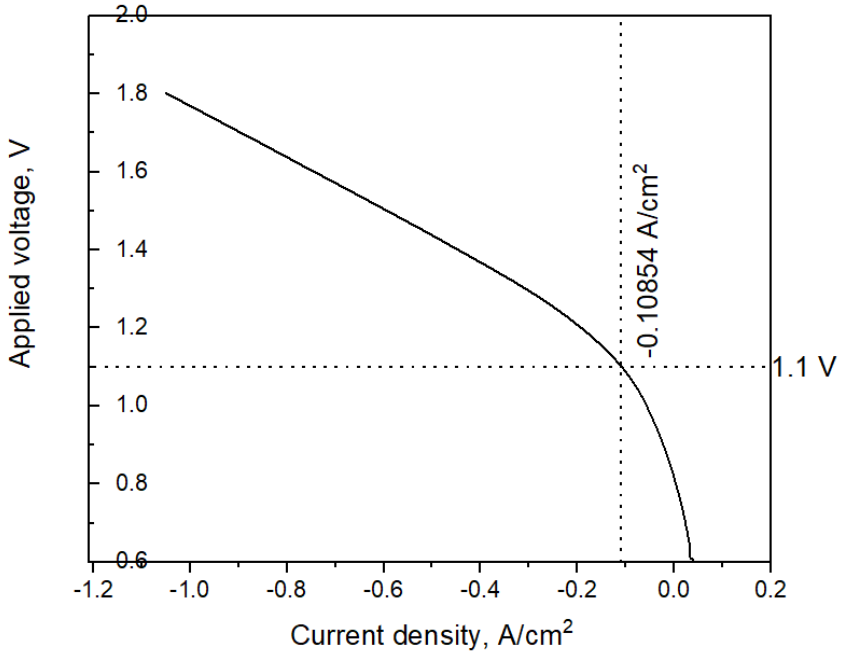

Fig. A.16 IV profile of electrolyte supported 55Ni 5Cr 40 YSZ/YSZ/Pt at 800 ℃ using steam to H_2 ratio at 70:30

จุฬาลงกรณ์มหาวิทยาลัย
CHULALONGKORN UNIVERSITY

$$m = \frac{I}{nF} \quad \cdots (A.1)$$

Where

m is an amount of mole is generated per area, I is a current (A or Coulomb/s), n is an amount of electron is generated in reaction (in this reaction n = 2), and F is the Faraday's constant (96,485 C/mol)

At 1.1 V, current density was 0.1085 A/cm^2. So, hydrogen production rate was

$$\frac{0.1085}{2 \times 96{,}485} = 5.62 \times 10^{-7} \text{mol s}^{-1}$$

A.5 Calculation of open circuit voltage (OCV)

$$E = E^0 - \frac{RT \ln\left(\frac{p_{H_2O}}{p_{H_2}\sqrt{p_{O_2}}}\right)}{nF} \qquad \cdots (A.2)$$

$$E^0 = -\frac{\Delta G^0}{nF} \qquad \cdots (A.3)$$

when E is the cell potential at the interested temperature, E^0 is the standard cell potential, R is the universal gas constant (8.314 $JK^{-1}mol^{-1}$), T is the temperature in kelvins, n is the number of electron transferred (in this reaction n = 2), F is Faraday constant (96,485 C mol^{-1}) and ΔG^0 is a standard Gibbs free energy.

จุฬาลงกรณ์มหาวิทยาลัย
Chulalongkorn University

At 900 °C using steam to hydrogen ratio of 70:30

For 150 ml/min total flow, 20 ml/min of H_2 and 46.67 ml/min of H_2O were fed and 83.33 ml/min of N_2 was used to balance the flow.

ΔG^0 for the $H_2 + ½\ O_2 \rightarrow H_2O$ reaction at 900 °C is -183.18 KJ/mol

Therefore, $E^0 = \frac{183{,}180}{2(96485)} =$ 0.9493 V

$$E = 0.9493 - \frac{8.314(1173.15)\ln\left(\frac{46.67/150}{(20/150)\sqrt{0.21}}\right)}{2(96{,}485)}$$
$$= 0.87\ \text{V}$$

A.6 Calculation of crystallite size by Sherer equation

$$\mathbf{B(2\theta)} = \frac{\mathbf{K\lambda}}{\mathbf{L{\cdot}Cos\theta}} \qquad \cdots (A.4)$$

Where L is crystallite dimension, B is the full width at half maximum intensity, θ is the Bragg angle, K is a Scherrer constant (0.94) and λ =X ray wavelength (1.54)

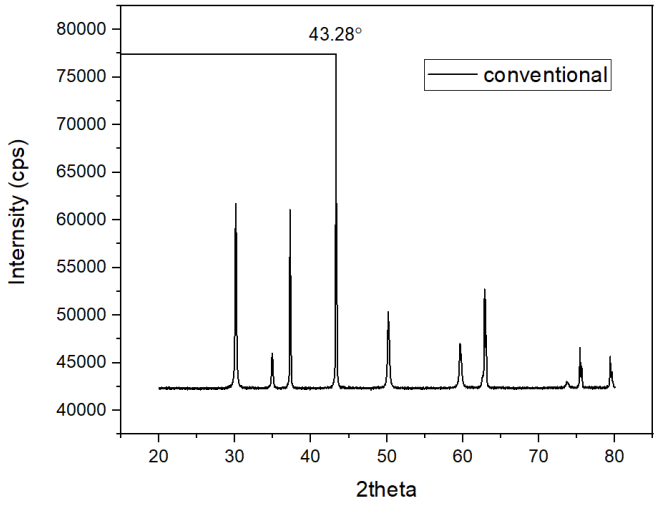

Fig. A.17 XRD pattern of conventional Ni-YSZ

The half intensity is 38,750 cps. FWHM is 0.2066.

$$B = \frac{FWHM \times 2\pi}{360} \quad \cdots (A.5)$$

$$B = \frac{0.2066 \times 2\pi}{360} = 0.0036$$

From eq (A.4) $L = \frac{K\lambda}{B(2\theta)\cdot Cos\theta} = \frac{0.94(1.54)}{0.0036\cdot Cos(21.54)}$

$=$ 433.9 A = 43.39 nm

จุฬาลงกรณ์มหาวิทยาลัย
Chulalongkorn University

VITA

NAME	Aritat Wongmaek
DATE OF BIRTH	20/02/1996
PLACE OF BIRTH	Bangkok, Thailand
INSTITUTIONS ATTENDED	Faculty of Engineering, Chulalongkorn University Faculty of Engineering, Mahidol University
HOME ADDRESS	20/7 m.4 Bangkratuk, Nakornpathom, Thailand, 73210

จุฬาลงกรณ์มหาวิทยาลัย
CHULALONGKORN UNIVERSITY